THE INTERSTELLAR MEDIUM OF DWARF GALAXIES

A Thesis

Submitted to the

Tata Institute of Fundamental Research
(A Deemed University)

for the degree of Doctor of Philosophy
in Physics

by

Narendra Nath Patra

National Centre for Radio Astrophysics
Tata Institute of Fundamental Research
2015

"আমার এ ক্ষুদ্র অঞ্জলি থাক তোমার চরনতলে"

--- বাবা ও মাকে

"Let my little tribute rest at your feet"

--- To my Dad and Mom

Acknowledgements

It has been a long bumpy journey so far and I have enjoyed it thoroughly in both sense. Now its time to reconcile the past and rejuvenate a few old memories. I joined NCRA approximately six and half years ago when I had no idea about astrophysics. Now look at me, submitting a thesis; interesting! Isn't it? But a great effort of many people have gone in producing this thesis and here I would like to take the opportunity to pay my sincere thanks to them.

Jayaram has been an ideal guide. His cool and calm smiling face always inspires one to take everything easy. He has been very patient with me and I am sure many time I almost got on his nerve. I still fondly remember those conversation when he use to debug me like a kid and advice me 'look naren, you have to work'. And the best part of him is, one doesn't have to lie to him, 'Jayaram I did not work for last couple of days', his reply would be 'Its okay, work now'. Every body doesn't have luxary to this kind of support. He has been a great adviser and without his constant support and inspiration I would not have come this far. I won't thank him, I would like to pay my respect and sincere gratitude to him.

I would like to thank Nissim for his constant effort to keep me in track in all possible ways. He has been a good friend and a critic, a hard one though! Nissim's scientific inputs to my research work continue to be very helpful. I would like to thank Yogesh Wadekar and Tirthankar Roychowdhury for their support and advise during my reviews which helped me a lot to improve myself. I would like to thank Dipanjan Mitra for his valuable suggestions (mainly during breakfast together) which helped me to see life with a different perspective. I would like to thank Rajaram, Saikia, Divya, Dharam, Ishwar, Subhasis, Govind, Poonam and others who made my stay

at NCRA much nicer both academically and socially. B. C. Joshi has been very friendly who helped me a lot time to time. I would like to thank Gulab, Ajit, Anand, Kandu, Dadhich, Ranjib, Maulik, Dhurandar and others from whom I learned a lot during graduate school course work.

I would specially like to thank Hemant and Reena for their constant cooperation in all academic (and non-academic) puposes. They have been very helpful specially locating Jayaram in the times of need! I would like to thank all NCRA staff members who made my stay at the campus a homely and comfortable one. I would like to thank J. K. Solanki for his help in various issues irrespective of the day, time, situation. He has been a good friend (a really inspiring one) and a well wisher too. I would like to thank all canteen staff. It is their constant effort from morning 7 am to 9:30 pm which made me feel home. I would like to thank all the security guards for being so nice and helpful every time. I would like to specially thank to Desaiji, Sureshji, Ganesh and Pramod for their kind efforts to keep the campus and our residence clean.

I would like to thank my friend and former office mate Rahul Basu. We have spent a long time in the same office. We together had a lots of memory to cherish during my stay at NCRA. He has been a very good friend. I would like to thank Dipanjan Mukherjee, Charlse, Sibu-da, Aditya, Sanved, Jincy, Merykutti, Mariyam and Azad C.S. with whom I had a lots of fun during graduate school. I would like to thank Vishal Gajjar and Arun Kumar Naidu for their humorous talks which made my life so much better. I would like to thank Ujjwal Kumar, Aritra Basu and Yogesh Chandola with whom I spent a significant amount of good time at NCRA. It has been great fun in cooking and hanging around hostel pantry with Alka, Raghu, Naidu, Doda and many others. I would like to thank Sweta also for being around and breaking the silence with a loud laugh. I would like to thank all hostelers, specially Kanaiya and Yogesh for making my hostel life in general eventful. I would like to thank my good friend Doda (Jyotirmay) for his constant push to finish my thesis. I would also like to thank Prakash, Aditya, Rohit for spending light times filled with enjoyment where we discussed nonsense

movies like ‘The Angrez’ and kept on laughing. I would like to thank Abhishek Johri for taking care of several hostel affairs. I would like to thank my good friend Anirban, Mayukh and Sayan for being there in needy times. I would like to thank my friend Vikas whose life continues to inspire me.

I would like to thank Gunjan (a very special friend in my life) for her constant support during last three years. She has been a valuable company who helped me a lot to take out the best of me. She is the one who taught and inspired me to work even harder. She has been there in tough and easy times and I am really thankful for her dedication/commitment towards my betterment.

I would like to thank Prasun Dutta from whom I learned a lot. It was great to discuss science during cooking with him. I thank Kanan Dutta who has been a precious friend and guide. I fondly remember the times when we use to go for evening walk and discuss various issues. I thank Arunima Banerjee for being a good adviser and collaborator. In many occasions her calm, simple advises worked best for me. I pay my sincere gratitude to her. I would like to thank Nirupam Roy (Gurudev) whose guidance not only helped me, but constantly inspired me in moving forward. I would like to thank Sambit Roychowdhury for his immense help in resolving various issues with AIPS, IRAF, FUV data and so many other things. Mariyam has been a very close friend, philosopher and guide to me. She contributed a lot in a positive way in the times when I needed. Though I keep saying to her ‘No thanks and no sorry between friends’, yet let me take the opportunity to break it and say thanks to Mariyam for everything.

I would like to thank my dear sir Mr. Subrata Kumar Burai whose never ending inspiration and love kept me alive in difficult times. He has been somebody who always believed in me and kept on motivating. I pay my respect to him and ask for his forgiveness for all odds.

I would like to thank my brothers Gupinath who has been a great teacher to me. His life still is an example of values and morals to me.

I would like to thank my 'Tandav bahini' and 'Bhairabh bahini' at Sitapur. They continue to give me strength and motivation to move forward. They have been a great source of my enthusiasm and are inseparable part of my life. I would like to thank my sister Mamani for her constant support in all odds like a solid friend. I would like to thank Dipak for taking care of my family during the last few years. I would like to pay my respect and love to my uncle late Jaydev Kar.

My father Shri Nimai Chandra Patra is the hero of my life. Behind every little success of mine, he is the architech. Whoever I am today, its because of his tremendous dedication and sacrifice. Once swami Vevekananda said in the praise of Shri Ramakrishna – 'He (Shri Ramakrishna) can create a thousand Naren (Swami Vivekananda) with a handful of dust'. I would like to give the same tribute to my father. Howmuch I say for him will fall short. My mother Smt. Rita Rani Patra has been a good teacher to me. She taught two important lessons of life, patience and simplicity. She has always blessed me with her unconditional love and care. I won't thank my mom and dad, let my thesis be a small tribute to them.

This thesis uses data from earlier GMRT observations which has been observed and analysed by Ayesha Begum. I really thank Ayesha for her effort (painful) in compiling such a large comprehensive data set. I would like to thank GMRT staff and the operators for their assistence during my observations. This thesis used data from NASA's Astrophysics Data System and I am thankful to NASA for maintaining such useful facilities. I would also like to thank NCRA-TIFR research fellowship for supporting my research.

Narendra Nath Patra
July 2015, Pune

Declaration

This is a presentation of my original research work. Wherever contribution of others are involved, every effort is made to indicate this clearly, with due reference to the literature, and acknowledgement of collaborative research and discussions.

The work was done under the guidance of Prof. Jayaram N. Chengalur, at the National Centre for Radio Astrophysics (Pune) of the Tata Institute of Fundamental Research, Mumbai.

(Narendra Nath Patra)

In my capacity as supervisor of the candidate's thesis, I certify that the above statements are true to the best of my knowledge.

(Prof. Jayaram N. Chengalur)

Date: 10^{th} July, 2015

Abstract

In hierarchical structure formation models of galaxy formation, the smallest objects form first and then collapse together to form larger objects. In this sense the local volume dwarf galaxies are analogues to the primordial galaxies in the early universe which makes them interesting to study. In addition, local volume dwarf galaxies have very low metallicity as well as low dust-content which provides a unique laboratory for the study of the interplay between gas and star-formation in extreme environments. The dark matter content and its influence on determining the structure and dynamics of these galaxies also could provide vital insight regarding the formation and evolution of these galaxies. In this thesis we use existing data from FIGGS (Faint Irregular Galaxies GMRT Survey) (Begum et al., 2008) survey along with fresh GMRT observation of 21 dwarf galaxies (FIGGS2 (see chapter 3 for details)) to study local volume dwarf galaxies.

FIGGS2 is an extension of our earlier survey Faint Irregular Galaxies GMRT survey (FIGGS) towards the faint luminosity end. A sample of 21 faint galaxies were observed in HI with the Giant Meter-wave Radio telescope to enrich the comprehensive data of FIGGS survey. For these galaxies, complementary multi-wavelength data already exist. The median blue band magnitude of the FIGGS2 sample is -11.7, which is more than one magnitude fainter than earlier FIGGS sample. The median HI mass of FIGGS2 sample is $\sim 10^{5.6}$ $M_{\odot}$which is also about an order of magnitude lower than the FIGGS sample. The observations and the first results of FIGGS2 survey constitute a part of this thesis. We detected 15 galaxies out of 21 observed in HI with the GMRT. The HI diameter and the HI mass of these galaxies shows a tight correlation with a slope of 2.32 ± 0.31 which agrees within the errorbars with the value of 1.99 ± 0.11 with FIGGS galaxies (Begum

et al., 2008). FIGGS2 samples are amongst the faintest galaxies and have a very shallow gravitational potential well. The interstellar gas are hence highly susceptible to feedback from star-formation. We show in this thesis that there is enough indication that the HI of our sample galaxies are highly offset from the optical disc in many cases indicating a possible feedback mechanism in action. FIGGS and FIGGS2 together form the largest sample of gas rich faint dwarf irregular galaxies till date.

Neutral atomic gas at high redshift can only be studied via the absorption lines that are produced when a gas cloud happens to lie in front of a more distant quasar. Much of what we know about the HI content of the early universe comes from the study of these absorption line systems. The absorption systems with the highest column densities ($N_{HI} \gtrsim 10^{20.3}$ atoms cm^{-2}), the so called Damped Lyman-α Absorbers (DLAs) are known to contain the bulk of the neutral gas at high redshift. DLAs are of particular interest because at these column densities self shielding results in the ionised fraction of the gas being small (Wolfe et al., 2005). As such, DLAs represent the most likely sites of star formation at high redshifts. However, despite decades of study, the nature of DLAs remains unclear; in particular the size and morphology of the systems remained until recently relatively poorly constrained by observations. Two extremes of the models that have been proposed are (i) that DLAs arise from large rotating disks, much like the disks of modern day spirals (e.g. Prochaska and Wolfe, 1997; Wolfe et al., 1986) at the one end and (ii) that DLAs arise from small systems analogous to the current day dwarf galaxies at the other (e.g. Haehnelt et al., 1998). Recent numerical simulations suggest a more nuanced picture where a wide range of hosts gives rise to the observed DLAs (see e.g. Cen, 2012; Pontzen et al., 2008). Another direct observable from the absorption studies is the column density distribution function $f(N_{HI})$, which gives the expected number of absorbers with HI column density between N_{HI} and $N_{HI}+dN_{HI}$ per unit distance. For the local galaxy population also $f(N_{HI})$ can be computed; this makes it one of the few statistics which can be computed for both the high redshift as well as local populations. Interestingly this $f(N_{HI})$ for DLAs matches that observed in local spirals (Zwaan et al., 2005).

In chapter 3 we study the HI column density distribution function, $f(\mathrm{N_{HI}})$, as measured from dwarf galaxies observed as part of our FIGGS survey. We find that the shape of $f(\mathrm{N_{HI}})$ for dwarfs is significantly different from $f(\mathrm{N_{HI}})$ for high redshift Damped Lymanα absorbers (DLAs) or for a representative sample of $z = 0$ gas rich galaxies. The dwarf $f(\mathrm{N_{HI}})$ falls much more steeply at high HI column densities as compared to the other determinations. While $\sim 10\%$ of the cross section above $\mathrm{N_{HI}} = 10^{20.3}$ atoms cm^{-2} at $z = 0$ is provided by dwarf galaxies, the fraction falls to $\lesssim 1\%$ by $\mathrm{N_{HI}} \sim 10^{21.5}$ atoms cm^{-2}. In the local universe, the contribution to the high $\mathrm{N_{HI}}$ end of the $f(\mathrm{N_{HI}})$ distribution comes predominantly from the inclined disks of large galaxies. Dwarf galaxies, both because of their smaller scale lengths, and their larger intrinsic axial ratios do not produce large HI column densities even when viewed edge-on. We conclude that if high column density DLAs/GRB hosts correspond to galaxies like the local dwarfs, this would require either that (i) the absorption arises from merging and not isolated systems or (ii) the observed lines of sight are strongly biased towards high column density regions.

The vertical gas distribution in a galaxy is determined by the balance between the vertical pressure gradients and the net gravitational potential of the galaxy in vertical direction. Measurements of the HI scale-heights of nearby edge-on galaxies hence allow one to infer the vertical gravitational field. Further, since the HI disc generally extends to a galacto-centric radii where the gravity due to stars is negligible, both the flaring of the HI disc as well as its rotational velocity can be used as diagnostic probes of the underlying potential of the dark matter halo (see e.g. Banerjee and Jog, 2008; Banerjee et al., 2010, 2011a; Becquaert and Combes, 1997; Narayan et al., 2005; Olling, 1995).

We model the observed vertical distribution of the neutral hydrogen (HI) in the faint ($\mathrm{M_B} \sim -13.7$ mag) edge-on dwarf irregular galaxy KK250 in chapter 4. Our model assumes that the galaxy consists of axi-symmetric, co-planar gas and stellar discs in the external force-field of a spherical dark matter halo, and in vertical hydrostatic equilibrium. The velocity dispersion

of the gas is left as a free parameter in the model. Our best fit model is able to reproduce the observed vertical distribution of the HI gas, as well as the observed velocity profiles. The best fit model has a large velocity dispersion (~ 22 km s^{-1}) at the centre of the galaxy, which falls to a value of ~ 8 km s^{-1} by a galacto-centric radius of 1 kpc, which is similar to both the scale-length of the stellar disc, as well as the angular resolution of the data along the radial direction. Similarly we find that the thickness of the HI disc is also minimum at $\sim$ 1kpc, and increases by about a factor of ~ 2 as one goes to the centre of the galaxy or out to $\sim$ 3kpc. The minimum intrinsic HWHM of the HI vertical distribution in KK250 is $\sim$ 350pc. For comparison the HWHM of the vertical distribution of the HI in the solar neighbourhood is $\sim 70-140$ pc. Our results are hence consistent with other observations which indicate that dwarf galaxies have significantly puffier gas discs than spirals.

In chapter 5 we study the amount of 'cold' HI in dwarf galaxies and its relation to star formation. We used two different methods to detect cold HI in a sample of dwarf irregular galaxies selected from the FIGGS survey. In the first method, line-of-sight HI spectra were decomposed into multiple Gaussian components and narrow width components were identified with $\sigma \lesssim 6$ km s^{-1}(T$_{\rm K}$ $\lesssim$ 4000 K) as cold HI . In multi-phase models of ISM (Wolfire et al., 1995a), the presence of high brightness temperature gas is generally indicative of the presense of a cold dense phase along the line of sight. This is because in these models the warm gas generally has too low an optical depth to contribute more than a few degrees K to the brightness temperature. For example, a typical WNM produces $\sim$ 9 K brightness temperature for a path length of 2 kpc. An alternative method for searching for the CNM would then be to look for gas with brightness temperature more than say $\sim 10K$. Indeed this method has previously been used to identify cold, optically thick gas in external galaxies by Braun (1997, 2012); Braun and Walterbos (1992). Adopting a conservative approach like Braun (1997) a brightness temperature limit of 50K were set as a threshold to identify cold HI in high resolution ($\sim$100 pc) HI map. Cold HI is detected in $\sim$ 50% galaxies using Gaussian decomposition method and in $\sim$ 65%

galaxies using T_B method. We compare the two methods, and conclude that the T_B method is better suited to our sample galaxies.

In chapter 6 we study the Kennicutt-Schmidt law of cold HI in a sample of star-forming dwarf galaxies selected from FIGGS survey at a very high spatial resolution of ~ 100 pc. We use publicly available *GALEX* FUV data and processed it to derive FUV star-formation map of our sample galaxies. At this high resolution, we detect predominantly cold high column density gas and a better correlation with star formation is expected. But instead we find an opposite trend showing an inefficient star formation at our resolution as compared to ~ 400 pc resolution (e.g. Roychowdhury et al., 2009, 2011). The best fit power law to our data gives a slope of 0.52 ± 0.04 which is very flat as comapred to previous studies. We take this as indicating that the total HI is a better tracer of the molecular gas and hence the SFR than the dense cold HI clumps.

Contents

List of Figures

LIST OF FIGURES

List of Tables

1

Introduction

1.1 Introduction

Though there is no widely accepted definition of dwarf galaxies, most definitions are based on the optical brightness. Typically a galaxy is called dwarf if its absolute blue band magnitude (M_B) is greater than -17. However, there are many exceptions to this definition. For example (Hodge, 1971) set $M_B > -15$ as a criteria for dwarf galaxies whereas (Tammann, 1994) used $M_B > -16$ and more extended than globular clusters to classify dwarf galaxies. Broadly though galaxies significantly smaller than the Milky Way are regarded as dwarfs.

Based on their gas content and ongoing star-formation rate, dwarf galaxies can be broadly classified into three different types viz. dwarf Irregular (dIrr) galaxies, blue compact dwarf (BCD) galaxies and dwarf Spheroidal (dSph) galaxies. Dwarf Spheroidal galaxies have negligible amount of gas and very little or no measurable on-going star-formation. These galaxies consist largely of an old stellar population. Dwarf Irregulars are gas rich galaxies with some on-going star-formation. BCDs have significant amount of gas and very high on-going star-formation or even an ongoing star burst.

Dwarf galaxies are the most abundant galaxy type in the local universe. In hierarchical structure formation models of galaxy formation, the smallest objects form first and then merge together to form larger objects. Hence one would expect that dwarf like galaxies should dominate the population in the early universe. Also, the chemical evolution of the nearby dwarf galaxies appears to be slow compared to normal spiral galaxies. Dwarf galaxies have significantly lower metallicities than spirals. For these

reasons the local volume dwarf galaxies could be regarded analogues to the galaxies at early universe and the study of these galaxies could help understand galaxy formation and evolution. In this thesis we use data from the Faint Irregular Galaxies GMRT Survey (FIGGS) (Begum et al., 2008) and the FIGGS2 survey (see chapter 2) survey to address several scientific questions which we discuss below in brief.

1.2 Dwarf galaxies in a cosmological context

The ΛCDM model is the most successful cosmological model till date (Abazajian et al., 2009; Kravtsov, 2006). ΛCDM numerical simulations successfully reproduce different observable properties of galaxies in the local universe (eg; the luminosity function, the two-point correlation function etc.) (Genel et al., 2014). Despite its major successes, there are still some 'crisis' areas in which the ΛCDM model fails to reproduce observations.

One of these is the so called 'core-cusp' problem. From observations, (e.g. Kormendy and Freeman, 2004) constant density dark matter cores (such as those of an isothermal halo) are found to better fit galaxy rotation curves than the 'cuspy' dark matter cores predicted by numerical models (Navarro et al., 1997). With earlier low resolution observations, the distinction between 'core' and 'cusp' like halos was difficult to make, but more recent high resolution HI and Hα observations (Begum and Chengalur, 2004; Begum et al., 2003; de Blok et al., 2008; Gentile et al., 2004) have clearly favour a 'cored' halo.

Gas rich dwarf galaxies can be used as potential samples to resolve the 'core-cusp' problem. In normal large spiral galaxies, the central stellar bulge and the stellar disk contribute most to the rotation curve. Determining the densities of the dark matter is difficult because of ambiguities arising from the Mass-to-Light (M/L) ratio across galaxy samples or even within a galaxy. Whereas gas rich dwarf galaxies like the FIGGS or FIGGS2 galaxies have relatively smaller stellar masses and the mass decomposition is less affected by the stellar M/L ratio.

ΛCDM simulations shows that a 'cuspy' halo can not be created by collapsing 'cores' (Dehnen, 2005). Hence some other mechanism is needed to explain the 'core-cusp problem under ΛCDM scenario. One promising idea is to invoke star formation feedback. Feedback could result in the expulsion of a large amount of baryons from the

central region of a galaxy. This in turn could lead to the dark matter in the centre being smoothed out to create a relatively flat dark matter profile (Governato et al., 2012, and references therein). However, details of star formation feedback processes are not well quantified in the faintest dwarfs. Hence studies of star formation and feedback in these galaxies are very important.

Another leading problem of ΛCDM is the 'missing satellite problem'. This refers to the discrepancy between the predicted and the observed number of sub-halos at the lower end of the circular velocity or halo mass function (Klypin et al., 1999; Moore et al., 1999). In spite of many discoveries of extremely faint galaxies through deep observations (Belokurov et al., 2007; Tollerud et al., 2008), the discrepancy has not yet been fully resolved. Specially the latest high resolution simulations of Milky Way type halos predicted more sub luminous sub-halos around Milky Way type halos (Diemand et al., 2008; Springel et al., 2008; Stadel et al., 2009) than expected before. Within the framework of ΛCDM, several solutions have been proposed to counter this problem. For example, it has been proposed that the galaxy formation before and after the reionization of the universe were different and galaxy formation were suppressed completely or partially in halos with circular velocities/masses bellow some threshold value. Alternatively, it is also proposed that the fraction of sub-halos forming galaxies decreases with halo circular velocity or halo mass with most of the low mass halos remaining dark and observationally undetectable (Busha et al., 2010; Koposov et al., 2009; Li et al., 2009). The other mechanisms of making dark halos could be through reheating and reionization of the collapsed baryons into dark matter halos (e.g. Busha et al., 2010; Koposov et al., 2009). Koposov et al. (2010) proposed if the luminous galaxies were formed in most massive halos prior to accretion, the observation could be explained in a better way under ΛCDM scenario. In spite of these theoretical considerations, this is still an open problem and lot more deep observations as well as high resolution realistic numerical simulations are required to better understand the 'missing satellite problem'.

Neutral atomic gas at high redshifts can only be studied through absorption lines against distant background quasars or gamma-ray burst (GRB) afterglows. The highest column density ($N_{HI} > 2 \times 10^{20}$ atoms cm^{-2}) absorbers (the so called Damped Lyman-alpha Absorbing Systems (DLAS)) are particularly interesting because they contain the bulk of the atomic gas and are the best known gas reservoir for future star

formation (Noterdaeme et al., 2009, 2012b; Péroux et al., 2005; Prochaska and Wolfe, 2009; Prochaska et al., 2005; Zafar et al., 2013; Zwaan et al., 2005).

Systematic surveys (e.g Noterdaeme et al., 2009; Prochaska and Wolfe, 2009; Wolfe et al., 1986) have discovered a large number of these absorption systems. However, despite of long effort over the last decade the nature of DLAS hosts remains poorly understood. The properties of the host are very difficult to trace as the information is constrained only within the pencil beam along the line-of-sight. Two extremes of the models that have been proposed for the host systems are i) DLAs arise from large rotating disks like present day spiral galaxies (e.g Prochaska and Wolfe, 1997, 1998; Srianand et al., 2005; Wolfe et al., 1986, 2003), ii) DLAs arise from small systems much like small dwarf galaxies in the local universe (e.g. Haehnelt et al., 1998; Ledoux et al., 1998). There are other models too; (For e.g. Schaye, 2001) proposed that large scale outflows can provide large cross-section for hosting DLAS and can also explain the high incident rates of the same.

Direct imaging of DLA hosts would be of prime interest to resolve these uncertainities in understanding DLAS. But this is a very difficult task, mainly due to the low brightness of the associated galaxy/galaxies (in contrast to the bright background emission from the QSO) and their unknown location with respect to the line-of-sight (Kanekar et al., 2001). There has been significant effort in recent years to identify the host galaxies using clever selection strategies as well as efficient instrumentation on large telescopes (Bouché et al., 2012; Fynbo et al., 2010, 2011; Noterdaeme et al., 2012a; Péroux et al., 2011). These have resulted in a handful tentative detections at $z < 1$ (Chen and Lanzetta, 2003; Lacy et al., 2003; Le Brun et al., 1997; Rao et al., 2003; Steidel et al., 1995; Turnshek et al., 2001), but the issue of what the host galaxies of DLAS are is not yet fully resolved.

One of the observables for DLAS with both radio and HI observations is the spin temperature of HI (Wolfe and Davis, 1979). The measured spin temperature in DLAs are found to be higher than typical spin temperature of HI found in local spiral galaxies (Carilli et al., 1996; Kanekar and Chengalur, 2003; Wolfe and Davis, 1979) but similar to what could be expected in dwarf galaxies (Chengalur and Kanekar, 2000; Kanekar et al., 2009). From absorption studies, another observable is $f(\mathrm{N_{HI}})$, which gives the expected numbers of absorbers with HI column density between $\mathrm{N_{HI}}$ and $\mathrm{N_{HI}}$+$\mathrm{dN_{HI}}$ per unit distance. $f(\mathrm{N_{HI}})$is one of the few statistics which can be calculated for both

the galaxies in local universe and DLAS. As discussed earlier, in hierarchical structure formation model small galaxies are expected to dominate the galaxy population at high redshifts. It would hence be interesting to check if the $f(N_{HI})$ of dwarf galaxies in the local volume matches that observed in high redshift DLAS.

1.3 Vertical HI distribution in dwarf galaxies

The vertical scale height of HI in a disk galaxy would be set by the balance between the vertical momentum flux and the gravitational force. The HI self gravity, the gravity of molecular gas, stars and the the dark matter halo all contribute to the vertical component of the gravitational force. (Narayan and Jog, 2002a) have computed the scale height of the stars, H_2 and HI using such a hydrostatic equilibrium model, and find that their model is a good match to the observations.

It would be interesting to try and apply such models to dwarf galaxies. A direct observation of HI scale height is difficult for various reasons even for a perfectly edge-on galaxy, unless the scale height is constant with radius and the gas in optically thin (Sancisi and Allen, 1979). Banerjee et al. (Banerjee et al., 2011b) studied four dwarf galaxies DDO154, Ho II, IC 2574 and NGC 2366 to predict the HI scale height theoretically using the self-consistent model of (Narayan and Jog, 2002b). The HI velocity dispersion is one of the key input parameters in their model. A $\sim 10\%$ change in the velocity dispersion leads to a $\sim\ 14-15\%$ change in the computed scale height. In their model (Banerjee et al., 2011b) assumed a constant velocity dispersion to predict the HI scale height (except for IC 2574 and Ho II for which a smoothly declining σ profile is used from (Tamburro et al., 2009)). (Tamburro et al., 2009) used second moment of the HI data cube as a measure of velocity dispersion. The second moment map represents the intensity weighted average dispersion on velocity along a line-of-sight and need not accurately reflect the true dispersion of HI . Similarly using a constant σ also does not have any clear theoretical basis (Tamburro et al., 2009).

In chapter 4, we address the vertical distribution of HI gas in the dwarf galaxy KK250 from FIGGS survey (Begum et al., 2008). Following the same prescription of (Narayan and Jog, 2002b) (Banerjee and Jog, 2008; Banerjee et al., 2011a; Narayan et al., 2005, later) we treat the dwarf galaxy as a gravitationally coupled two component (stars and HI) system in hydrostatic equilibrium in an external field of dark matter

halo and solve for the HI density as a function of the height from the mid-plane. In this model we treat the velocity dispersion of gas 'σ_{gas}' as a free parameter and chose the best model describing HI observation by χ^2 minimization.

1.4 Gas and star-formation

Theoretical models of the atomic ISM (Field et al., 1969; Wolfire et al., 1995a) indicate that the HI should exist in two phases, a cold dense phase (Cold Neutral Medium or CNM) and a warm diffuse phase (Warm Neutral Medium or WNM). The typical temperature of the CNM is $\sim$ 100K, while the typical temperature of the WNM is $\sim$ 5000$-$8000K. Observations of HI in our galaxy, as well as in external spiral galaxies does provide support for this model. In dwarf galaxies, the presence of a cold ("CNM") phase has traditionally been inferred by decomposing the HI emission profiles into multiple Gaussians and identifying narrow components with emission from the CNM (Warren et al., 2012; Young and Lo, 1997; Young et al., 2003). The gaussian fits typically return a mix of broad components (with a velocity dispersion of 8 - 13 km s^{-1}) and narrow components (with velocity dispersion of 3 - 5 km s^{-1}). We use a similar technique to try and identify cold HI in our sample of galaxies. Though the Gaussian Decomposition technique is widely used to identify narrow width cold HI , it has several drawbacks. Firstly, Gaussian do not form an orthogonal basis and hence any decomposition is not unique. Secondly, it is not clear that components identified in this manner necessarily correspond to physically distinct clouds. Extra galactic and galactic studies reveal that the emission brightness of HI gas is tightly coupled with the opacity of the gas. In the Galaxy, any line-of-sight having brightness temperature (T_B) more than 5 K found to be associated with significant absorption, i.e. has a large optical depth. Large optical depths in turn typically arise from the low spin temperature CNM phase. We hence try a second method for identifying the CNM phase in our dwarf galaxies, based on the observed brightness temperature. Similar studies have earlier been done for nearby spiral galaxies (Braun and Walterbos, 1992), but, to the best of our knowledge, there has been no such previous study in dwarfs.

We then study the correlation of the cold HI found by these two methods with the total HI column density distribution, as well as regions of recent star formation. In many previous studies (Bigiel et al., 2010; Kennicutt, 1998; Roychowdhury et al.,

2009, 2011) of spiral and dwarf galaxies it has been found that the star formation rate density and gas surface density are related by a power law (generally termed as the 'Kennicutt-Schmidt' law) as given below -

$$\Sigma_{gas} = A(\Sigma_{SFR})^N \tag{1.1}$$

where 'N' is the power-law index and 'A' is the normalising constant. The earliest such studies were carried on large spiral galaxies by averaging the surface densities over the entire optical disk and estimated the value for 'N' to be 1 - 2 (e.g. Kennicutt, 1997). As the star formation and the gas surface densities were averaged over the entire star forming disk, the results found by these studies could be interpreted in terms of different global parameters of a galaxy such as large scale instabilities, differential rotation, density waves etc. Studies of the relationship on local scales could reflect the effect of different ISM conditions on star formation.

A number of recent studies used radial profiles of gas densities and star-formation rate densities to constrain the Kennicutt-Schmidt law (Eqn. 1.1) on local scales (e.g. Boissier et al., 2003; Martin and Kennicutt, 2001; Schuster et al., 2007). Most of these studies were skewed towards large spirals (Dalcanton et al., 2009; Gil de Paz et al., 2007; Kennicutt et al., 2003; Leroy et al., 2009; Walter et al., 2008). Only recently have there been studies (Bigiel et al., 2010; Roychowdhury et al., 2009, 2011) focused on dwarf galaxies where the ISM has much lower metallicity and dust content. It would be interesting to check the relationship between the cold HI that we find in our dwarf galaxies and the star formation rate, to see if one can find a similar kind of power law relation between the star formation rate and the cold gas density.

1.5 Outline of the thesis

In this thesis we study different aspects of HI in star-forming dwarf galaxies. We used data from **F**aint **I**rregular **G**MRT **G**alaxies **S**urvey (FIGGS) (Begum et al., 2008) along with fresh observations of 21 nearby dwarf galaxies with the GMRT (FIGGS2). In chapter 2, we describe our observations, data analysis and preliminary results of the FIGGS2 survey. The primary aim of this survey is to build a comprehensive sample of faint gas rich dwarf galaxies with multi wavelength data.

In chapter 3 we try to determine if galaxies like the local dwarf galaxies could form the host population of high redshift DLAS found in quasar absorption spectra. High redshift DLAS contain the bulk of neutral gas ($> 80\%$) at high redshifts. In that sense they are the precursors of the current day population of gas rich galaxies. However, in spite of decade long studies the nature of these DLAS hosts are still not clearly understood. In chapter 3 we estimate the column density distribution function $f(\mathrm{N_{HI}})$ of dwarf galaxies in the local universe and compare it with the $f(\mathrm{N_{HI}})$ of high redshift DLAS, to see if the dwarf galaxies could be the hosts of the high redshift DLAS.

The vertical structure of the HI disk of dwarf galaxies plays a significant role in the galaxy evolution process. For example, a thicker HI disk will prevent early breakout of HI shells produced by supernovae. In chapter 4 we model the vertical HI distribution of an edge-on galaxy KK250 assuming vertical hydrostatic equilibrium between different baryonic components under the external force field of a fixed dark matter halo. This allows us to measure both the scale height of the HI disk (as a function of radius) as well as the velocity dispersion of the gas (again as a function of radius).

In chapter 5 we study the phase structure of the HI in dwarf galaxies. We describe a routine that was developed to automatically decompose line-of-sight HI emission spectra into multiple Gaussian components and identify narrow components. We characterise the performance of this routine and compare it those used in earlier studies. We also used the HI brightness temperature (as measured on ~ 100 pc scales) to identify gas in the CNM phase. We compare these two different methods of identifying cold HI to try and determine which of them is better suited for dwarf galaxies.

In the chapter 6 we investigate the connection of the cold HI with recent star-formation. We use both FUV emission as well as Hα emission as tracers of recent star formation. Finally in chapter 7 we present a summary of the thesis and describe possible future extensions of the work presented here.

2

FIGGS2: An HI survey of extremely faint irregular galaxies

2.1 Introduction

While there have been a number of multi-wavelength surveys of samples of large spiral galaxies (Dalcanton et al., 2009; Gil de Paz et al., 2007; Kennicutt et al., 2003; Leroy et al., 2009; Walter et al., 2008), the number of detailed studies of faint gas-rich dwarf galaxies are quite small, although the situation is changing rapidly. Recent surveys of dwarf galaxies include VLA-ANGST (Ott et al., 2012), FIGGS (Begum et al., 2008), SHIELD (Cannon et al., 2011) and LITTLE-THINGS (Hunter et al., 2012). There are a number of issues that make systematic studies of dIrr galaxies particularly interesting. Firstly, in hierarchical models of galaxy formation, small objects form first and merge together to form larger objects. In that sense, nearby dwarf galaxies are the closest analogues to the galaxies in the early universe. Secondly, the ISM of dwarf galaxies have low metallicity. In this sense too, they are analogous to high redshift galaxies, and serve as a nearby laboratory for the study of gas and star formation in environments with low dust and low metallicity (Roychowdhury et al., 2009, 2011).

In this chapter we describe an extension to the FIGGS (Begum et al., 2008) survey to even fainter galaxies. We present here the results of our HI observations of 21 ultra-faint galaxies with the Giant Meterwave Radio Telescope (GMRT). In §2 we describe our sample, in §3 we explain the main science drivers of the survey, in §4 we present the observations and data analysis and finally in §5 we present the results and discussion.

2.2 Sample

The FIGGS2 survey was planned as an extension of the Faint Irregular Galaxy GMRT Survey (FIGGS) (Begum et al., 2008). The FIGGS sample was based on the 2004 version of a compilation of nearby galaxies (Catalogue of Nearby Galaxies (Karachentsev et al., 2004)). Since then there has been an almost two fold increase in the known number of faint galaxies in the local neighbourhood, thanks to surveys like the SDSS (Abazajian et al., 2009) and ALFALFA (Giovanelli et al., 2005). In the FIGGS2 survey we focus on the faintest end of the galaxy spectrum, viz. galaxies fainter than $M_B = -12$. The cutoff magnitude for the FIGGS sample was $M_B = -14.5$ and the sample contained ~ 11 galaxies fainter than $M_B = -12$. The FIGGS2 sample consists of 21 galaxies with $M_B \gtrsim -12.0$, and $S_{HI} > 0.5$ Jy km/s which combined with FIGGS galaxies leads to a ~ 3 times larger sample of galaxies fainter than $M_B = -12.0$ than was earlier available.

In Table 2.1 we list a few general properties of our sample galaxies. The columns are as follows: column (1): Galaxy name, column (2) and (3): the equatorial coordinates (J2000), column (4): the absolute blue magnitude (extinction corrected), column (5): log of HI mass, column (6): The Holmberg diameter, column (7): Distance in Mpc, column (8): the methods used to determine the distances to the galaxies, - by the tip of the red giant branch (TRGB), by the Hubble velocity-distance relation ($H_0 = 73$ km/s/Mpc) (h), from galaxy membership (mem), by the Tully-Fisher relation (TF), by the texture of the object (txt) (One galaxy in our sample (KK191) does not have any optical or HI measurement due to its low optical surface brightness and HI deficiency. The texture of this object indicates its likely proximity, which can be verified later by HST observation or by HI observations), column (9): inclination derived from optical photometry (assuming an intrinsic thickness of 0.2). The data presented in Table 2.1 are taken from (Karachentsev et al., 2013).

Table 2.1: Sample galaxy properties

Galaxy	α (J2000) (hhmmsss)	δ (J2000) (^{o} $'$ $''$)	M_B (mag)	$\log M_{HI}$ ($M_\odot$)	V_{hel} km s^{-1}	D_{opt} (arcmin)	Distance (Mpc)	Method	i_{opt} (^{o})
AGC112521	014107.9	+271926	−11.6	6.82	274	0.60	6.58	TRGB	67
KK15	014641.6	+264805	−11.9	7.24	366	0.59	9.04	TRGB	90
KKH37	064745.8	+800726	−11.6	6.70	11	1.15	3.39	TRGB	55
KKH46	090836.6	+051732	−11.9	7.28	598	0.60	5.60	h	34
UGC4879	091602.2	+525024	−11.9	5.98	−25	3.24	1.36	TRGB	66
LeG06	103955.7	+135428	−11.9	6.85	1007	0.63	10.40	mem	57
KDG073	105257.1	+693245	−10.8	6.51	116	1.20	3.70	TRGB	38
VCC0381	121954.1	+063957	−11.7	7.14	480	0.78	4.71	h	26
KK141	122252.7	+334943	−12.9	7.20	573	0.40	7.78	h	45
KK152	123324.9	+332105	−13.0	7.54	838	1.07	6.90	TF	83
UGCA292	123840.0	+324600	−11.8	7.44	308	1.02	3.61	TRGB	52
BTS146	124002.1	+380002	−12.2	6.97	446	0.34	8.50	TF	67
LVJ1243+4127	124355.7	+412725	−11.8	7.02	402	1.38	6.09	h	83
KK160	124357.4	+433941	−10.9	6.59	293	0.59	4.31	TRGB	47
KKH86	135433.6	+041435	−10.3	5.91	287	0.85	2.59	TRGB	51
LeG18	104653.3	+124440	−11.3	7.15	636	0.28	10.40	mem	47
KDG090	121457.9	+361308	−11.67	7.66	280	1.55	2.86	TRGB	33
LJV1424345	104952.2	+130942	−10.24	−	754	0.1	10.4	mem	26
LVJ1217+4703	121710.1	+470349	−11.0	< 6.44	394	0.30	7.80	mem	46
KK138	122158.4	+281434	−10.4	< 6.25	449	0.42	6.30	mem	64
KK191	131339.7	+420239	−10.8	< 6.21	371	0.42	6.00	txt	18

In Figure 2.1 we plot histograms of various global properties of our sample galaxies. In panel [A] we plot the histogram of absolute blue magnitude M_B, panel [B] shows the histogram of log of HI mass, panel [C] and [D] shows the histograms of distances to the sample galaxies and the HI mass to blue luminosity ratio (M_{HI}/L_B). Most of our sample galaxies have $M_B \gtrsim -12.0$ (the distances to some of our galaxies have been updated after the sample selection was done) with a median of -11.7 which is more than one magnitude fainter than the median of the FIGGS sample. Panel [B] shows the histogram of log of HI mass of our sample galaxies. The median HI mass of our sample galaxies is $\sim 5.6 \times 10^6$ $M_\odot$ which is also about an order of magnitude lower than the median HI mass of FIGGS sample. From Figure 2.1 one can see that our sample spans around two orders of magnitude in brightness and about 3 orders of magnitude in HI mass. From Figure 2.1 we clearly see that there is no particular bias on the selection criteria of our sample galaxies. Our sample galaxies are almost uniformly distributed over the distance of 10 Mpc. Though there is no visible trend in different global properties of our sample galaxies, it is still a flux limited sample as our samples are selected on the basis of luminosity. It is a representative sample of dwarf galaxies though the completeness is not entirely assured.

2.3 Science drivers for FIGGS and FIGGS2

The primary goal of the FIGGS2 survey was to extend the previous FIGGS survey towards the fainter end and enrich the multi wavelength database to address several science questions. A few key science drivers of FIGGS2 are discussed below.

2.3.1 ISM, star formation and feedback

The neutral ISM and its connection with the star-formation in gas-rich dwarf irregular galaxies has been a major area of interest for a long time. Star formation in these low dust, low metallicity environments is expected to proceed differently than in spiral galaxies. Though a number of studies using FIGGS data have already explored many aspects of star formation (see for example, Roychowdhury et al., 2009, 2011), yet a number of interesting questions still remain to be answered; like star formation feedback and its effect on star-formation in smallest scales, abundance of the different ISM phases and its connection with star formation etc. Very often the total measured Hα emission

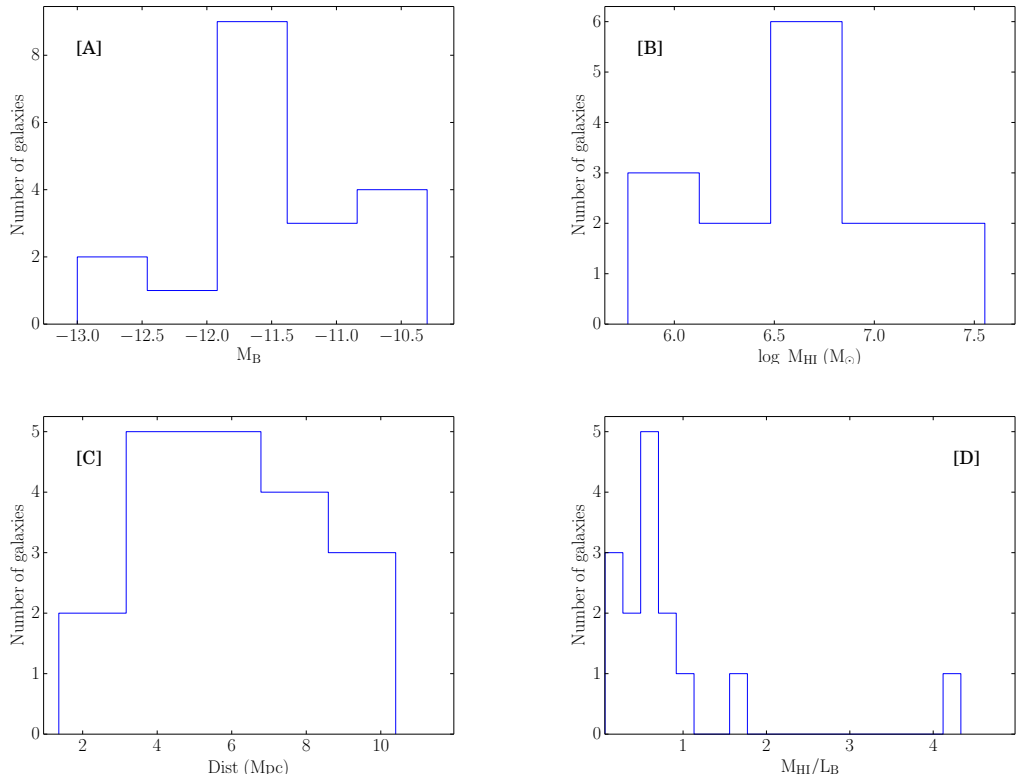

Figure 2.1: Histograms of different global properties of our sample. Panel [A] shows the histogram of extinction corrected absolute blue magnitude (M_B), panel [B] represents the histogram of log of HI mass of our sample galaxies, panel [C] shows the histogram of distances and in panel [D] we show the histogram of the HI mass to blue luminosity ratio (M_{HI}/L_B).

in these galaxies can be accounted for by only a few massive stars. Due to very shallow potential well of these galaxies, the ISM and cold gas are expected to be strongly affected by star formation feedback. A comparison of the HI and optical morphologies could allow one to examine the consequences of this feedback in the smallest gas-rich galaxies.

2.3.2 Dynamics and Dark matter halos

The other major scientific aim of this survey was to understand the structure of the dark matter halo and its influence on the dynamics of dwarf galaxies. The dark matter halo is believed to influence not only the dynamics but also the structure and course of evolution of galaxies (Banerjee and Jog, 2008; Banerjee et al., 2010; Saha and Maciejewski, 2013).

The vertical structure and scale-height of galaxies is determined by the hydrostatic equilibrium between different galactic components (e.g. Narayan and Jog, 2002a) embedded in the dark matter halo. This vertical hydrostatic equilibrium decides in turn the thickness and the vertical structure of the galactic disk. The thickness of galactic disks has many implications in cosmological context (Patra et al., 2013) as well as in galaxy evolution. Observationally it is found that the gas disks of small gas-rich galaxies (like our sample) are thicker than normal spirals (Roychowdhury et al., 2010). However a complete theoretical understanding of this higher thickness and the vertical structure of the gas disc of dwarf galaxies is not yet available. One of the aims of this study is to measure the vertical structure of gas disks and use this to constrain the dark matter distribution. Though this is a future work with FIGGS and FIGGS2 sample which was not realised in this thesis. Instead we developed a method to measure the vertical structure of gas disks in galaxies and to independently estimate gas velocity dispersions in low mass dwarf galaxies.

2.4 Observation & data analysis

For all our observations we used the newly installed GMRT Software Back-end (GSB) instead of the old GMRT Hardware Back-end (GHB). A bandwidth of 2.08 MHz with 256 channels or a 4.17 MHz with 512 channels were used keeping the spectral resolution constant at $\sim$ 8.1 KHz (velocity width of $\sim$ 1.7 km s^{-1}). In every observing run flux

calibration and bandpass calibration were done by observing standard flux calibrators 3C48, 3C147 or 3C286 at the starting and at the end of the observation. The phase calibration were done by observing a phase calibrator from the VLA list of calibrators within an angular distance of $\lesssim 10^o$ of the source once in every 45 minutes.

Typically about 6 hrs of time was alloted for a single observation, with the actual on-source time varying between $\sim$ 2-5 hrs. All data were reduced in classic AIPS. For every galaxy, phase and bandpass calibration were applied to the data after editing bad visibilities. Online doppler tracking was not done during observation, hence the data were corrected for earth's motion using AIPS task CVEL. The GMRT has a hybrid configuration (Swarup et al., 1991) with 12 antennas inside the central square (2 km $\times$ 2 km) and 18 antennas spread over $\sim$ 25 km area in an approximate "Y" shaped array. Due to its hybrid configuration, GMRT is capable of sampling both the small and large angular scales within a single observing run. The longest achievable baseline at 21cm wavelength is $\sim$ 120 kλ. Image cubes at different resolutions were made using the task IMAGR in AIPS by using natural weighting and different values of uvrange and uvtaper. The continuum subtraction was done in image plane using the task IMLIN and clean cubes were generated using APCLN. Low resolution channel maps were first inspected manually to determine all channels with emission and subsequent moment images were made using these channels.

Total intensity images at different resolutions are very important for exploring the physics of the ISM and the dynamics at different scales. For example the effect of local processes like star formation are best studied using high resolution images, whereas the large-scale dynamics are better studied using low resolution images. As an example, in Figure 2.2 we show integrated HI emission images of one of the FIGGS2 sample galaxies, (viz. UGC 4879) at different spatial resolutions. The galaxy shows a faint extended structure at the south-west corner in low resolution image (panel [A]) which is resolved out at higher resolution. On the other hand, the fine details of the morphology of the galaxy in the central region can be more clearly seen in the high resolution images.

We detected HI emission in 15 out of 21 galaxies. Three (LeG18, LJV1424345, LVJ1217+4703) out of the six non-detections have quite large single-dish peak fluxes ($>$ 25 mJy (Huchtmeier et al., 2009)). However their GMRT observations were affected by strong RFI and a significant fraction of the data had to be flagged, resulting in higher noise levels in the data cube. Despite these increased noise level, one would have

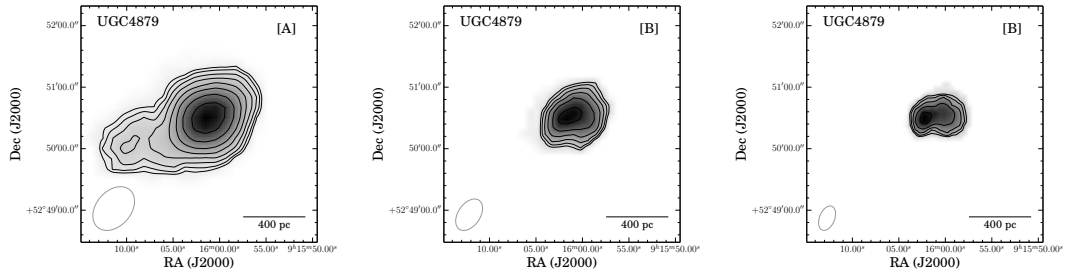

Figure 2.2: Integrated HI emission from UGC 4879 at different spatial resolutions. The resolution of the images are $48'' \times 34''$ (panel [A]), $34'' \times 21''$ (panel [B]), $25'' \times 14''$ (panel [C]). The contour levels are (1, 1.4, 2, 2.8, ..) 2×10^{19} in panel [A], (1, 1.4, 2, 2.8, ..) 6×10^{19} in panel [B] and (1, 1.4, 2, 2.8, ..) 1×10^{20} in panel [C].

expected to see the HI emissions at the 3σ level so, the non detections are surprising, if the single dish fluxes are correct. In the case of KDG90, although the quoted single dish flux is quite high ($\sim$ 23.6 Jykm s^{-1}(Koribalski et al., 2004)), VLA observations (VLA-ANGST survey, (Ott et al., 2012)) also did not detect any emission from this galaxy. The single dish HI spectra for KK138 has a velocity width of 186 km s^{-1} and a very low peak flux of $\sim$10 mJy. Such a large velocity width is not expected for dwarf galaxy; it seems likely that the single dish detection is spurious. In the case of KK191 there is a large spiral galaxy NGC5055 within an angular distance of $\sim$ $25'$. NGC5055 has a central velocity of 510 km s^{-1} and a velocity width of $\sim$ 400 km s^{-1} which overlaps with the quoted velocity for KK191, i.e. 368 km s^{-1}(Huchtmeier et al., 2000). Hence it is possible that the single dish detection is confused.

Table 2.2: Observation details

Galaxy name	Date of observations	velocity coverage (km s^{-1})	Time on source (Hr)	Synthesized beam (arcsec^2)	Single channel rms (mJy/beam)
AGC112521	December 10, 2010	$-145-734$	6	$40.64\times35.75,\ 27.85\times22.56,\ 13.91\times10.55$	2.0, 1.5, 1.3
KK15	November 14, 2010	$5-886$	4	$44.28\times36.50,\ 27.35\times24.03,\ 15.02\times11.39$	1.4, 1.1, 0.9
KKH37	December 29, 2010	$-643-234$	5.3	$54.40\times35.55,\ 25.98\times19.19,\ 12.14\times9.85$	3.5, 2.6, 1.6
KKH46	December 10, 2010	$251-1133$	3.8	$43.26\times36.75,\ 30.03\times25.91,\ 26.54\times10.51$	3.0, 2.7, 2.0
UGC4879	August 06, 2010	$-154-56$	3.8	$48.16\times34.03,\ 34.18\times21.52,\ 25.02\times14.78$	3.8, 3.2, 2.8
LeG06	October 15, 2010	$831-1272$	6.8	$45.00\times38.07,\ 26.95\times22.50,\ 12.40\times10.71$	3.8, 3.0, 1.1
KDG073	March 14, 2009	$-19-191$	6.75	$45.32\times35.45,\ 28.42\times22.00,\ 14.44\times10.60$	2.8, 1.7, 1.5
VCC0381	August 08, 2010	$273-714$	4.5	$45.28\times35.57,\ 31.87\times23.50,\ 23.40\times10.27$	3.1, 2.9, 2.5
KK141	November 14, 2010	$37-919$	4.5	$44.49\times35.97,\ 30.14\times24.39,\ 13.31\times9.38$	2.1, 1.8, 1.5
KK152	August 09, 2010	$494-1377$	4.5	$44.21\times33.60,\ 29.53\times21.46,\ 16.15\times9.71$	3.7, 3.2, 2.5
UGCA292	December 10, 2010	$-171-708$	4.5	$45.22\times35.23,\ 27.79\times23.95,\ 15.09\times11.84$	2.6, 2.5, 1.9
BTS146	December 11, 2010	$39-920$	5.25	$44.28\times34.73,\ 30.92\times21.58,\ 16.29\times11.23$	1.1, 0.8, 0.7
LVJ1243+4127	January 02, 2011	$-69-811$	3.75	$49.86\times35.72,\ 26.71\times20.43,\ 13.92\times10.12$	3.2, 2.6, 2.0
KK160	December 31, 2010	$-104-775$	4.4	$49.27\times35.55,\ 28.43\times21.65,\ 14.01\times9.93$	2.9, 2.3, 1.5
KKH86	November 13, 2008	$181-392$	5.25	$43.20\times35.01,\ 34.17\times23.83,\ 29.53\times14.45$	2.6, 2.3, 1.8
LeG18	December 11, 2010	$466-1350$	3.75	$87.52\times35.10,\ 73.18\times23.85,\ 62.30\times9.21$	7.4, 9.0, 6.3
KDG090	March 14, 2009	$155-366$	3.3	$70.04\times33.61,\ 59.18\times20.04,\ 46.17\times16.54$	6.3, 4.1, 2.9
LJV1424345	August 12, 2010	$623-1064$	4.5	$70.04\times33.61,\ 59.18\times20.04,\ 46.17\times16.54$	7.5, 8.3, 20.5
LVJ1217+4703	August 07, 2010	$183-623$	4.4	$49.20\times37.41,\ 47.16\times35.0,\ 44.06\times33.61$	4.7, 7.7, 12.1
KK138	December 31, 2010	$39-920$	4.5	$42.10\times40.14,\ 27.50\times23.83,\ 11.91\times9.51$	1.8, 1.7, 1.7
KK191	August 13, 2010	$3-884$	4.5	$56.76\times34.50,\ 46.54\times18.22,\ 33.38\times11.72$	4.9, 4.3, 6.6

The observation details and analysis results are presented in Table 2.2. The columns are as follows: column (1): the galaxy name, column (2): date of observation, column (3): the velocity (heliocentric) coverage of the observing band, column (4): on-source time in hour, column (5): synthesized beam size at different resolution data cubes, column (6): corresponding single channel rms.

2.5 Results & Discussion

The global HI spectra of our sample galaxies are shown in Figure 2.3. As our sample galaxies are very faint, the global spectra at $\sim$ 1.8 km s^{-1} resolution some times has a very low SNR. Hence adjacent channels were collapsed together to increase SNR wherever necessary. The velocity resolutions used for the different galaxies are shown in the respective panels of Figure 2.3. The parameters derived from the global spectra are listed in Table 2.3. The columns are as follows: column (1) the galaxy name, column (2) The integrated flux with error, column (3) systematic velocity (V_{sys}), column (4) the velocity width at 50 percent of the peak flux (Δ_{50}), column (5) The HI diameter derived by ellipse fitting at a column density, $N_{HI} = 2 \times 10^{19}$ atoms cm^{-2}, column (6) the ratio of the HI diameter to the Holmberg diameter, column (7) the derived HI mass, column (8) mass to light ratio (M_{HI}/L_B), column (9) the ratio of GMRT flux to single dish flux, column (10) HI inclination assuming an intrinsic thickness of 0.6 (Roychowdhury et al., 2010).

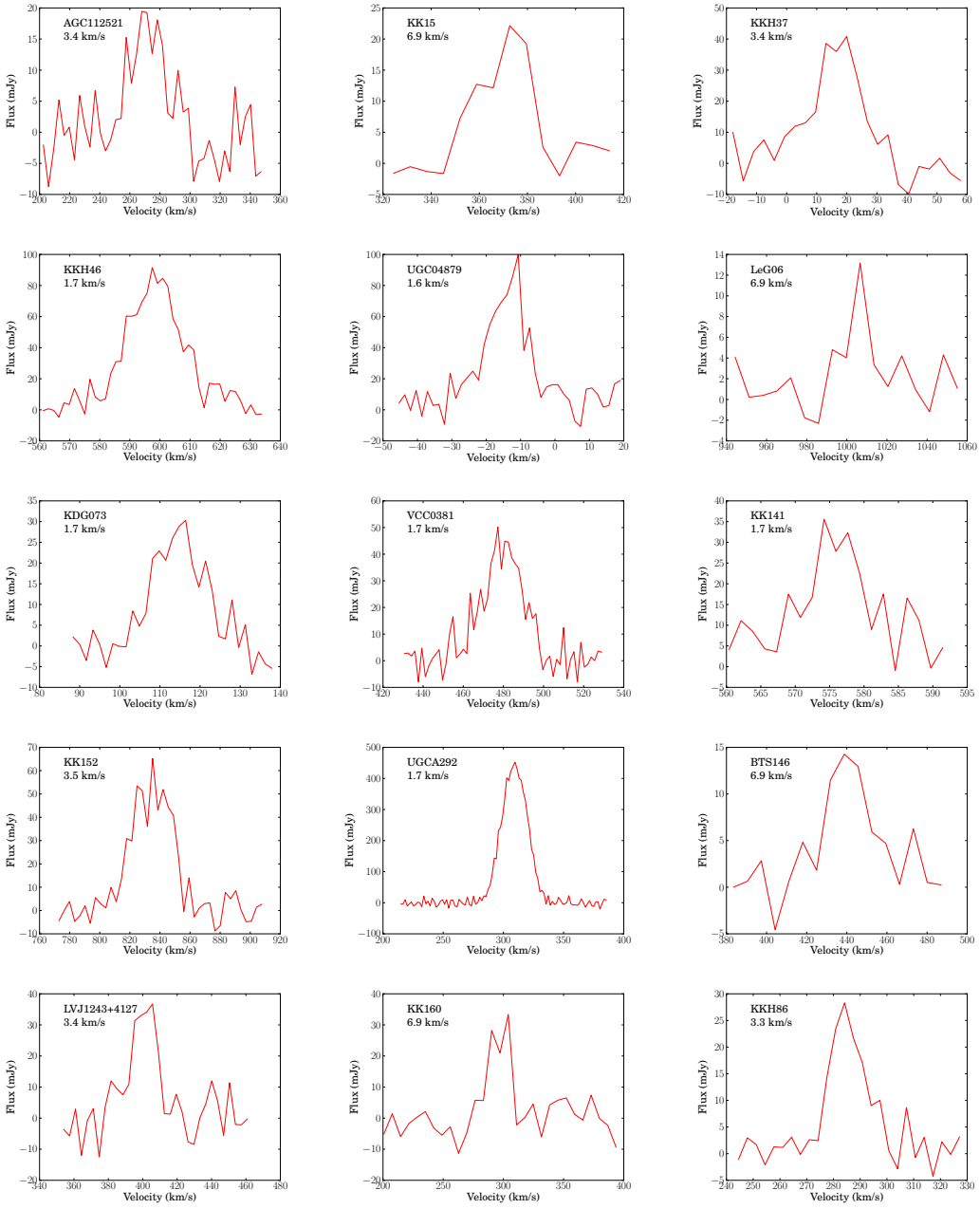

Figure 2.3: Global HI spectra of our sample galaxies. To increase the SNR, multiple channels were collapsed together wherever necessary. The velocity resolution used is quoted in the respective panels.

Table 2.3: Results from the GMRT observations of FIGGS2 sample galaxies

Galaxy	FI_{GMRT} (Jy km s^{-1})	V_{sys} (km s^{-1})	ΔV_{50} (km s^{-1})	D_{HI} (arcmin)	D_{HI}/D_{opt}	M_{HI} ($M_\odot$)	M_{HI}/L_B	$FI_{GMRT}/FI^{\dagger}_{SD}$	i_{HI} (^{o})
AGC112521	0.44 ± 0.34	270.4	25.0	1.43	2.4	$4.46e+06$	0.65	0.7	44
KK15	0.52 ± 0.19	371.3	23.8	1.61	2.7	$1.00e+07$	1.11	0.6	55
KKH37	0.70 ± 0.13	17.4	17.2	1.69	1.5	$1.90e+06$	0.28	0.2	54
KKH46	1.96 ± 0.47	598.2	21.2	2.17	3.6	$1.45e+07$	1.60	0.8	45
UGC4879	1.35 ± 0.66	-13.2	14.2	2.19	0.7	$5.86e+05$	0.06	0.5	72
LeG06	0.22 ± 0.37	1005.9	16.3	1.25	2.0	$5.59e+06$	0.62	0.8	78
KDG073	0.40 ± 0.18	114.6	14.2	1.59	1.3	$1.28e+06$	0.39	0.4	51
VCC0381	1.07 ± 0.30	479.8	22.9	1.57	2.0	$5.59e+06$	0.74	0.4	34
KK141	0.43 ± 0.18	576.0	14.5	1.22	3.0	$6.12e+06$	0.27	0.4	38
KK152	1.78 ± 0.37	834.7	30.5	1.97	1.8	$2.00e+07$	0.80	0.6	63
UGCA292	11.67 ± 0.62	309.2	24.6	3.40	3.3	$3.58e+07$	4.35	1.3	37
BTS146	0.39 ± 0.15	440.5	25.5	1.20	3.5	$6.62e+06$	0.56	0.7	37
LVJ1243+4127	0.62 ± 0.53	403.2	16.5	1.73	1.3	$5.41e+06$	0.66	0.5	65
KK160	0.51 ± 0.53	301.6	20.0	1.70	2.9	$2.22e+06$	0.62	0.6	75
KKH86	0.45 ± 0.16	285.0	15.1	1.52	1.8	$7.11e+05$	0.34	0.9	55

† Single Dish Flux were taken from the Lyon Extragalactic Database (LEDA).

To estimate the HI diameter, we first define an isophotal contour of $N_{HI}= 2 \times 10^{19}$ atoms cm^{-2}as an indicator of HI extent in our sample galaxies. We then fit an ellipse to this isophotal contour to estimate the HI diameter and HI inclination of the galaxies. To estimate the HI inclination, we used an intrinsic thickness of 0.6 (Roychowdhury et al., 2010). In Figure 2.5 we plot the histogram of HI diameters of our sample galaxies. To compare the extent of HI disks with their optical counterparts, we normalised the HI diameter by the Holmberg diameter of the galaxies. The mean value of normalised HI diameter is 2.26 which is similar to the value found for the FIGGS (Begum et al., 2008) sample i.e. 2.40. From our data, in general; the HI disks extend more than the optical disk which is a common trend in all galaxies except one. For the galaxy UGC4879, the HI disk found to be smaller than its optical disk. From Figure 2.4 (5th panel) we note that, a faint extended HI emission is seen in the south-west corner, which may be indicative of diffuse emission not picked up in our observations. It is worth noting that in this case the GMRT observation picksup only about 50% of the single dish flux.

In galaxies, HI can only exist within a small range of column densities. At high column densities it gets converted into molecular H_2 and in very low column densities it gets ionized by background radiation. Due to this constraint only a relation between HI diameter and HI mass is expected. In Figure 2.6 we show the tight correlation between the HI diameter and the HI mass of our sample galaxies. The filled triangles represent FIGGS2 data and the red dotted line is the linear fit to the data. The black line represents FIGGS data from (Begum et al., 2008). The best fit linear relation is

$$\log(M_{HI}) = (2.27 \pm 0.29) \log(D_{HI}) + (5.77 \pm 0.13) \tag{2.1}$$

Equation 2.1 illuminates an important fact about the average surface density of the HI disks of our sample galaxies. A constant slope of 2.0 refers to an average constant surface density across different galaxies with different HI mass and HI diameter. The slope we find with FIGGS2 galaxies i.e. (2.27 ± 0.29) agrees well with the slope of FIGGS galaxies (1.99 ± 0.11) within error bars. The intercept of FIGGS2 (5.77 ± 0.13) also roughly matches with that of FIGGS (6.08 ± 0.06) data (see Figure 2.6).

In Figure 2.7 we show the $\log(M_{HI}/L_B)$ as a function of M_B. Our sample galaxies are shown by filled blue triangles, whereas the filled red points represent the FIGGS sample. The crosses are from (Warren et al., 2007) and hollow boxes are for galaxies from (Verheijen and Sancisi, 2001). The solid line represents an empirically derived

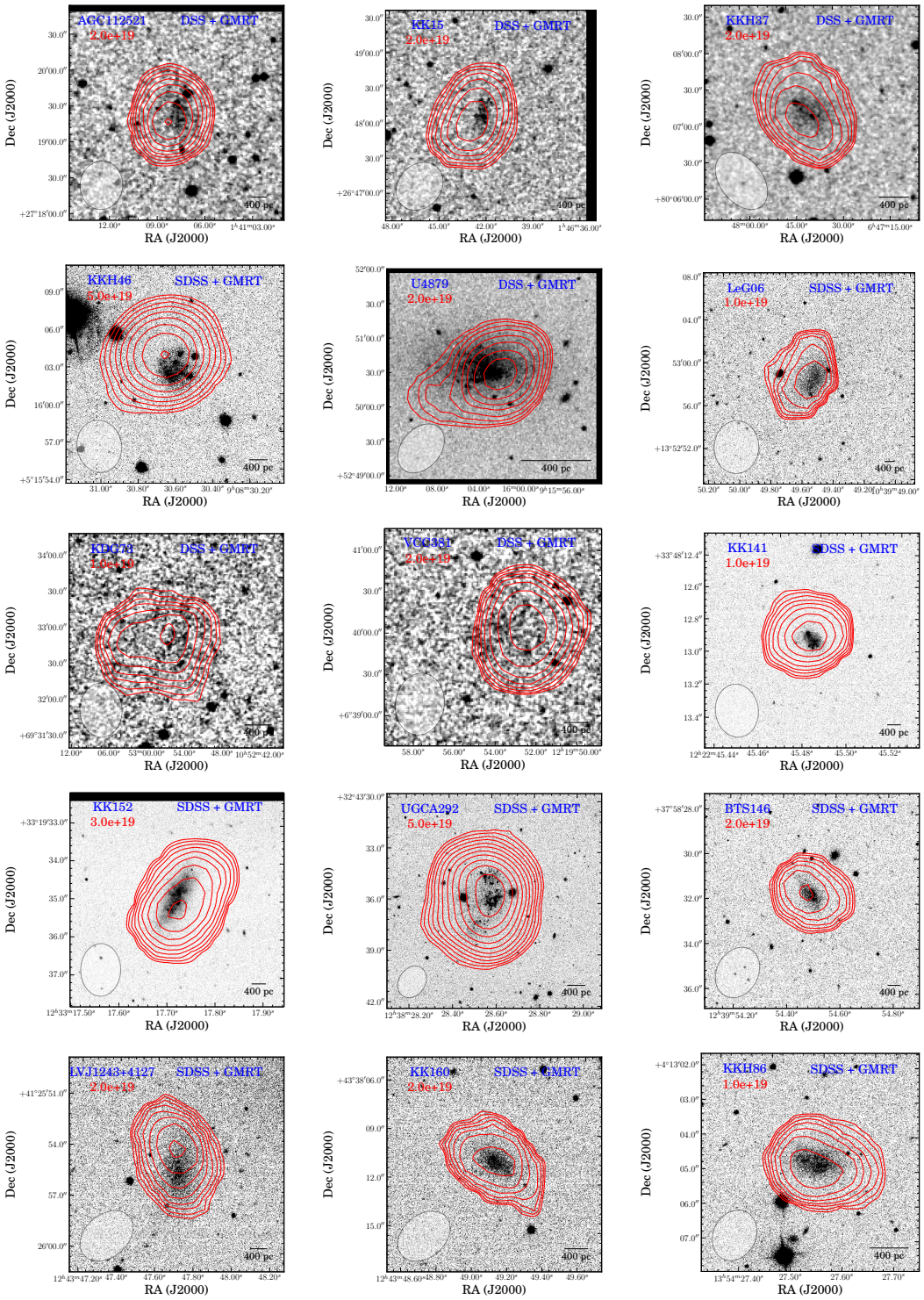

Figure 2.4: Overlays of the integrated HI emission (contours) on the optical image for the FIGGS2 galaxies. The optical images were taken from SDSS (Abazajian et al., 2009) if available, else DSS images were used. The lowest contour levels are quoted in the top left of the respective panels, just below the galaxy name. The contour spacings are in multiples of $\sqrt{2}$.

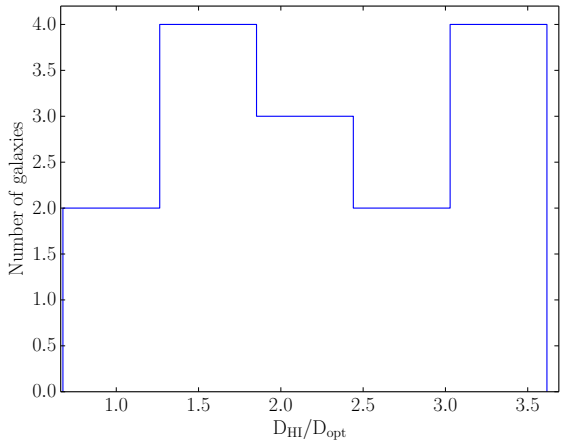

Figure 2.5: Histogram of HI diameters of our sample galaxies normalized to Holmberg diameter. One can see that all our galaxies have HI diameter larger than the optical diameter except one (UGC4879). See the text for more discussion.

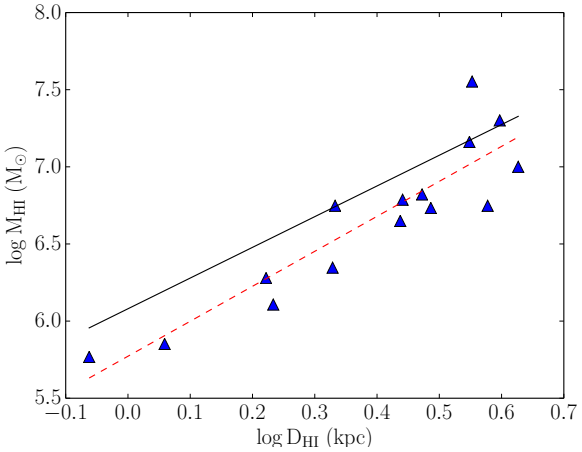

Figure 2.6: The HI mass of the FIGGS2 sample as a function of HI diameter (measured at $N_{HI} = 2 \times 10^{19}$atoms cm^{-2}). The red dashed line represent a straight line fit to the FIGGS2 data and the black solid line represents a fit to FIGGS data taken from (Begum et al., 2008)

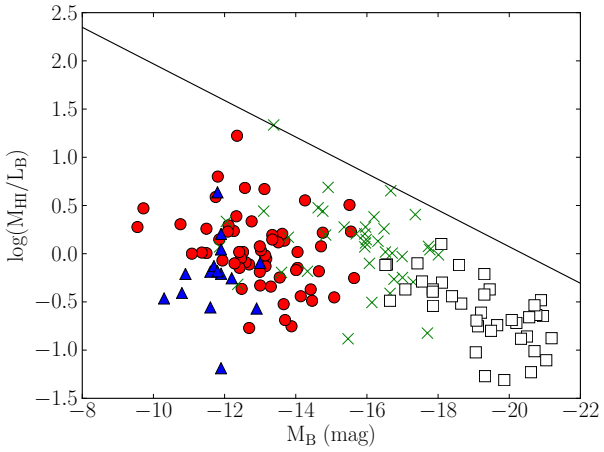

Figure 2.7: The log of HI -mass-to-light ratio as a function of M_B. Blue filled triangles are from FIGGS2, red filled circles are taken from FIGGS survey, green crosses are from (Warren et al., 2007) and hollow boxes are from (Verheijen and Sancisi, 2001). The solid line represents an empirically derived upper limit to M_{HI}/L_B from (Warren et al., 2007). See text for more details.

upper limit to the (M_{HI}/L_B) from (Warren et al., 2007). It can be thought of as a minimum fraction of the baryonic mass to be converted into stars in order to be stable under thermal equilibrium with gravity (Warren et al., 2007) for a galaxy of given baryonic mass. It is interesting to note that all our data points are situated well below the solid line. It implies that these small dwarf galaxies converted much more gas into stars than the minimum required to be stable under the balance of gravity and thermal energy.

In summary we have observed 21 faint galaxies with the GMRT to expand the FIGGS sample towards the low luminosity end. We detected HI emission from 15 of the galaxies. We use these data along with data from the FIGGS sample in the analysis presented in the following chapters.

3

The HI column density distribution function in faint dwarf galaxies

3.1 Introduction

Neutral atomic gas at high redshifts can only be studied via the absorption lines that are produced when a gas cloud happens to lie in front of a more distant quasar[1]. Much of what we know about the HI content of the early universe comes from the study of these absorption line systems. The absorption systems with the highest column densities ($N_{HI} \gtrsim 10^{20.3}$ atoms cm^{-2}), the so called Damped Lyman-α Absorbers (DLAs) are known to contain the bulk of the neutral gas at high redshifts. DLAs are of particular interest because at these column densities self shielding results in the ionised fraction of the gas being small (Wolfe et al., 2005). As such, DLAs represent the most likely progenitors of the gas rich galaxies seen at the current epoch.

Systematic surveys (e.g. Noterdaeme et al., 2009; Prochaska and Wolfe, 2009; Wolfe et al., 1986) have resulted in the discovery of a large number of DLAs. (Noterdaeme et al., 2009) report the discovery of 937 DLAs using data from the SDSS DR7 (Abazajian et al., 2009). However, despite decades of study, the nature of DLAs remains unclear; in particular the size and morphology of these systems remains very poorly

[1]This chapter is based on "The HI column density distribution of dwarf galaxies", Patra et al. MNRAS, 429, 1596 (2013)

constrained by observations. Two extremes of the models that have been proposed are (i) that DLAs arise from large rotating disks, much like the disks of modern day spirals (e.g. Prochaska and Wolfe, 1997; Wolfe et al., 1986) at the one end and (ii) that DLAs arise from small systems analogous to the current day dwarf galaxies at the other (e.g. Haehnelt et al., 1998). Recent numerical simulations suggest a more nuanced picture where a wide range of hosts gives rise to the observed DLAs (see e.g. Cen, 2012; Pontzen et al., 2008).

Because the observable information available for DLAs is limited to the narrow pencil beam illuminated by the background quasar, there is limited scope for quantitative comparisons of the properties of DLAs and gas rich local galaxies. For DLAs with a compact background radio source, the spin temperature of the HI 21cm line can be measured (Wolfe and Davis, 1979). The spin temperature is typically higher than that observed in the disks of nearby spiral galaxies (see e.g. Carilli et al., 1996; Kanekar and Chengalur, 2003; Wolfe and Davis, 1979), but similar to what might be expected in dwarf galaxies with low metallicity and low central pressure (Chengalur and Kanekar, 2000; Kanekar et al., 2009). Another direct observable from the absorption studies is the column density distribution function $f(\mathrm{N_{HI}})$, which gives the expected number of absorbers with HI column density between $\mathrm{N_{HI}}$ and $\mathrm{N_{HI}}$+$\mathrm{dN_{HI}}$ per unit distance. For the local galaxy population also $f(\mathrm{N_{HI}})$ can be computed; this makes it one of the few statistics which can be computed for both the high redshift as well as local populations. Further interest in studying $f(\mathrm{N_{HI}})$ comes from the idea that various physical processes, e.g. the onset of self-shielding, the threshold at which the gas goes from becoming dominantly atomic to dominantly molecular, would affect its shape (Altay et al.). Studies of the evolution of $f(\mathrm{N_{HI}})$ could hence also lead to an understanding of the evolution with redshift of the physical conditions in neutral gas.

In this chapter we present $f(\mathrm{N_{HI}})$ computed from the FIGGS sample (Begum et al., 2008). The FIGGS sample consists of extremely faint gas rich dwarfs; the median HI mass of the galaxies that we use here is only $\sim 1.4 \times 10^7 \mathrm{M_\odot}$. Our data set is complementary to the one used by (Zwaan et al., 2005) to study $f(\mathrm{N_{HI}})$ at $z \sim 0$. Those authors used HI maps of 355 nearby galaxies from the WSRT based WHISP survey to determine $f(\mathrm{N_{HI}})$. Their sample contains a representative mix of galaxy types, albeit being somewhat biased towards early types S0-Sb, which they correct for using a type specific HI mass function. The (Zwaan et al., 2005) study demonstrated that the

cross-section for producing DLAs at $z \sim 0$ is dominated by large spiral galaxies. The $f(\mathrm{N_{HI}})$ that they compute is hence essentially that corresponding to large galaxies. Our current sample excludes large spirals, and the $f(\mathrm{N_{HI}})$ that is computed here corresponds to that in the smallest star forming galaxies. There are a number of reasons why it is interesting to study the $f(\mathrm{N_{HI}})$ in such small galaxies. Firstly, since the gas in dwarf galaxies is dust poor, one would expect the transition from atomic to molecular gas to happen at a higher column density than in spirals (McKee and Krumholz, 2010; Welty et al., 2012). Further, unlike in spiral galaxies the gas in dwarfs is not in a thin, dynamically cold disk (Roychowdhury et al., 2010). For these reasons, it is not apriori obvious that the $f(\mathrm{N_{HI}})$ in dwarf galaxies would be similar to that in large spirals. Finally, in hierarchical models of galaxy formation, small objects form first, and one would expect that the properties of the gas rich objects in the early universe would more closely resemble dwarfs, than large spirals. These are the themes that we explore in the rest of this chapter.

3.2 Description of the Sample and primary data

The data that we use were gathered as part of the FIGGS survey (Begum et al., 2008). The survey used a sample of 65 dwarf galaxies, selected from the (Karachentsev et al., 2004) catalog, that satisfied the following selection criteria: (i) absolute blue magnitude $M_B \geq -14.5$ mag, (ii) HI integrated flux > 1.0 Jy kms^{-1}, and (iii) optical B-band major-axis ≥ 1.0 arcmin. Three of the galaxies in the FIGGS sample were not detected in HI. One galaxy had a companion that was detected in HI, which we also use for our analysis. This leaves us with a total of 63 galaxies from the FIGGS survey. A further 16 fainter local galaxies which satisfy the following selection criteria (i) absolute blue magnitude, $\mathrm{M}_B \geq$ –12.0 mag, and (ii) integrated HI flux ≥ 0.5 Jy kms^{-1} were later added to the sample (chapter 2).

The GMRT has a hybrid configuration (Swarup et al., 1991), i.e. with a mix of short and long baselines. Consequently, images at a range of resolutions can be made from a single GMRT observation. For the FIGGS galaxies we have data cubes and moment maps at resolutions ranging from $\sim 40''$ to $\sim 4''$, corresponding to linear resolutions of 850 pc to 85 pc at the median distance to the galaxies in the sample. For this study we use only those galaxies for which good quality images were available at all resolutions.

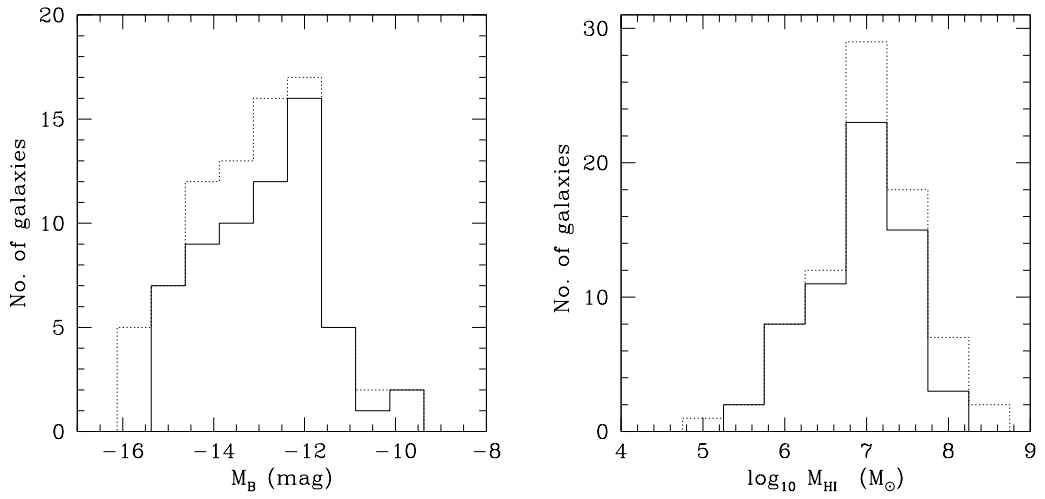

Figure 3.1: Distribution of absolute blue magnitude M_B (left panel) and M_{HI} (right panel). Because of problems with the high resolution images of some galaxies, we use only a subset of the total sample for the analysis in this chapter (See the text for more details). The dotted lines represent the entire FIGGS sample, whereas the solid lines are for the galaxies whose data are used in this chapter.

This leaves us with a total of 62 galaxies. Figure 3.1 shows the distribution of absolute blue magnitude and HI mass for our sample galaxies. For this sub-sample, the median HI mass is $\sim 1.4 \times 10^7 M_\odot$, the median blue magnitude is $M_B \sim -12.3$ mag, and the median distance is ~ 4.4 Mpc.

In Fig. 3.2 we show the integrated HI images of a representative sample galaxy, UGC 8833, which has an HI mass of $10^{7.2} M_\odot$ and an inclination $\sim 28^o$. Maps at three different resolutions, viz. $\sim 40''$, $12''$ and $4''$ are shown. As can be clearly seen, the low resolution images smooth over the high column density clumps that are seen at higher resolutions. Conversely, the smooth diffuse emission that is seen in the low resolution images is largely resolved out in the high resolution images. Clearly, for any individual galaxy one would need to use data from a range of resolutions to get an

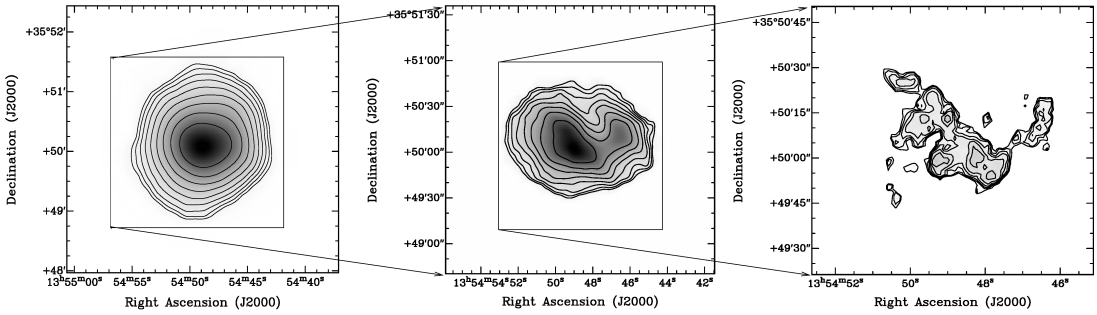

Figure 3.2: Integrated HI maps of UGC 8833 ($M_{HI} = 10^{7.2} M_{\odot}$) at three different resolutions, viz. $\sim 40''$ (left panel), $\sim 12''$ (middle panel) and $\sim 4''$ (right panel). In all three panels the contours spacing is $\sqrt{2}$. The first contour is at $6, 10$ & 30×10^{19} atoms cm^{-2}respectively for the left, middle and right panels.

accurate estimate of the HI column density distribution function. We return to this issue in the next section where we compute the HI column density distribution function for our sample of galaxies.

3.3 The Column Density Distribution Function

The HI column density distribution function $f(N_{HI})$ was first used in the context of gas seen in absorption against distant quasars. It is defined such that $f(N_{HI})dN_{HI}dX$ gives the number of systems with gas column density between N_{HI} and $N_{HI}+dN_{HI}$ that would be encountered within an absorption distance dX (Bahcall et al., 1969). The quantity $f(N_{HI})$ is directly computable from absorption spectra (see e.g. Noterdaeme et al., 2009; Prochaska and Wolfe, 2009; Wolfe et al., 1986) and is hence fairly well known at redshifts $\gtrsim 2$. At redshifts below ~ 2 the Lymanα line cannot be observed from ground based telescopes; $f(N_{HI})$ is consequently not well measured at these redshifts. At the lowest redshifts (i.e. $z \sim 0$) however, $f(N_{HI})$ can be computed from resolved images of the HI disks of galaxies and knowledge of the HI mass function (see e.g. Rao and Briggs, 1993; Zwaan et al., 2005). Specifically, from the integrated HI map of a galaxy one can compute the total area in the map that is covered by gas with column densities between N_{HI} and $N_{HI} + dN_{HI}$. This area is clearly dependent on the inclination of the galaxy to the line of sight; however if one has a large sample of galaxies with random inclinations to the line of sight, the average area $A(N_{HI}, M_{HI})$, provided by galaxies in

some HI mass bin would automatically represent the average over different inclinations. In order to compute the average area along a random line of sight through the universe, this average area has to be further normalised by the number density of galaxies with HI mass in the given mass bin, i.e. the HI mass function. Putting this all together, (and also using the fact that at $z = 0$, dX/dz = 1) $f(\mathrm{N_{HI}})$ can be computed as (see e.g. Zwaan et al., 2005).

$$f(\mathrm{N_{HI}})d\mathrm{N_{HI}} = \frac{\mathrm{c}}{\mathrm{H_0}} \int \psi(\mathrm{M_{HI}})\mathrm{A}(\mathrm{N_{HI}}, \mathrm{M_{HI}})\mathrm{dM_{HI}} \tag{3.1}$$

where

$$\psi(\mathrm{M_{HI}}) = \frac{\phi(\mathrm{M_{HI}})}{\ln(10.0)\mathrm{M_{HI}}} \tag{3.2}$$

and $\phi(\mathrm{M_{HI}})$ is the usual HI mass function (per unit interval of $\log_{10}(\mathrm{M_{HI}})$) which is generally parametrised as a Schecter function. Here we use the Schecter function parametrisation provided by (Martin et al., 2010) with $\alpha = -1.33, \phi_* = 4.8 \times 10^{-3}$ $\mathrm{Mpc^{-3}dex^{-1}}$, $\mathrm{M_{HI*}} = 10^{9.96}\mathrm{M_\odot}$. The integral in Eqn. (3.1) was computed by summing the integrand computed over logarithmic bins in $\mathrm{M_{HI}}$, the bin width was taken to be 0.3. We have confirmed that the result is not very sensitive to the chosen bin width, results obtained using bin widths of 0.2 and 0.4 overlap within the error bars. The slope of the faint end of the HI mass function remains somewhat uncertain. In the tabulation in (Martin et al., 2010) of various determinations of the HI mass function, the values reported for the faint end slope in different studies vary from -1.20 to -1.41. We conservatively take the error bars to be the quadrature sum of the variation in $f(\mathrm{N_{HI}})$ that one gets using these extreme values of the faint end slope and the errors obtained from bootstrap re-sampling over 100 runs.

Fig. 3.3 (left panel) shows $f(\mathrm{N_{HI}})$ computed from images at different resolutions. As discussed above, the $f(\mathrm{N_{HI}})$ computed from the low resolution images will underestimate the true $f(\mathrm{N_{HI}})$ at high column densities, while the $f(\mathrm{N_{HI}})$ computed from the high resolution images will underestimate $f(\mathrm{N_{HI}})$ at low column densities. This is clearly seen in Fig. 3.3 (left panel). We hence also use a "hybrid" $f(\mathrm{N_{HI}})$. For the hybrid $f(\mathrm{N_{HI}})$, the value at any $\mathrm{N_{HI}}$ is set to the maximum value obtained for different resolutions. We note that the hybrid curve differs from the curve made by using the low resolution $40''$data only at the highest column densities, viz. $\mathrm{N_{HI}} \gtrsim 10^{21.5}$atoms $\mathrm{cm^{-2}}$. (Zwaan et al., 2005) point out that a hybrid $f(\mathrm{N_{HI}})$ computed in this way will be an

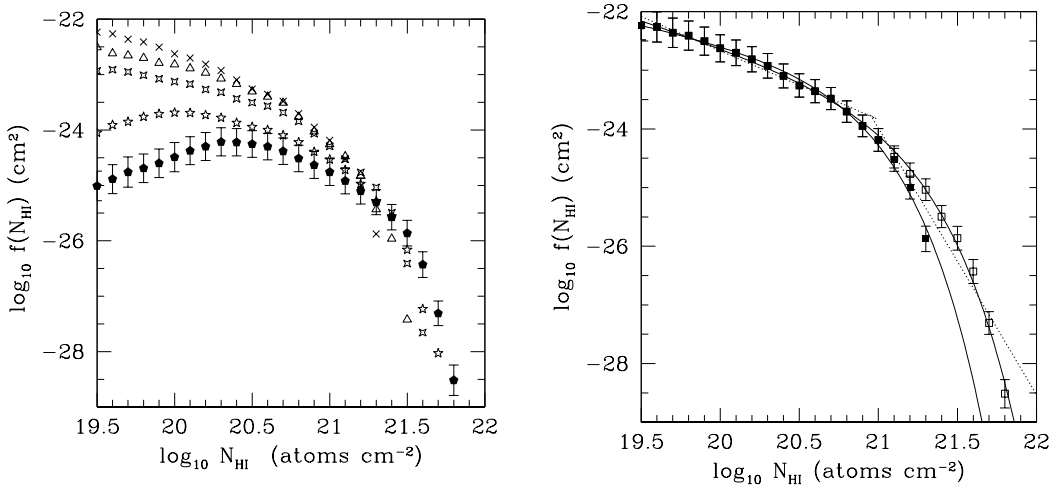

Figure 3.3: Left panel: The HI column density distribution function $f(\mathrm{N_{HI}})$ computed from images at different resolutions. The crosses use the $40''$ resolution data, the triangles are for the $25''$ resolution data, the hollow four pointed stars are for the $12''$ resolution data, the hollow five pointed stars are for the $6''$ resolution data and the filled pentagons are for the $4''$ resolution data. For clarity error bars are shown only for the $4''$ data (for which the error bars are largest). Right panel: The hybrid $f(\mathrm{N_{HI}})$ (hollow squares) and the $f(\mathrm{N_{HI}})$ derived from the $40''$ resolution data (filled squares). Gamma function fits (solid line) are shown for both sets of data. For both data sets, the break point for a piece wise linear fit is at $\log(\mathrm{N_{HI}}) \sim 21.0$, for clarity this is only shown for the hybrid curve (dotted lines).

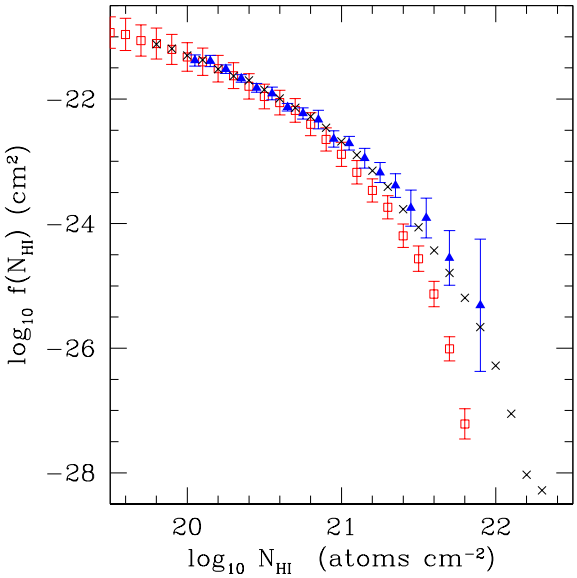

Figure 3.4: Comparison of the shape of $f(\mathrm{N_{HI}})$ computed from dwarf galaxies (hollow squares) with the $f(\mathrm{N_{HI}})$ for DLAs ((Noterdaeme et al., 2009), filled triangles) and for the $z = 0$ galaxy population ((Zwaan et al., 2005), crosses). As can be seen the $f(\mathrm{N_{HI}})$ for dwarfs falls sharply at high column densities as compared to the other two curves.

over-estimate, since the gas that is seen at high column densities in the high resolution images will also (after the smoothing that happens in the low resolution images) contribute to gas at lower column densities. In the rest of the chapter we hence give results obtained from both the hybrid $f(\mathrm{N_{HI}})$ and the $f(\mathrm{N_{HI}})$ computed from the $40''$ resolution images.

3.3.1 Results and Discussion

Fig. 3.3 (right panel) shows the hybrid $f(\mathrm{N_{HI}})$, as well as the $f(\mathrm{N_{HI}})$ derived from the $40''$ resolution data. To allow easy comparison with previous works, we also show two different fits, i.e. a broken power law, and a gamma function defined as:

Parameter	(Zwaan et al., 2005)	(Noterdaeme et al., 2009)	FIGGS (Hybrid)	FIGGS $40''$
$\log(\alpha)$	-22.91	-22.75	-23.29 $\pm$ 0.04	-22.79 $\pm$ 0.06
β	1.24	1.27	0.88 ± 0.04	0.57 ± 0.07
$\log N_*$	21.2	21.26	20.82 ± 0.01	20.55 ± 0.03

Table 3.1: Parameters of the Gamma function fit to $f(\mathrm{N_{HI}})$.

$$f\left(N_{HI}\right) = \alpha \left(\frac{N_{HI}}{N_*}\right)^{-\beta} e^{-(N_{HI}/N_*)}$$

Below we compare the $f(\mathrm{N_{HI}})$ computed here with those determined by (Zwaan et al., 2005) and (Noterdaeme et al., 2009). In the piece wise power law fit to the dwarf galaxy $f(\mathrm{N_{HI}})$ the break point which gives the best fit is at $\log(\mathrm{N_{HI}}) \cong 21.0$ for the hybrid $f(\mathrm{N_{HI}})$, and 20.9 for the $f(\mathrm{N_{HI}})$ derived from the $40''$ resolution data. As can be seen from Fig. 3.3 (right panel) $f(\mathrm{N_{HI}})$ is curved at high column densities and the gamma function provides a much better fit to the data than a broken power law. This curvature of the $f(\mathrm{N_{HI}})$ curve is very similar to what (Zwaan et al., 2005) found for their WHISP sample.

A particularly interesting result to come out of the earlier data sets is that the shape of the $f(\mathrm{N_{HI}})$ derived for the local galaxy population agrees well with that derived from DLAs (Prochaska and Wolfe, 2009; Zwaan et al., 2005). This is a surprising result for a number of reasons, viz. (i) the total neutral gas density evolves, changing by about a factor of 2 between high redshifts and $z \sim 0$ (Noterdaeme et al., 2009; Zwaan et al., 2003), (ii) the morphological mix of galaxies is significantly different at high redshifts (Conselice et al., 2005), and (iii) DLAs have significantly lower metallicity than low redshift spiral galaxies that dominate the HI cross section at $z = 0$. The non-evolution of $f(\mathrm{N_{HI}})$ has led to the suggestion that it is set by some universal process that shapes the gas distribution (Erkal et al., 2012). A possible explanation is geometric – for gas in a thin disk, averaging over different orientations would lead to an $f(\mathrm{N_{HI}})$ that falls as $\mathrm{N_{HI}^{-3}}$ at column densities larger than the maximum face on column density of the disk (Erkal et al., 2012; Milgrom, 1988).

3. THE HI COLUMN DENSITY DISTRIBUTION FUNCTION IN FAINT DWARF GALAXIES

In Fig. 3.4 we show the $f(\mathrm{N_{HI}})$ computed by (Zwaan et al., 2005), (Noterdaeme et al., 2009) and for the FIGGS sample. All the $f(\mathrm{N_{HI}})$ curves have been normalised to have the same value at $N_{HI} = 10^{20}$ atoms cm^{-2} so that one is comparing only the difference in shapes. As can be seen the dwarf galaxy $f(\mathrm{N_{HI}})$ differs markedly from the other two in that it falls much more steeply at the high column density end ($\mathrm{N_{HI}} \gtrsim 10^{21}$atoms cm^{-2}). The HI cross section at $z \sim 0$ is dominated by large galaxies (Zwaan et al., 2005), so the difference between the FIGGS $f(\mathrm{N_{HI}})$ and that determined by (Zwaan et al., 2005) is essentially the difference between large galaxies and dwarfs. It is interesting that the $f(\mathrm{N_{HI}})$ for dwarf galaxies begins to fall below the other two curves for column densities larger than $\log(\mathrm{N_{HI}}) \sim 21.0$ atoms cm^{-2}. For the $f(\mathrm{N_{HI}})$ derived from the THINGS sample (Erkal et al., 2012) also find a turnover at $\mathrm{N_{HI}} \sim 10^{21}$ atoms cm^{-2}. They attribute this feature to the HI cross section above this column density being dominated by highly inclined thin disks. The high column densities come from the long path lengths that the line of sight traverses through these disks. The sharp decline of the dwarf galaxy $f(\mathrm{N_{HI}})$ at high $\mathrm{N_{HI}}$ is presumably because in dwarfs the HI gas is not in a thin disk. (Roychowdhury et al., 2010) show that for the FIGGS sample, the median intrinsic axial ratio is ~ 0.6. A higher intrinsic axial ratio indicates a puffed up HI disk with a low average volume density of gas. Along with this a shorter scale length of HI disk dwarf galaxies prohibits the production of very high column densities in these galaxies even viewed at edge-on. In this context it is worth noting that the fall off at high $\mathrm{N_{HI}}$ is found in the dwarf $f(\mathrm{N_{HI}})$ despite the relatively high linear resolution of $\sim$ 100pc of our data (In contrast, the (Zwaan et al., 2005) sample was observed with a resolution $\sim$ 1.3kpc). In DLAs the drop in $f(\mathrm{N_{HI}})$ at $\mathrm{N_{HI}} \sim 10^{22}$atoms cm^{-2} is attributed to the onset of H_2 formation; above this column density, the gas transitions to being mostly molecular (see e.g Altay et al.). Since this transition happens at still higher column densities in low metallicity dwarfs (McKee and Krumholz, 2010; Welty et al., 2012), it cannot be the cause of the drop off that we see in the dwarf $f(\mathrm{N_{HI}})$. We note that the $f(\mathrm{N_{HI}})$ computed here as well as in (Zwaan et al., 2005) assumes that the emission is optically thin. (Braun, 2012) models the HI emission as arising from an isothermal gas distribution and finds that in this model optical depth corrections could lead to HI column densities as high as few times 10^{23} atoms cm^{-2}. This is in contrast to the current understanding that the gas becomes predominantly molecular at these column densities (e.g. Schaye, 2001). Our current data set does not

allow us to reliably estimate the opacity of the HI line. If optical depth corrections are indeed important, the comparison of the $f(\mathrm{N_{HI}})$ of dwarfs with DLAs may need some revision at the high column density end. However, the comparison of $f(\mathrm{N_{HI}})$ between the dwarf $f(\mathrm{N_{HI}})$ and the (Zwaan et al., 2005) results should remain largely unaffected, since both will have similar corrections. In the final stage of refereeing of this paper (Noterdaeme et al., 2012a) published the $f(\mathrm{N_{HI}})$ computed from DLAs in the SDSS III sample. Interestingly this $f(\mathrm{N_{HI}})$ agrees with the one determined by (Braun, 2012). Since the dwarf $f(\mathrm{N_{HI}})$ lies below the determination of the $f(\mathrm{N_{HI}})$ by (Zwaan et al., 2005), to bring the dwarf $f(\mathrm{N_{HI}})$ into agreement with (Noterdaeme et al., 2012a) would require a larger opacity related correction than has been applied to spiral galaxies. In the neutral atomic ISM, large opacities are expected to occur only in the cold neutral medium (CNM). In dwarf galaxies, the CNM fraction is in general lower than that in spiral galaxies (Warren et al., 2012; Young and Lo, 1997), so one would expect that opacity effects are less important in dwarfs than in spiral galaxies. It hence seems unlikely that the discrepancy between the dwarf $f(\mathrm{N_{HI}})$ and the spiral $f(\mathrm{N_{HI}})$ can be resolved by applying opacity corrections. Nonetheless, it will be very useful to try and estimate these corrections with the data sets obtained in the next generation surveys.

Fig. 3.5 shows the ratio $dn/dz(\mathrm{N_{HI}})$ as computed from the FIGGS data and from the (Zwaan et al., 2005) sample. $dn/dz(\mathrm{N_{HI}})$, is the integral over $\mathrm{dN_{HI}}$ of $f(\mathrm{N_{HI}})$, and gives the average number of absorbers with column density greater than $\mathrm{N_{HI}}$ per unit redshift. As can be seen, above the DLA column density limit ($\mathrm{N_{HI}} = 10^{20.3}$ atoms $\mathrm{cm^{-2}}$) dwarfs (with $\mathrm{M_{HI}} \lesssim 10^8 \mathrm{M_\odot}$) contribute about 10% to the cross-section. However the fraction drops rapidly with increasing $\mathrm{N_{HI}}$, and by $\mathrm{N_{HI}} \sim 10^{21.5}$atoms $\mathrm{cm^{-2}}$, dwarfs contribute less than 1% to the cross-section. In a model in which the host galaxies of DLAs were similar to the $z = 0$ dwarfs one could match the DLA number count (i.e. $dn/dz(N_{HI} = 10^{20.3})$) by scaling up the number density of dwarfs at high redshift. However, such a model would predict $\lesssim 3$ DLAs with $\mathrm{N_{HI}} > 10^{21.5}$atoms $\mathrm{cm^{-2}}$ in the SDSS volume, instead of the $\gtrsim 30$ found by (Noterdaeme et al., 2009). Further, DLAs with $\mathrm{N_{HI}} \sim 10^{22}$atoms $\mathrm{cm^{-2}}$ have been found in the SDSS survey (Kulkarni et al., 2012; Noterdaeme et al., 2009, 2012b). From the $f(\mathrm{N_{HI}})$ for DLAs, (Noterdaeme et al., 2009) estimate that only ~ 1 such high column density DLA should be detected in the SDSS survey volume. Since the $f(\mathrm{N_{HI}})$ for dwarfs falls sharply at high column densities, the probability of finding two such high column density absorbers in the SDSS volume is

vanishingly small for a host population dominated by dwarfs. Similarly high column densities are also seen in the DLAs arising from the host galaxies of high redshift GRBs (GRB-DLAs). Photometry of GRB hosts suggests that they are small galaxies (Chen et al., 2009), albeit somewhat brighter than the dwarfs considered here. Nonetheless, the sharp fall off in $f(\mathrm{N_{HI}})$ at high column densities for dwarfs strongly supports the suggestion (see e.g. Prochaska et al., 2007) that GRBs probe biased regions of the ISM, i.e. those with the highest column density. In the case of ordinary DLAs, as argued above, models where the host galaxies are all similar to $z = 0$ dwarfs appear to be ruled out. However models with a larger fraction of dwarfs but either (i) a sufficient number of disk galaxies to provide the observed cross section at high column densities, and/or (ii) where a signficant fraction of the high column density gas arises from merging dwarfs may still be consistent with both the observed DLA $f(\mathrm{N_{HI}})$ and the large velocity spreads observed in the DLAs low ionisation metal lines (see e.g. Prochaska and Wolfe, 1997).

To summarise, we determine the $f(\mathrm{N_{HI}})$ in faint local dwarfs, and find that it falls off significantly faster at high column densities than the $f(\mathrm{N_{HI}})$ in DLAs or in the $f(\mathrm{N_{HI}})$ determined from a representative sample of the local galaxy population. For the local galaxy population, at the high $\mathrm{N_{HI}}$ end the dominant contribution to $f(\mathrm{N_{HI}})$ comes from the disks of large spiral galaxies viewed edge on. Isolated galaxies like the $z = 0$ dwarfs hence cannot form the dominant host population of high redshift DLAs and GRB-DLAs unless there is significant biasing of the observed lines of sight and/or corrections for the opacity of the HI line is important even for dwarf galaxies. The FIGGS sample is one of the largest existing samples of faint dwarf galaxies with high resolution HI images. We hence expect that further significant progress on the shape of $f(\mathrm{N_{HI}})$ in dwarfs will require data from HI surveys using the next generation telescopes, i.e. the Australian SKA Pathfinder (ASKAP; Deboer et al. 2009), MeerKAT (Jonas, 2009) in South Africa and APERTIF (Verheijen et al., 2008) in the Netherlands.

Discussions with and comments from Nissim Kanekar as well as very useful comments from the anonymous referee are gratefully acknowledged.

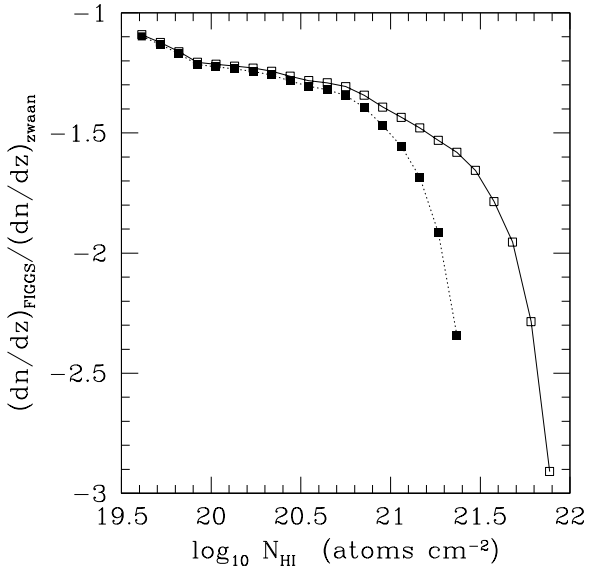

Figure 3.5: Ratio of $\frac{dn}{dz}$ computed from dwarf galaxies with that computed for the $z = 0$ galaxy population (Zwaan et al., 2005). The solid squares are for the $f(\mathrm{N_{HI}})$ derived from the $40''$ resolution data while the hollow squares are for the hybrid $f(\mathrm{N_{HI}})$.

3. THE HI COLUMN DENSITY DISTRIBUTION FUNCTION IN FAINT DWARF GALAXIES

4

Modeling HI distribution and kinematics in the edge-on dwarf irregular galaxy KK250

4.1 Introduction

The equilibrium vertical gas distribution in a galaxy is determined by the balance between the vertical pressure gradients and the net gravitational potential of the galaxy[1]. Measurements of the HI scale-heights of nearby edge-on disc galaxies hence allow one to infer the vertical gravitational field. Further, since the HI disc generally extends to galacto-centric radii where the gravity due to stars is negligible, both the flaring of the HI disc as well as its rotational velocity can be used as diagnostic probes of the underlying potential of the dark matter halo (see e.g. Banerjee and Jog, 2008; Banerjee et al., 2010, 2011a; Becquaert and Combes, 1997; Narayan et al., 2005; Olling, 1995). While modelling of the vertical distribution of the gas can be used to infer the properties of the dark matter distribution, comparison of models with observations is complicated by the following problem. The HI disc scale-height can be constrained from observations of edge on galaxies. In such a situation it is however difficult to measure the gas velocity dispersion σ_g, which is a critical parameter for the model. (Banerjee et al., 2011a) show that the uncertainty in σ_g is an important contributor to the uncertainty

[1]This chapter is based on "Modelling HI distribution and kinematics in the edge-on dwarf irregular galaxy KK250", Patra et al. MNRAS, 445, 1425, (2014).

in the scale-height computed from the model. The calculated HI scale-height is highly sensitive to the assumed value of σ_g; a 10% change in σ_g can lead to $\sim$ 15% change in the calculated HI scale-height. While σ_g can be measured for face on galaxies, in such cases it is diffuclt to directly measure the scale-height. The fact that it is difficult to simultaneously measure both the scale-height and the velocity dispersion makes it difficult to build completely data driven models of the vertical distribution of the HI . In this paper we use GMRT observations of the dwarf irregular galaxy KK250 to model the scale-height of the HI distribution. The dark matter halo is assumed to be spherically symmetric and its parameters are fixed from modelling of the observed rotation curve. Unlike the earlier studies, we do not assume a fixed value for the gas velocity dispersion, but instead allow it to be a free parameter in the fitting. We pick the model that best fits the observed vertical HI distribution. Although the observed velocity widths were not used as an input to the model, we also compare the observed line of sight profiles with the model ones, to check for consistency. The rest of this paper is arranged as follows. In §2, we present the HI data, in §3 the modelling procedure. §4 contains a comparison of the model with the observational data, and a discussion of the results.

4.2 HI observations and analysis

KK250 was observed as part of the Faint Irregular GMRT Galaxy Survey (FIGGS; Begum et al., 2008). Throughout this paper we assume a distance of 5.9 Mpc to the galaxy (Karachentsev et al., 2013). At this distance, an angular separation of $1^{'}$ corresponds to a linear separation of 1.7 kpc. The observations, data analysis as well as the rotation curve and mass decomposition for this galaxy are presented in (Begum and Chengalur, 2004). The galaxy is close to edge-on, meaning that a circular beam gives far fewer independent measurements along the minor axis than the major axis. In this paper we are interested in modeling the scale-height of the HI . We would hence like to have as good a resolution as possible along the minor axis. The hybrid configuration of the GMRT (Swarup et al., 1991) allows one to use a single GMRT observation to make images at a range of angular resolutions (varying from $\sim 40^{''}$ for data from the central square antennas alone to $\sim 2^{''}$ for data from the full array). However, the signal to noise ratio at the higher resolutions is generally modest. To get an optimum between

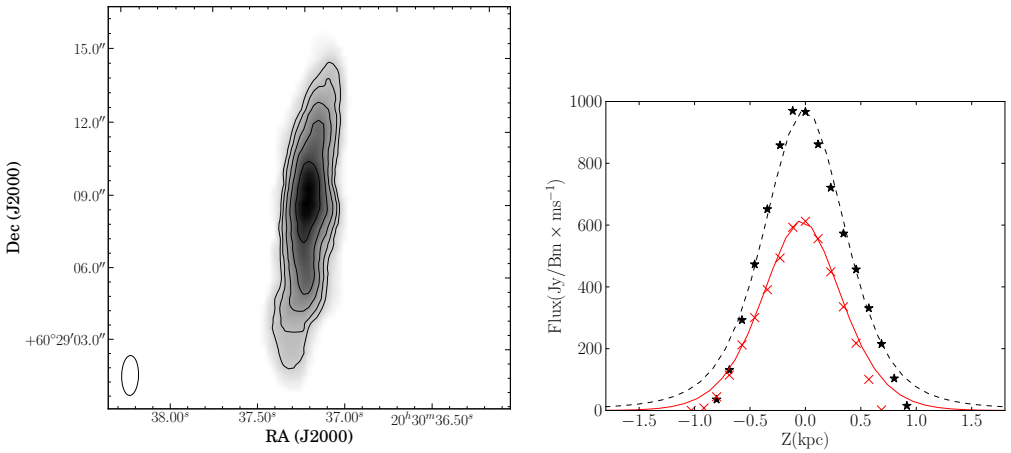

Figure 4.1: Left Panel GMRT HI 21 cm radio synthesis image of the dwarf irregular galaxy KK250. The image has been made using an elliptical beam with FWHM $32'' \times 13''$. The contour levels are $(1, 1.4, 2, 2.8, ...)\ 5 \times 10^{20}$ atoms cm^{-2}. See the text for more details. **Right Panel** This shows the intensity profiles along two vertical cuts through the disc of KK250. The stars are at a galacto-centric distance of 0.1 kpc, while the crosses are at a galacto-centric distance of -1.9 kpc. The dashed and solid lines are the corresponding model profiles at these two locations.

the angular resolution along the minor axis and the signal to noise ratio, we choose to image the galaxy with an elliptical beam, with the major axis of the ellipse aligned with the major axis of the galaxy. We used the task UVSRT in AIPS to rotate the visibility data so that the major and minor axis of the beam are aligned with the galaxy axes. The desired ellipticity of the beam can then be obtained using the UVTAPER parameters to the AIPS task IMAGR. For the analysis below, the images were made with a synthesized beam having full width half maximum (FWHM) of $32'' \times 13''$ (or 0.91 kpc $\times$ 0.37 kpc). The resulting image is shown in Fig. 4.1, along with the HI intensity profile at two different galacto-centric radii.

4.3 Modeling the galactic disc

4.3.1 Formulation of the Equations

Our model for the galaxy is based on similar modeling of edge-on galaxies done earlier by (Banerjee et al., 2011a; Narayan and Jog, 2002b). Details of the model can be found

in those papers, and is also briefly summarized below. The discs of the galaxy are modeled as a 2-component system of gravitationally-coupled stars and gas in the force field of a fixed dark matter halo. We assume that each of the two components is present in a form of a disc, the discs being concentric, and coplanar. We further assume the discs to be axi-symmetric and the halo to be spherically symmetric. The joint Poisson's equation for the disc plus dark matter halo in cylindrical polar coordinates (R, ϕ, z) therefore reduces to

$$\frac{1}{R}\frac{\partial}{\partial R}\left(R\frac{\partial \Phi_{total}}{\partial R}\right) + \frac{\partial^2 \Phi_{total}}{\partial z^2} = 4\pi G\left(\sum_{i=1}^{2}\rho_i + \rho_h\right) \tag{4.1}$$

where Φ_{total} is the total potential due to all the components and dark matter halo. ρ_i with $i = s, g$ denotes the mass density of stars and gas respectively. (Following (Begum and Chengalur, 2004) we correct the observed HI gas density by a factor of 1.4 to account for the presense of Helium.) ρ_h denotes the mass density of the dark matter halo. In their modeling of the rotation curve of this galaxy, (Begum and Chengalur, 2004) found that the dark matter halo is well fit by a pseudo-isothermal halo, and not well fit by an NFW (Navarro et al., 1997) type halo. We hence take the density distribution in the dark matter halo to be pseudo-isothermal, i.e. with a density profile given by

$$\rho_h(R, z) = \frac{\rho_0}{1 + \frac{R^2+z^2}{R_c^2}} \tag{4.2}$$

where ρ_0 and R_c are the central core density and core radius respectively (Binney et al., 2007).

The equation of hydrostatic equilibrium in the z direction for each of the two disc components, is given by

$$\frac{\partial}{\partial z}\left(\rho_i \langle\sigma_z^2\rangle_i\right) + \rho_i \frac{\partial \Phi_{total}}{\partial z} = 0 \tag{4.3}$$

where $\langle\sigma_z\rangle_i$ is the vertical velocity dispersion of the i^{th} component ($i = s, g$), again an input parameter .

Eliminating Φ_{total} between Equation (1) and (3) we get

$$\begin{aligned}\langle\sigma_z^2\rangle_i \frac{\partial}{\partial z}\left(\frac{1}{\rho_i}\frac{\partial \rho_i}{\partial z}\right) &= -4\pi G\left(\rho_s + \rho_g + \rho_h\right) \\ &+ \frac{1}{R}\frac{\partial}{\partial R}\left(R\frac{\partial \phi_{total}}{\partial R}\right)\end{aligned} \tag{4.4}$$

Equation (4) can be further simplified using the fact

$$\left(R\frac{\partial \phi_{total}}{\partial R}\right)_{R,z} = (v_{rot}^2)_{R,z} \tag{4.5}$$

Assuming that the vertical gradient in $(v_{rot})_{R,z}$ is small, we approximate $(v_{rot})_{R,z}$ by the observed rotation curve v_{rot}, which is a function of R alone. Thus Equation (4) reduces to

$$\begin{aligned}\langle\sigma_z^2\rangle_i \frac{\partial}{\partial z}\left(\frac{1}{\rho_i}\frac{\partial \rho_i}{\partial z}\right) &= -4\pi G\left(\rho_s + \rho_g + \rho_h\right) \\ &+ \frac{1}{R}\frac{\partial}{\partial R}\left(v_{rot}^2\right)\end{aligned} \tag{4.6}$$

Therefore Equation (6) now represents two coupled, second-order ordinary differential equations in the variables ρ_s and ρ_g. The solution of Equation (6) at a given R gives ρ_s and ρ_g as a function of z at that R. Thus solving Equation (6) at all R gives the model three dimensional density distribution of the stars and gas in the galaxy.

4.3.2 Input Parameters

As mentioned above, (Begum and Chengalur, 2004) present mass models for this galaxy, based on the HI rotation curve. We take the parameters from the mass model of (Begum and Chengalur, 2004) as inputs to the current model. Specifically, the stellar surface density $\sum_*(R)$ is taken to be an exponential with a scale-length $R_D \sim$ 1.1 kpc with the total stellar mass $3.4 \times 10^7 M_\odot$. The HI surface density $\sum_{HI}$ is modeled as a double Gaussian and given by

$$\Sigma_{HI} = \Sigma_{01} e^{-r^2/2r_{01}^2} + \Sigma_{02} e^{-r^2/2r_{02}^2} \tag{4.7}$$

with $r_{01} = 2.11 \pm 0.05$ kpc, $r_{02} = 0.41 \pm 0.02$ kpc, $\Sigma_{01} = 5.0 \pm 0.1\ M_\odot \mathrm{pc}^{-2}$ and $\Sigma_{02} = 4.2 \pm 0.2\ M_\odot \mathrm{pc}^{-2}$. As mentioned above, the HI surface density is scaled to account for the presense of helium to get the total gas density. The dark matter halo

is modelled as a pseudo-isothermal halo (Eqn. 2) with $\rho_0 = 37.6 \times 10^{-3}\ M_{\odot}\mathrm{pc}^{-3}$ and $R_c = 1.5$ kpc.

The remaining parameters that need to be specified are the vertical velocity dispersions in the stellar and gaseous discs. These cannot be directly measured from the data for edge-on galaxies. Banerjee & Jog (2011) show that while modelling the structure of the gaseous disc, the accuracy of the assumed value of stellar velocity dispersion $\sigma_{z,s}$ has a marginal effect on the calculated HI scale-height. We hence assume the stellar dispersion ($\sigma_{z,s}$) to be the same as obtained analytically for that of an isothermal stellar disc in vertical hydrostatic equilibrium in the net potential of the stars and the dark matter halo (Leroy et al., 2008). The assumed value of HI velocity dispersion, σ_g however strongly regulates the calculated HI scale-height (Banerjee et al., 2011a). Therefore using an accurate value of σ_g is fundamental to obtaining the correct value of the HI scale-height. Unlike earlier studies, we have not assumed an ad-hoc value for σ_g for our calculations. Instead, as described below, we have treated σ_g as a free parameter and constrained it using the observed data.

4.3.3 Solution of the Equations

We solve the two coupled, second-order ordinary differential equations given by Equation (6) in an iterative manner using a Eighth-Order Runge Kutta method as implemented in the scipy package.

$$(\rho_i)_{z=0} = \rho_{i,0} \quad \text{and} \quad \frac{d\rho_i}{dz} = 0 \tag{4.8}$$

The observations constrain the observed surface density Σ_i and not the midplane density $\rho_{i,0}$. We hence take a trial value of $\rho_{i,0}$, and iterate until the model matches the observed Σ_i. We are able to measure the HI vertical distribution only within a projected galacto-centric radius of 3 kpc, beyond that the signal to noise ratio is too poor to allow a realiable estimate to be made. Accordingly we solve Equation (6) for $0 < R < 3$ kpc at steps of 100 pc in the radial direction, and an adaptive (scale-height sensitive) resolution along the vertical axis. The resolution along the vertical direction was always better than 10 pc. The solution at the intermediate radii is estimated by interpolation. Since v_{rot} is fixed, Equation(6) can be solved independently for each value

of the radius R. Instead of assuming a fixed value of σ_g at each R, we treat it as a free parameter satisfying the following two constraints: (i) $1 < \sigma_g < 24$ km s^{-1}(ii) σ_g does not increase with R. The upper limit of ~ 24 km s^{-1}was set by increasing the upper limit to the range of σ_g being searched until we found a value that bracketed the best fit σ_g. We then explored the entire available parameter space in velocity dispersion using a grid with cell size in velocity of 2 km s^{-1}and radial cell size of 500 pc. In practice we generated a set of solutions for $\rho_i(R, z)$; each solution was for a fixed value of σ_g, with the σ_g being varied in steps of 2 km s^{-1}between the different solutions. Combinations of these solutions were then made for all possible σ_g profiles that satisfy the constraints listed above. Since, as noted earlier, Eqn(6) needs to be solved only as a function of z, combining the solutions is equivalent to solving the equation for each possible σ_g profile. From the $\rho_g(R, z)$ and the rotation curve we constructed a 3D model of the galaxy. This was then projected to the adopted morphological inclination ($i = 85^o$, see the discussion below), and convolved with the telescope beam to produce a model data cube.

(Begum and Chengalur, 2004) estimated the morphological inclination to be $i = 80^o \pm 4^o$. A value of 80^o for the inclination requires an extremely large velocity dispersion ($\sigma_g \sim 40$ km s^{-1}) at the centre to reproduce the observed morphology. In deriving the inclination, (Begum and Chengalur, 2004) assumed the intrinsic axial ratio to be $q_0 = 0.2$, however (Roychowdhury et al., 2013) show that dwarf galaxies tend to have somewhat larger intrinsic axial ratios. For galaxies with luminosity M_B between -12.6 and -14.8 the mean axial ratio is 0.36 with a scatter of ~ 0.15. A larger intrinsic axial ratio would lead to a higher value of the inclination. The inclination adopted here ($i = 85^o$) is consistent with this expectation. We note however that there is some uncertainty in deriving inclinations of dwarf galaxies, and our adopted value is in some sense a best guess.

Since the HI emission is optically thin, the integrated HI flux image has folded into it the distribution of all of the gas along the given line of sight. This means that for an edge on galaxy there is no one to one mapping between the observed thickness of the HI distribution at a given projected galacto-centric radius and the intrinsic HI scale-height. In order to compare the model distribution with the observations, we hence generate a model integrated flux image from the model data cube and measure the FWHM of the HI vertical distribution computed in exactly the same way as was

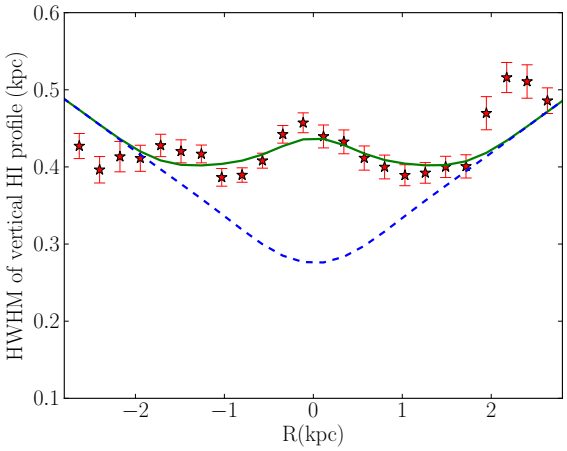

Figure 4.2: Plot of the obseved (points with error bars) half-width-at-half-maxima (HWHM) of the HI vertical intensity profile of the edge-on dwarf irregular galaxy KK250 as a function of galactocentric radius R overlaid with the best fit model (solid line), as well as a model in which the gas velocity dispersoion, σ_g is fixed at 8 km s^{-1}(blue dashed line).

done with the observed "moment 0" image. The σ profile that produced the best fit (smallest χ^2) fit to the observed data was picked as the best fit model. This is the most compute intesive step of the model fitting, and it was implemented using MPI based code and run on a 32 node IBM sandybridge cluster. A run using 400 processors takes about 8 hours. The best fit model had σ_g tending to a constant value of 8 km s^{-1}outside of $R \geq 1.5$ kpc, and rises steeply inside this. To resolve this better, a second set of models were produced, with σ_g set to 8 km s^{-1}outside $R = 1.5$ kpc, and with σ varying from $7 - 24$ km/s inside. The cells of fixed σ_g were reduced to 300 pc instead of the earlier value of 500 pc. The best fit of these models is then picked as our final model.

4.4 Results and Discussion

In Fig. 4.2, we compare the half-width-at-half-maximum (HWHM) of the observed vertical HI intensity distribution (points with error bars) with that from the best fit model (solid line). For comparison we also plot the HWHM profile for the constant $\sigma_g = 8$ km s^{-1}model (blue dashed line). As can be seen, the match between our model and the data is excellent inside a galacto-centric radius of 2 kpc. Between 2 kpc and 3 kpc the observed disc is slightly asymmetric. In this region one can see that the

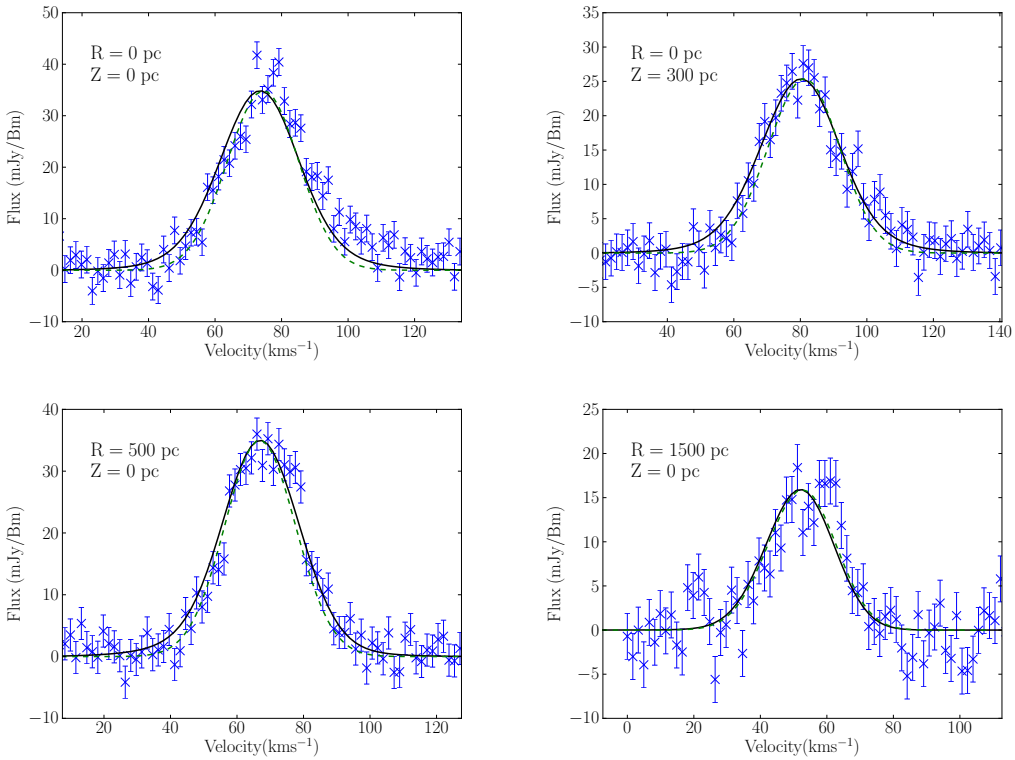

Figure 4.3: Observed versus model HI spectra at different locations in the galaxy. The solid and dotted lines show the best fit model and a model with a constant velocity dispersion of 8 km s^{-1}respectively. The model was fit only using the morphological data and not the kinematical data. Comparison of the model and observed spectra is hence an independent cross check of the model.

model represents some kind of average of the two halves. The model with constant $\sigma_g = 8$ km s^{-1}fails to produce the observed HWHM profile at the central region of the galaxy, though it merges with our model at $\sim R > 2$ kpc.

In Fig. 4.3 we compare the observed velocity profiles with the model profiles. Since the aim of this exercise is to see if the data provides some independent support for the existence of high velocity dispersion gas in the central regions of the galaxy, we have slightly shifted and scaled the model spectra so that they align exactly with the observed spectra. Recall that our model fitting used only the morphological data, this comparison provides an independent check. As can be seen from the figure, the velocity profiles in the central regions of the galaxy show an excess flux at $v \sim 100$ km s^{-1}as

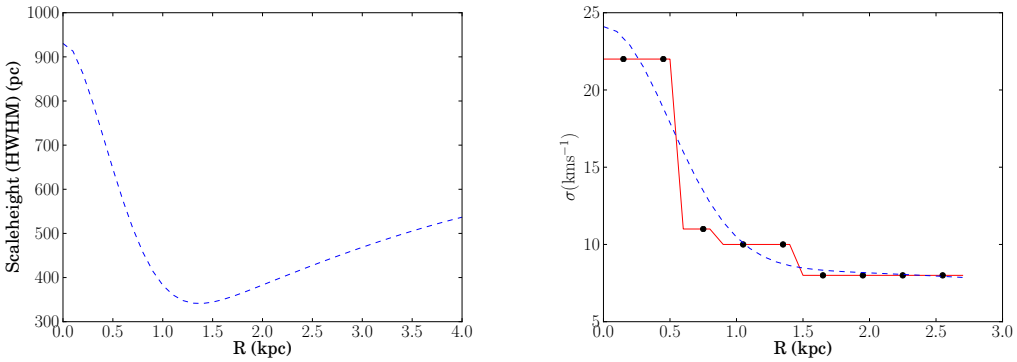

Figure 4.4: Left Panel: Plot of the calculated intrinsic scale-height (half-width-at-half-maxima) versus R corresponding to the Gaussian fits to the best-fit σ_g profile. **Right Panel:** Best-fit intrinsic HI velocity dispersion σ_g versus R overlaid with a double gaussian fit to the same. The velocity dispersion σ_g takes a value of $\sim$ 22 km s^{-1}at the galaxy centre and falls steeply with increasing galacto-centric radius R reaching to $\sim$ 8 km s^{-1}beyond R $\sim$ 1 kpc.

compared to the best fit model spectrum. This could perhaps be due to some low level non-circular motions which are not captured in our model. Several mechanism like feedback from star-formation, inflow or outflow of gas from the central region etc. could lead to this kind of non-circular motion. We also note in passing that the total amount of gas with high velocity dispersion is relatively small, and the existence of this gas is difficult to determine from the moment 2 maps that are often used as a measure of the velocity dispersion.

As discussed above, since the HI is optically thin, the observed vertical distribution of the HI reflects the scale-height distribution of all of the gas along the line of sight. If the scale-height does not vary with radius then the observed vertical distribution can be used to determine the intrinsic scale-height of the gas. If the scale-height varies with radius then determination of the true scale-height from the observed vertical distribution is not so straight forward. In the current case, since we have modelled the galaxy, we can use the model to determine how the scale-height varies with radius. In Fig. 4.4 (Left Panel), we plot the calculated model scale-height (defined as the HWHM of the model HI vertical density profile) versus R for the best-fit σ_g profile. As can be seen the HWHM varies significantly with galacto-centric radius. At $R \sim 0$,

the HWHM is $\sim$ 700 pc, it drops to a minimum value of $\sim$ 350 pc at $R = 1$ kpc. This is similar to both the scale-length of the stellar disc, as well as the spatial resolution of the data along the galaxy major axis. Beyond 1 kpc the gas disc flares by almost a factor of 2 by $R = 4$ kpc. HI flaring in the outer parts of galaxies is a common phenomenon and can be attributed to the decreasing importance of the self gravity of the disc components (see for example the study by Banerjee et al., 2011a). However the large HWHM seen in the central regions of the galaxy is unusual. To understand this better, it is useful to look at the radial variation of the velocity dispersion in our best fit model. In Fig. 4 (Right Panel), we plot our best-fit σ_g versus R along with a double-gaussian fit to the same. The velocity dispersion at the center of the galaxy is $\sim$ 22 km s^{-1}and it falls steeply to a value of 8 km s^{-1}by $R \sim 1$ kpc, which is equal to one exponential stellar disc scale-length R_D . The earlier studies (Banerjee et al., 2011a) of the scale-height in dwarf galaxies assumed a constant velocity dispersion of $\sigma_g = 8$ km s^{-1}. In Figure 4.2 we show the HWHM derived from a model in which we have assumed $\sigma_g = 8$ km s^{-1}. As can be seen, this provides a poor fit to the data in the central regions of the galaxy. Clearly the high velocity dispersion in the best fit model is driven by the fact that the observed HWHM is roughly constant towards the center of the galaxy, while the vertical gravitational force gets larger as one approaches the galaxy center. The decrease in velocity dispersion as one goes from the center to the edge of the disc in KK250 is also consistent with earlier results that in most galaxies the velocity dispersion either remains constant or decreases with radius (Tamburro et al., 2009). Our inferred value of σ_g of 22 km s^{-1}at the centre of galaxy is however somewhat high compared to the typical values obtained from other studies of dwarf galaxies. For e.g. (Johnson et al., 2012) find $\sigma_g \sim 10$ km s^{-1}for galaxies in the LITTLE THINGS survey and (Stilp et al., 2013) obtain values $\sim$ 6 - 12 km s^{-1}for the dwarf irregulars in the Local Group. We note however that apart from the center most region, the velocity dispersion in KK250 is similar to the values reported in these other works.

One of the input parameters to our model was the mass distribution as derived from the rotation curve by (Begum and Chengalur, 2004). In that paper the asymmetric drift correction (viz. the correction for the support against collapse provided by the pressure gradient in the gas) was derived by assuming the velocity dispersion to have a constant value of 8 km s^{-1}. Since the value we get near the centre of the galaxy is somewhat higher, we recalculated the asymmetric drift-corrected rotation curve using

the velocity dispersion as estimated here. The corrected curve lies within the error bars of the original rotation curve of (Begum and Chengalur, 2004), which justifies the use of the mass decomposition derived in that paper.

What is the origin of the velocity dispersion that we observe? The one dimension thermal velocity dispersion associated with 8000 K gas (i.e. a reasonable upper limit to the kinetic temperature of the Warm Neutral Medium) is $\sim$ 8 km s^{-1}. So while it is possible that the velocity dispersion that we see in the outer parts of the galaxy are entirely due to thermal motions of the particles, in central regions there must be an extra contribution due to small scale bulk motions of the gas. Velocity spreads in excess of thermal in the neutral ISM are often attributed to turbulence. In the case of dwarf galaxies, further evindence for the exisitence of turbulence in the atomic ISM comes from studies of the power spectrum of the HI intensity fluctuations (Begum et al., 2006; Block et al., 2010; Dutta and Bharadwaj, 2013; Dutta et al., 2009). Turbulence in the atomic gas in galaxies can arise from energy input from star formation and supernovae explosions (Mac Low and Klessen, 2004), magneto-rotational instabilities (MRI) in differentially rotating discs, (Sellwood and Balbus, 1999), gravitational instabilities (Wada et al., 2002) and mass accretion Klessen and Hennebelle (2010). KK250 has a linearly rising rotation curve, and hence the magneto-rotational instability does not appear to be relevant here. KK250 has a nearby companion dwarf galaxy, KK251, and tidal interaction could be a possible reason for the increased velocity dispersion. However, the HI distributions of KK250 and KK251 show no obvious sign of interaction or disturbance, and the rotation curves of the galaxies also appear fairly regular (Begum and Chengalur, 2004). It is hence appears that tidal interactions may not be playing an important role in this system. Which, if any, of the remaining mechanisms are responsible for driving turbulence in dwarf irregulars is currently unclear (see for e.g. Stilp et al., 2013).

Regardless of the origin of the velocity dispersion, the fact that the estimated velocity dispersion in dwarfs is comparable to that in much larger spiral galaxies will have consequences for the structures of the gaseous discs in dwarfs. The larger ratio of $\sigma_g/v_{\rm rot}$ in dwarfs will lead to their gas discs being thicker that those of spiral galaxies. Indeed, the typical HWHM for the HI that we determine for KK250 is significantly larger than the value of $\sim 70 - 140$pc determined for the inner disc of the Milky

way (Malhotra, 1995). Similarly large scale-heights for dwarf galaxies have also been indicated by studies of the power spectrum of the HI intensity fluctuations (Dutta et al., 2009). These results are based on the expectation that the slope of the power spectrum will change on scales comparable to the scale-height of the galaxy (Elmegreen et al., 2001). Finally, studies of the axial ratio distribution of the gas and stellar discs of dwarf galaxies (Roychowdhury et al., 2010, 2013) do indeed show that their stellar and gaseous discs are significantly thicker than those of spirals. The more diffuse gas distribution has several implications for galaxy evolution, including being likely to be one of the causes for the observed low efficiency of conversion of stars to gas in dwarf galaxies (Roychowdhury et al., 2009, 2011).

4.5 Conclusion

We use GMRT HI 21cm observations of the dwarf irregular galaxy KK250 to model the vertical distribution of the atomic gas. Our model consists of a 2-component galactic disc model of gravitationally-coupled stars and gas in the force field of a dark matter halo. The dark matter halo parameters are derived from fitting to the observed rotation curve. We allow the velocity dispersion of the gas to be a free parameter in the model, and constrain it using the observed half width half maximum of the vertical distribution of the HI . For the best fit model we also compare the observed line of sight velocity widths with the model ones, and find the two to be in good agreement. This provides a further consistency check to the derived velocity dispersion. From our best fit model, we find that the velocity dispersion is maximum at the center, but rapidly falls to a value of $\sim$ 8 km s^{-1}at $R \sim 1$ kpc. This is similar to both the scale-length of the stellar disc, as well as the spatial resolution along the radial direction. The intrinsic HI scale-height also reaches its minimum value at $R \sim 1$ kpc. The scale-height that we measure for KK250 is significantly larger than the scale-height of the HI in the central regions of the Milk way, consistent with earlier observations that dwarf galaxies have significantly thicker gas discs than typical spiral galaxies.

4. MODELING HI DISTRIBUTION AND KINEMATICS IN THE EDGE-ON DWARF IRREGULAR GALAXY KK250

5

Cold HI in faint dwarf galaxies

5.1 Introduction

The ISM in galaxies is multi-phase, consisting of molecular, atomic and ionised phases. Early observations of the HI 21cm emission/absorption spectra in our galaxy showed that the atomic gas itself has multiple phases (Clark, 1965; Radhakrishnan and Goss, 1972), a clumpy dense phase with low spin temperature and a more diffuse widely distributed phase with a high spin temperature. Theoretically it has been established that in steady state (i.e. when the heating rate is balanced by the cooling rate) the gas settles into one of two stable phases, a cold dense phase (the "Cold Neutral Medium" or CNM) and a warm diffuse phase (the "Warm Neutral Medium" or WNM) (Field and Saslaw, 1965; Field et al., 1969; Wolfire et al., 1995a, 2003). In these models, gas at kinetic temperatures intermediate between that of the stable CNM and WNM is subject to thermal instability and is expected to settle into one of the two stable phases. Gas in the CNM has small velocity dispersion and large 21cm optical depths, and is easily detected in absorption. The properties of the CNM in our galaxy are hence quite well established by emission/absorption studies. On the other hand the WNM has a very low optical depth, large velocity dispersion, is extremely challenging to detect in absorption, and its properties hence remain observationally not very established. Theoretical studies however indicate that the timescales for gas that has been disturbed away from the stable WNM conditions to settle into the WNM can be quite large. Sensitive emission absorption studies done over the last decade, aimed partly at detecting the WNM in absorption (e.g. Heiles and Troland, 2003b,c; Kanekar

et al., 2003; Roy et al., 2013a,c) have resulted in the somewhat surprising conclusion that a reasonable fraction of the atomic ISM in our galaxy could be out of thermal equilibrium, i.e. have kinetic temperatures that are intermediate between that of the CNM and WNM. Similarly numerical simulations of gas in a turbulent medium (e.g. Audit and Hennebelle, 2005) have also shown that in steady state a reasonable fraction of the gas could have kinetic temperatures in the unstable range.

In the case of nearby dwarf galaxies, most earlier studies of the phase structure of the gas have been done in the context of the classical two phase models and have focused on using the velocity dispersion to distinguish between the CNM and WNM. (Begum et al., 2006; Warren et al., 2012; Young and Lo, 1997; Young et al., 2003) analysed the spatially resolved line-of-site HI emission spectra of a number of nearby dwarf galaxies to look for narrow velocity dispersion gas. The narrow velocity dispersion gas was identified via multi-Gaussian fitting to the observed spectra. Components with small velocity dispersion were identified as arising from the CNM, whereas components with large velocity dispersion were identified with the WNM.

In our own galaxy, it has observationally been established that large optical depths (implying presence of the CNM) can be found along all lines of sight where the HI 21cm brightness temperature exceeds some threshold value (Braun and Walterbos, 1992; Roy et al., 2013a). This can be understood in terms of a maximum brightness temperature that the WNM can produce. As discussed in more detail below, because of its low optical depth, there is a limit on how large a brightness temperature one can get from physically reasonably sized path lengths through the WNM. The presence of high brightness temperature gas can hence be used to locate dense cold gas in external galaxies (e.g. Braun, 1997). Since the CNM is clumpy, this requires sensitive high spectral and velocity resolution observations. In this chapter we use these two different methods to detect cold HI in our sample of galaxies.

5.2 Sample & Data reduction

The sample of galaxies we use is drawn from the Faint Irregular Galaxy GMRT Survey (FIGGS) (Begum et al., 2008), and FIGGS2 survey (see chapter 2). These two samples contain a total of 73 galaxies detected in HI interferometric imaging. As described in more detail below, for detecting CNM the galaxies needed to be imaged at a specific

linear resolution. Out of the original sample of 73 galaxies, 11 galaxies could not be imaged at the required resolution, mainly because of signal to noise ratio related issues. The final sample hence consists of 62 galaxies. The median HI mass and median blue magnitude (M_B) of the sample are $10^{7.3} M_\odot$ and -12.7 respectively. Some general properties of the sample galaxies are listed in Tab. 5.1. The columns of the table contains: col(1): Name of the galaxy, col(2): RA of the galaxy in J2000 coordinate, col(3): DEC of the galaxy in J2000 coordinate, col(4): Distance to the galaxy in Mpc (taken from (Karachentsev et al., 2013)) col(5): Absolute blue magnitude (M_B) (again taken from (Karachentsev et al., 2013)) col(6): Log of HI mass of the galaxy, column(7) represents if the galaxy is included in the sample used for detecting the CNM via the Gaussian Decomposition method (see 5.3), column(8) represents if the galaxy is included in the sample for detecting the CNM via the Brightness Temperature method (see 5.4), col(9) presents the velocity resolution used to image the galaxy at $\sim$ 100 pc (as required for the T_B method).

As discussed above we use two different methods to try and identify gas in the CNM phase, viz. the Gaussian Decomposition method and Brightness Temperature (T_B) method. As shown in Sec. 5.3, the Gaussian Decomposition method requires spectra with high signal to noise ratio. For this we use data cubes at a uniform linear resolution of $\sim$ 400pc. Data cubes at higher linear resolutions have a signal to noise ratio that is too low for the Gaussian decomposition method to work reliably. On the other hand, as discussed in Sec. 5.4, the brightness temperature method is well suited to high resolution data cubes, and does not require as high signal to noise ratio spectra. We hence use data cubes made at $\sim$ $100pc$ linear resolution for finding cold gas using the T_B method. Some galaxies from the parent sample did not have sufficient signal to noise ratio (SNR) in the low resolution $\sim$ 400pc data cubes, while some galaxies did not have sufficient snr in the $\sim$ 100pc data cubes. These galaxies were hence dropped from the sub-sample used for that particular method. Details of the actual galaxies that were used for each method are also given in Tab. 5.1.

Table 5.1: General properties of our sample galaxies.

Name	RA (J2000)	DEC (J2000)	Dist (Mpc)	M_B (mag)	$\log M_{HI}$ ($M_\odot$)	Gaussian	T_B	Δv (T_B) (km s^{-1})

AGC112521	014107.9	+271926	6.58	−11.6	6.82	*N*	*N*	–
BTS146	124002.1	+380002	8.50	−12.2	6.97	*N*	*N*	–
LVJ1243+4127	124355.7	+412725	6.09	−11.8	7.02	*N*	*N*	–
DDO125	122741.8	+432938	2.74	−14.3	7.48	*N*	*Y*	1.7
DDO167	131322.8	+461911	4.19	−12.7	7.19	*N*	*N*	–
DDO181	133953.8	+404421	3.01	−13.2	7.33	*N*	*N*	–
DDO183	135051.1	+380116	3.22	−13.2	7.31	*N*	*Y*	1.7
DDO187	141556.5	+230319	2.20	−12.4	7.06	*N*	*Y*	3.3
DDO210	204651.8	−125053	0.94	−11.1	6.42	*N*	*Y*	1.6
DDO226	004303.8	−221501	4.92	−13.6	7.53	*Y*	*N*	–
DDO043	072817.2	+404613	5.73	−13.9	7.85	*N*	*N*	–
DDO006	004949.3	−210058	3.34	−12.4	7.04	*N*	*Y*	3.3
DDO099	115053.0	+385250	2.64	−13.5	7.74	*N*	*Y*	3.3
ESO321-014	121349.6	−381353	3.18	−12.7	7.21	*N*	*N*	–
ESO379-007	115443.0	−333329	5.22	−12.3	7.51	*Y*	*Y*	1.7
UGCA365	133630.8	−291411	5.25	−13.3	7.26	*N*	*N*	–
ESO490-017	063756.6	−255959	4.23	−14.5	7.55	*N*	*N*	–
GR8	125840.4	+141303	2.13	−12.0	6.89	*N*	*Y*	1.7
IC4316	134018.1	−285340	4.41	−13.9	7.05	*N*	*N*	–
KDG073	105257.1	+693245	3.70	−10.8	6.51	*N*	*N*	–
KK109	114711.2	+434019	4.51	−10.3	6.54	*N*	*N*	–
KK14	014442.7	+271716	7.20	−12.1	7.56	*N*	*N*	–
KK141	122252.7	+334943	7.78	−12.9	7.20	*N*	*N*	–
KK144	122527.9	+282857	6.15	−12.5	7.86	*Y*	*N*	–
KK15	014641.6	+264805	9.04	−11.9	7.24	*N*	*N*	–
KK152	123324.9	+332105	6.90	−13.0	7.54	*N*	*N*	–
KK160	124357.4	+433941	4.31	−10.9	6.59	*N*	*N*	–
KK195	132108.2	−313147	5.22	−11.8	7.56	*N*	*N*	–
KK200	132436.0	−305820	4.63	−12.0	6.84	*Y*	*Y*	1.7
KK246	200357.4	−314054	7.83	−13.7	8.07	*N*	*N*	–
KK65	074231.2	+163340	8.02	−14.3	7.70	*N*	*N*	–
KK69	085250.7	+334752	7.70	−12.2	7.51	*N*	*N*	–
KKH11	022435.0	+560042	3.00	−13.3	7.66	*Y*	*Y*	1.7
KKH12	022727.0	+572916	3.00	−13.0	7.23	*Y*	*Y*	1.6
KKH34	055941.2	+732539	4.61	−12.3	6.76	*N*	*Y*	3.3
KKH37	064745.8	+800726	3.39	−11.6	6.70	*N*	*N*	–
KKH46	090836.6	+051732	5.60	−11.9	7.28	*N*	*N*	–
KKH6	013451.6	+520530	3.73	−12.4	6.63	*Y*	*Y*	3.3
KKH86	135433.6	+041435	2.59	−10.3	5.91	*N*	*N*	–
KKH98	234534.0	+384304	2.45	−10.8	6.45	*N*	*Y*	3.3
LeG06	103955.7	+135428	10.40	−11.9	6.85	*N*	*N*	–
PGC051659	142803.7	−461806	3.58	−13.1	7.78	*Y*	*Y*	1.7
UGC03755	071351.8	+103119	7.41	−15.7	8.25	*N*	*N*	–

UGC04115	075701.8	+142327	7.73	−14.3	8.34	*Y*	*N*	–
UGC04879	091602.2	+525024	1.36	−11.9	5.98	*N*	*N*	–
UGC05186	094259.8	+331552	8.30	−13.4	7.38	*N*	*N*	–
UGC05209	094504.2	+321418	6.56	−13.1	7.15	*N*	*Y*	3.3
UGC05456	100719.7	+102144	5.60	−15.1	7.71	*Y*	*N*	–
UGC06145	110535.0	−015149	10.70	−13.9	7.97	*N*	*N*	–
UGC06456	112800.6	+785929	4.35	−14.1	7.77	*N*	*Y*	1.6
UGC06541	113329.1	+491417	3.89	−13.6	6.97	*N*	*Y*	3.3
UGC00685	010722.3	+164102	4.51	−14.3	7.74	*Y*	*Y*	6.6
UGC07298	121628.6	+521338	4.21	−12.3	7.28	*Y*	*Y*	1.7
IC3308	122517.9	+264253	12.80	−15.5	8.57	*N*	*N*	–
UGC07605	122839.0	+354305	4.43	−13.5	7.32	*Y*	*Y*	3.3
UGC08055	125604.00	+034841	17.4	−15.49	8.89	*N*	*N*	–
UGC08215	130803.6	+464941	4.55	−12.3	7.27	*Y*	*Y*	3.3
UGC08508	133044.4	+545436	2.69	−13.1	7.30	*N*	*Y*	1.7
UGC08638	133919.4	+244633	4.27	−13.7	7.08	*Y*	*N*	–
UGC08833	135448.7	+355015	3.08	−12.2	7.00	*N*	*Y*	1.7
UGCA292	123840.0	+324600	3.61	−11.8	7.44	*N*	*Y*	1.7
VCC0381	121954.1	+063957	4.71	−11.7	7.14	*N*	*N*	–

5.3 Searching for the CNM using Gaussian decomposition

As discussed above, classical models for the phase structure of the atomic ISM in the Milky Way and nearby galaxies indicate the existence of two stable phases with kinetic temperatures $\sim 5000 - 8000$ K, i.e. the "Warm Neutral Medium" (WNM) and $\sim 50 - 300$ K, i.e. the "Cold Neutral Medium" (CNM) respectively (Wolfire et al., 1995b). Recent observations and models suggest that in addition, there could be a significant amount of gas with kinetic temperatures that lie between $500 - 5000$ K, i.e. in the range that is thermally unstable (see e.g. Heiles and Troland, 2003a; Kanekar and Chengalur, 2003; Kim et al., 2014; Roy et al., 2013b). We follow (Chengalur et al., 2013) in calling this the "Unstable Neutral Medium" (UNM). In the Gaussian decomposition method, one decomposes the line of sight velocity profile into multiple Gaussians, and identifies components with velocity widths corrresponding to kinetic temperatures in the CNM range as the cold neutral medium. Gas at a kinetic temperature of 200 K would have a one dimensional thermal velocity dispersion of ~ 1.28 km s^{-1} or a FWHM of ~ 3.1 km s^{-1}. However, most previous studies of the CNM in dwarf galaxies (see

e.g. de Blok and Walter, 2006; Warren et al., 2012; Young and Lo, 1997) have used significantly larger velocity dispersions (up to ~ 6 km s^{-1}) to identify CNM gas. We note that a velocity dispersion of ~ 6 km s^{-1} corresponds to kinetic temperatures of ~ 4400 K. While this kinetic temperature is significantly higher than the maximum expected for the CNM, it is nonetheless lower than the expected kinetic temperature for the WNM. In the absense of non thermal contributions to the velocity width, gas with velocity dispersion $\lesssim 6$ km s^{-1} would correspond to gas in phases other than the WNM, i.e. the CNM or UNM. In the presnse of non-thermal motions however, the situation is more complex. The simplest case is if one assumes that the gas is isothermal and that the only non-thermal motions are micro-turbulence and that the net effect of these motions is to keep the profile shape as a Gaussian, albeit with a larger velocity width than that corresponding to the kinetic temperature. In this case, the velocity width of the profile provides an upper limit to the kinetic temperature, and gas with velocity dispersion of ~ 6 km s^{-1} must be at a kinetic temperature lower than that corresponding to the WNM. However if the gas has a range of kinetic temperatures, or if because of bulk motions the line profile is intrinsically non-Gaussian, then it is not clear what the components derived from a Gaussian decomposition physcially correspond to. In this section, we follow earlier studies (i.e. those cited above, as well as galactic studies such as (Heiles and Troland, 2003a; Shuter and Verschuur, 1964)) in assuming that the velocity width obtained from Gaussian decomposition can be used as a proxy for the kinetic temperature, but we return to the issues raised above in Sec. 5.4.

5.3.1 Implementation

Line-of-sight HI spectra were extracted from the 400 pc image cubes and decomposed into multiple Gaussian components using a python routine '`multigauss`' that was developed by us for this purpose. '`multigauss`' uses a non-linear optimization routine as implemented using the '`lmfit`' package of python.

Starting with a single Gaussian component, Gaussian components were successively added to the model till there is no improvement in the fit residuals as interpreted by a single-tailed F-test. This is similar to the procedure followed earlier by Warren et al. (2012). A single-tailed F-test estimates the probability (or confidence level) that two fit residuals are different just by random chance. Two residuals, one with N components and another with N+1 components were compared by single-tailed F test

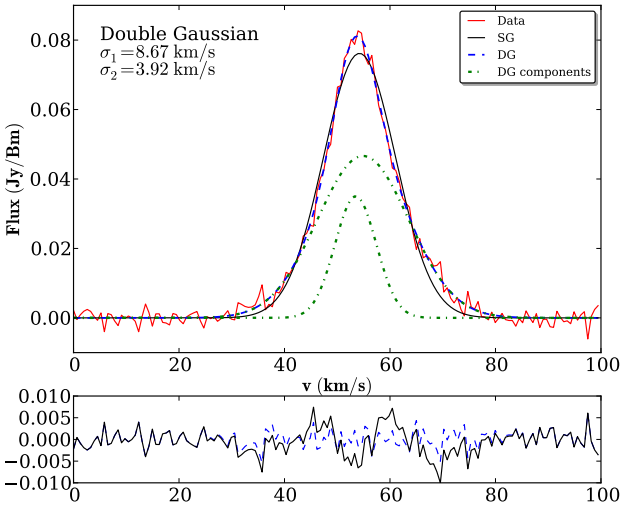

Figure 5.1: Example fits at SNR=20. The (simulated) input data (red solid noisy line), a single Gausian fit (black solid smooth line), double Gausian fit (blue dashed line) as well as the inidividual components of the double Gaussian fit (dotted lines) are shown. The residuals after subtracting the fits from the data are also shown (dashed line residual from the double Gaussian fit, solid line residual from the single Gausian fit). The routine detects a double gaussian fit as the best fit. The velocity dispersions for the double Gaussian fit are $\sigma_1 = 8.67$ km s^{-1}and $\sigma_2 = 3.92$ km s^{-1}, which match the true input values (8 km s^{-1}and 4 km s^{-1}) very well.

and the question asked is: what is the confidence level with which one can reject the hypothesis that the residual of fit with N+1 components is better than the residual of fit with N components purely by chance. This confidence level is referred as F-test confidence level of rejecting the null hypothesis. Narrow components returned by the routine were accepted as representing cold gas if the following critea are met. (1) The component must have a velocity dispersion $\sigma \lesssim 6$ km s^{-1}, (2) the amplitude of the narrow component must be at least 3 times the per channel rms noise, and (3) the velocity dispersion of the component must be greater than the velocity resolution of the data by at least the standard error returned by the fitting routine. Conditions (2) and (3) are meant to reduce the possibility of falsely identifying a narrow noise spike as a genuine narrow component. There was no restriction placed on the central velocity of the components. These criteria are very similar to those used in past studies, e.g. (de Blok and Walter, 2006; Warren et al., 2012; Young and Lo, 1997). One important difference between the current routine and those used in previous studies is that previous studies limited the maximum number of Gaussian components per spectrum to 2, where as in the current decomposition the total number of components to be fit has been left as a free parameter. All of our spectra are however well described by single or double Gaussian, with no spectra having more than two components in the best fit model.

5.3.1.1 Characterization of the routine

To characterize the detection efficiency of our routine `multigauss`, 50,000 model spectra were simulated having global SNR distributed uniformly between $10 < \mathrm{SNR} < 60$. Each spectrum consisted of a narrow component with $\Delta v < \sigma < 6.0$ km s^{-1}, (where Δv is set 1.65 km s^{-1}, i.e. corresponding to the velocity resolution of the observed data) and a broad component with $8.0 < \sigma < 12.0$ km s^{-1}. Each of the components was required to have a SNR (i.e. peak amplitude) more than 3. Adopting a conservative approach, the centroids of two components were set to be the same, as any offset between these two would lead to a higher detection efficiency. As mentioned above, no spectra required more than two components for the best fit, the simulated spectra were hence restricted not to have more than two components. These synthetic spectra then passed through the `multigauss` routine. In Figure 5.2 (left panel), we plot the recovery efficiency of

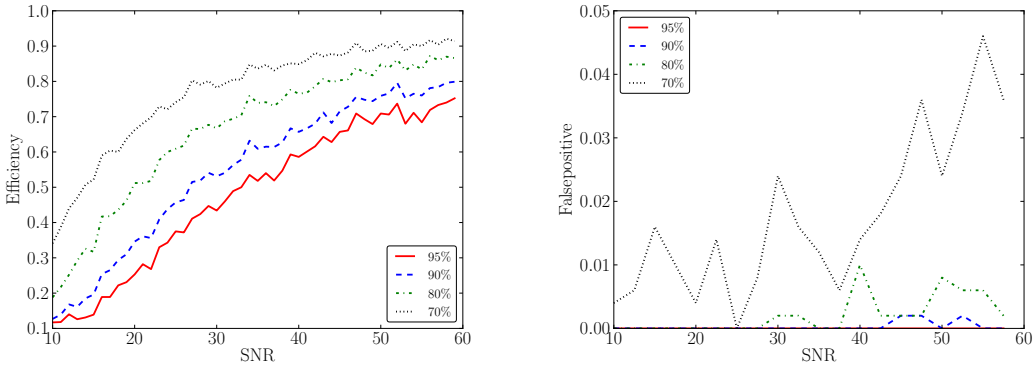

Figure 5.2: Left panel: The recovery efficiency of our routine as a function of the signal to noise ratio (SNR) at different F-test confidence levels. Right panel: False detection rate of our routine as a function of the SNR at different F-test confidence limits.

our routine as a function of SNR. Different curves represent different confidence levels of F-test.

To characterize the false detection rate of our routine, we simulated 1000 spectra with only one component with velocity dispersion uniformly distributed between $8.0 < \sigma < 12.0$ km s^{-1}, added gaussian random noise, and then passed them through `multigauss`. The false positive rate measured in this way is shown in the right panel of Fig. 5.2. We note that the false positive rate is always less than a few percent for SNR in this range (i.e. > 10). This is similar to the results found in previous studies (e.g. Warren et al., 2012). The detection efficiency and detection accuracy are summarized in Table 5.2. The columns in the table are as follows: Col. (1) the confidence level of the F-test. Col. (2) the amplitude ratio of the input and recovered narrow component. Col. (3) the mean offset between the centroids of the input and recovered narrow component. Col. (4) The average of the absolute value of the difference between input and the recovered velocity dispersion of the narrow component.

For the rest of the analysis below we adopt a conservative F-test confidence level, which we set to 95%. At this confidence level, the detection rate is comparatively small, but the false positive rate is negligible. Further, in the cases where a narrow component is recovered, the parameters of this Gaussian are also fairly accurately recovered. Using this conservative approach implies that the number of identified narrow components is

Table 5.2: Characterization of the efficiency and the accuracy of the decomposition routine

Confidence level	A_{sim}/A_{extr}	Δb (km/s)	$\Delta\sigma$ (km/s)
95%	0.97 ± 0.17	0.00 ± 0.26	-0.12 ± 0.57
90%	0.98 ± 0.21	0.00 ± 0.35	-0.07 ± 0.57
80%	0.99 ± 0.29	-0.01 ± 0.58	0.00 ± 0.60
70%	1.02 ± 0.36	0.00 ± 0.74	-0.06 ± 0.69

a lower limit to the true number of such components. Once again the approach adopted here is similar to that taken in earlier studies (e.g. Warren et al., 2012), to allow an easy comparison of our results with those from earlier work.

5.3.2 Results

We had data for a total of 62 galaxies in the main sample. For galaxies with high inclinations, the observed spectrum is a blend of the emission from gas distributed along a relatively long line of sight. We hence exclude galaxies with inclination more than 70^o from the sample. As discussed above we also require a peak SNR of > 10, and galaxies for which the data cube contained no spectra with SNR greater than this threshold were also dropped from the sample. After these cuts, we are left with a total of 15 galaxies.

The data for these 15 galaxies were passed through the `multigauss` routine, which detected narrow components in 8 of them. In Table 5.3 we summarise the inputs and the results of Gaussian decomposition method. The columns are as follows: Col. (1) Name of the galaxy, Col. (2) The log of HI mass of the galaxy, Col. (3) The absolute blue magnitude of the galaxy, Col. (4) The number of lines-of-sight which met the SNR criteria (i.e. SNR >10), Col. (5) Column density at SNR = 10, Col. (6) the average SNR of the spectra with SNR greater than the threshold, Col. (7) shows the average column density of the lines-of-sight having SNR greater than 10. Col. (8) The peak column density in the galaxy, and Col. (9) The amount of narrow velocity dispersion HI detected.

Figure 5.3 shows the narrow velocity dispersion HI detected in the galaxy UGC 685. The dashed line contours show the integrated HI emission, while the Hα emission is

Table 5.3: Summary of cold HI search using Gaussian decomposition method

Name	log M_{HI} ($M_\odot$)	M_B	N	CD_{10} (atoms cm^{-2})	<SNR>	<CD> (atoms cm^{-2})	CD_{peak} (atoms cm^{-2})	log Cold M_{HI} ($M_\odot$)
DDO226	7.53	-13.60	2	1.07e+20	10.07	1.08e+20	1.08e+20	–
ESO379-007	7.51	12.30;	11	1.09e+20	10.74	1.16e+20	1.23e+20	–
KK144	7.86	-12.50	3	2.97e+20	10.48	3.12e+20	3.17e+20	4.90
KK200	6.84	-12.00	3	1.42e+20	10.37	1.47e+20	1.50e+20	4.05
KKH11	7.66	13.30;	716	6.01e+19	12.65	7.22e+19	1.15e+20	5.79
KKH12	7.23	13.00;	82	3.36e+19	11.51	3.72e+19	4.48e+19	4.47
KKH6	6.63	12.40;	19	9.63e+19	10.81	1.04e+20	1.11e+20	–
PGC051659	7.78	13.10;	331	1.15e+20	12.09	1.33e+20	1.88e+20	5.99
UGC04115	8.34	-14.30	8	1.87e+20	10.18	1.90e+20	1.95e+20	–
UGC05456	7.71	-15.10	27	1.29e+20	10.58	1.37e+20	1.45e+20	–
UGC00685	7.74	-14.30	220	1.53e+20	11.81	1.72e+20	2.23e+20	5.94
UGC07298	7.28	-12.30	1	1.04e+20	10.01	1.04e+20	1.04e+20	–
UGC07605	7.32	-13.50	105	1.18e+20	12.03	1.36e+20	1.81e+20	4.22
UGC08215	7.27	-12.30	13	1.40e+20	10.56	1.47e+20	1.56e+20	5.28
UGC08638	7.08	-13.70	16	1.34e+20	10.30	1.38e+20	1.42e+20	–

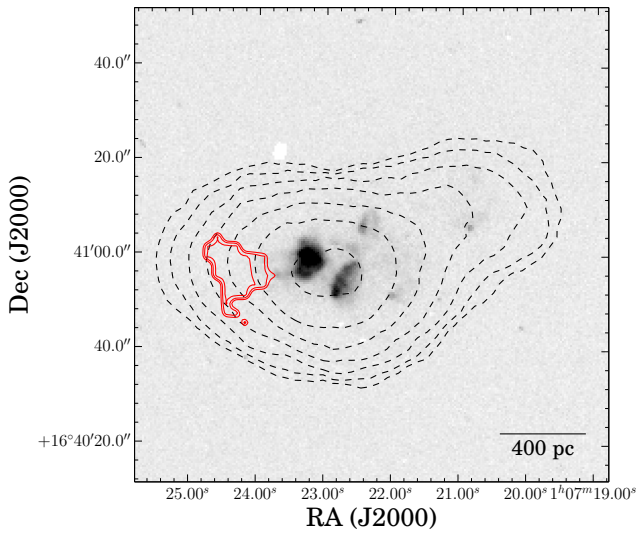

Figure 5.3: Gray scale represents the Hα map of U685. Black broken contours represents total HI column density and the levels are $(1, 1.4, 2, 2.8, 4, 5.6, 8, 11.2, 16, 22.4, ...)$ 5×10^{20} atoms cm^{-2}. Red solid contours show the cold HI as recovered by Gaussian method. The levels are $(1, 1.4, 2, 2.8, 4, 5.6, 8, 11.2, 16, 22.4, ...)$ 6.2×10^{20} atoms cm^{-2}. The spatial resolution of all the gray-scale and contours is $\sim$ 400 pc.

shown in grey-scales. The regions where narrow velocity dispersion HI were detected is delineated by solid lines. To compare our result with previous work of (Warren et al., 2012) we used the publicly available data from LITTLE-THINGS (Hunter et al., 2012) survey and passed through our routine. The narrow velocity dispersion detected by our routine matches well with the published results by (Warren et al., 2012). We also note that cold HI recovered in the GMRT data also match with the published LITTLE-THINGS (Warren et al., 2012) results despite being observed by different telescope with different velocity resolution.

We note that the narrow velocity dispersion HI as detected by the Gaussian decomposition method doesn't coincide with the highest column density regions or with the Hα emission. The Hα emission originates mainly from regions with recent (i.e. $3 - 10$ Myr) star-formation. For all of our sample galaxies, the narrow velocity dispersion HI is offset from the regions of current star formation. If the CNM is associated with the molecular gas from in which the star formation occurs, one would expect that there would be a good correlation between the detected CNM and the Hα emission. We note that previous studies (Warren et al., 2012; Young and Lo, 1996) also observed similar offset between the gas with small velocity dispersion and the regions of current star formation. One possible explanation is that in this context, the Gaussian Decomposition method is not best suited for identifying the CNM in dwarf galaxies. We explore this possibility, as well as other techniques to identify the CNM in the rest of this chapter.

5.3.3 Drawbacks of Gaussian decomposition method

As described above we used (following the lead of earlier searches for the CNM in nearby dwarf galaxies) Gaussian decomposition to identify narrow velocity dispersion gas. This method has several drawbacks. The first is that, as is well known, Gaussians do not form a orthogonal basis set. Thus any Gaussian decomposition suffers from the problem of not being unique. Further as mentioned above, it is not clear that the components recovered from a given decomposition correspond to separate physical entities. Finally the shapes of the line profiles obtained using observations with finite spatial resolution (as well as integration along the line of sight) are determined by a number of physical processes, including turbulent motions and bulk velocities in addition to the thermal

velocity dispersion. In view of these drawbacks, we examine in the next section, an alternate method for identifying cold atomic gas in dwarf galaxies.

5.4 The Brightness temperature method

The observed brightness temperature of HI 21cm emission (defined as $T_B = \frac{I_\nu c^2}{2k\nu^2}$ where T_B is the brightness temperature in Kelvin, 'I_ν' is the specific intensity, 'k' is Plank's constant and 'c' is the speed of light), has long been used to constrain the physical conditions in the atomic ISM (e.g. Baker and Burton, 1975; Braun and Walterbos, 1992; Rohlfs, 1971; Schmidt, 1957). In detail, the observed brightness temperature depends on the distribution of the spin temperature, optical depth as well as spatial ordering of all the gas along the line of sight. In the context of multi-phase models however, the presense of high brightness temperature gas is generally indicative of the presense of a cold dense phase along the line of sight. This is because in these models the warm gas generally has too low an optical depth to contribute more than a few degrees Kelvin to the brightness temperature. Consistent with this, Galactic studies show that, there is no detectable HI absorption along lines of sight where the emission brightness temperature, $T_B < 3-10$K and almost all line-of-sights with $T_B > 3-10$K have detectable absorption (Braun and Walterbos, 1992; Roy et al., 2013b). (Braun, 1997; Braun and Walterbos, 1992) also show that the HI emission observations of gas in the Milky Way and M31 can be well fitted with models in which the brightness temperature is correlated to the opacity. An alternative method for searching for the CNM would then be to look for gas with brightness temperature much larger than say $\sim$ 10K. Indeed this method has previously been used to identify cold, optically thick gas in external galaxies by (Braun, 1997, 2012; Braun and Walterbos, 1992). We refer to this the brigthness temperature method (or T_B method) for detecting the CNM.

Since gas in the CNM phase is expected to be clumpy, a high resolution HI image is a primary requirement to identify the high density cold HI in the brightness temperature method. In low resolution images the high T_B regions will be smoothed over, reducing ones ability to detect the compact peaks. The first step in trying this method on our sample galaxies was hence to re-image all of the galaxies at a spatial resolution of $\sim$ 100 pc. Since for many galaxies the SNR is modest at this high resolution, the data were smoothed up to a velocity resolution of $\sim$ 5 km s^{-1} wherever it was necessary

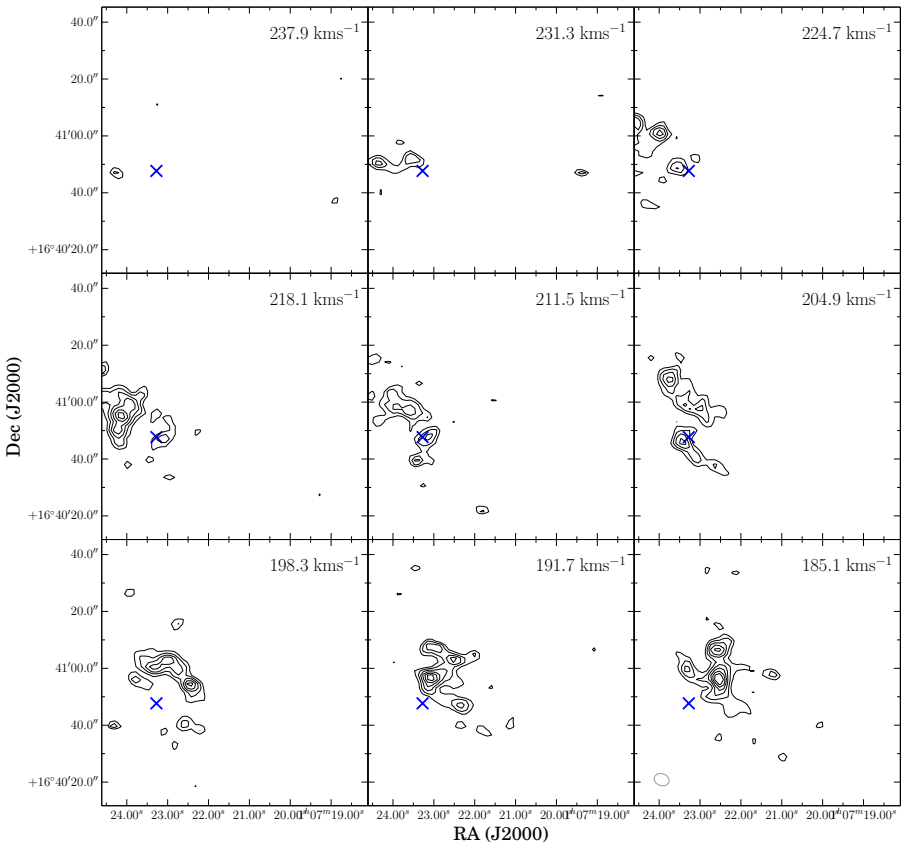

Figure 5.4: The HI channel maps of the galaxy UGC 685 at a spatial resolution of $\sim$ 100 pc. The cross mark spots an emission region, which is seen over several contigous channels (viz. a velocity range from 231 km s^{-1}to 204 km s^{-1}). Our moment map parameters were tuned to pick up only such clearly coherent structures.

(see Tab. 5.1). We note that the parameters that we use here (i.e. spatial resolution of $\sim$ 100 pc and a velocity resolution of $\sim$ 5 km s^{-1}) are similar to those used by (Braun, 1997) to identify high brightness temperature gas.

We then inspected all of the data cubes to make sure that any emission that we detected as real was present at more than a 2σ level in several contiguous channels (of typically 1.6km s^{-1}velocity width). We show for example in Fig. 5.4 the channel maps for UGC 685 at a spatial resolution of $\sim$ 100 pc. The cross traces the location of one of the detected emission regions. As can be seen there is emission in velocities from 231 to 204 km s^{-1}.

In the two-phase models of the ISM (Wolfire et al., 1995b) at low metalicity and low

dust content (as would be appropriate for our dwarf galaxies), the density of the WNM is expected to be in the range of $0.19-1.9$ atoms cm^{-3} and the spin temperature in the range of $5900-8400$ K (Wolfire et al., 1995a). For a region of size ~ 100 pc, the expected optical depth would then be $\lesssim 0.0031$, and the brightness temperature $\lesssim 18$ K. We hence conservatively set a threshold brightness temperature cutoff of $T_B > 50$ K to identify gas that arises from phases other than the classical WNM. For some galaxies, the per channel 2σ rms corresponded to T_B larger than 50 K, for these galaxies the 2σ level was instead used as a cut-off. The actual cut-off used per galaxy is listed in Tab. 5.4. Once we have identified gas with high brightness temperature (which we henceforth refer to as "cold" gas), the next step is to determine the total HI mass producing this emission. Two different approaches were adopted to calculate the cold HI mass from the brightness temperature. In first case we assume that the emission is optically thin, in which case the total column density can be trivially computed from the moment map. While this may not be a good approximation, it does provide a lower limit to the cold HI mass. Our second approach was to assume that the emitting gas has a spin temperature of 500 K, which is a robust upper limit in the two phase models (Wolfire et al., 1995b) for low metalicity gas. We calculated both estimates of the HI mass for all of galaxies in our sample.

5.4.1 Results

The GMRT has a hybrid configuration (Swarup et al., 1991), and for most of our observations the UV coverage allows one to make images at spatial resolutions as high as $\sim 5''$. For 24 of the 62 galaxies in our sample an angular resolution of $\sim 5''$ corresponds to a spatial resolution > 100 pc. These galaxies were dropped from the analysis below, since we wanted to use a uniform linear resolution for all of the galaxies. High resolution images were made for the remaining 38 galaxies, and cold HI (identified using the T_B cutoff of 50K as described above), was detected in 25 of them, corresponding to a detection efficiency of $\sim 65\%$.

In table 5.4 we summarise the results of the cold HI detected using the T_B method. The columns of the table are: Col. (1) the galaxy name. Col. (2) log of the HI mass (in solar units) Col. (3) the absolute blue magnitude Col. (4) the T_B cutoff used to identify cold HI . We set the cut off to 50K or 2σ, which ever is larger. Col. (5) the mass of

Table 5.4: Summary of cold HI search using T_B method.

Name	$\log M_{HI}$ ($M_\odot$)	M_B	$(T_B)_{cut}$ K	$\log(M_{HI})_{thin}$ ($M_\odot$)	$\log(M_{HI})_{thick}$ ($M_\odot$)
DDO125	7.48	−14.30	60.83	5.58	5.62
DDO183	7.31	−13.20	50.00	7.00	7.03
DDO187	7.06	−12.40	139.50	6.39	6.52
DDO210	6.42	−11.10	50.00	4.99	5.01
DDO006	7.04	−12.40	50.00	5.69	5.72
DDO099	7.74	−13.50	50.00	6.66	6.69
ESO379-007	7.51	−12.30	51.16	6.90	6.93
GR8	6.89	−12.00	50.00	5.67	5.69
KK200	6.84	−12.00	53.02	6.36	6.40
KKH11	7.66	−13.30	50.00	7.10	7.12
KKH12	7.23	−13.00	50.00	6.22	6.25
KKH34	6.76	−12.30	69.50	5.73	5.79
KKH6	6.63	−12.40	67.15	6.36	6.41
KKH98	6.45	−10.80	50.00	5.68	5.71
PGC051659	7.78	−13.10	71.02	7.46	7.51
UGC05209	7.15	−13.10	55.11	6.17	6.21
UGC06456	7.77	−14.10	104.81	6.28	6.35
UGC06541	6.97	−13.60	58.50	6.50	6.54
UGC00685	7.74	−14.30	64.70	7.50	7.55
UGC07298	7.28	−12.30	64.41	6.16	6.21
UGC07605	7.32	−13.50	53.39	6.80	6.85
UGC08215	7.27	−12.30	57.73	6.54	6.58
UGC08508	7.30	−13.10	50.00	7.05	7.09
UGC08833	7.00	−12.20	50.00	6.61	6.64
UGCA292	7.44	−11.80	102.00	7.24	7.32

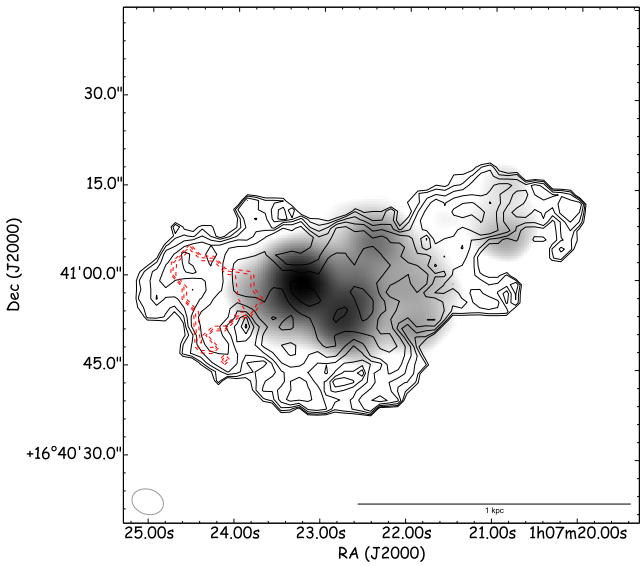

Figure 5.5: Cold HI as recovered by two different methods shown in contours overlaid on Hα map in gray scale. The black solid contours represent cold HI recovered by T_B method and the red broken contours are the same for Gaussian decomposition method. The contours levels are $(1, 1.4, 2, 2.8, 4, 5.6, 8, 11.2, 16, 22.4, ...)$ 1.5×10^{21} atoms cm^{-2}for cold HI detected by T_B method (black solid contours) and $(1, 1.4, 2, 2.8, 4, 5.6, 8, 11.2, 16, 22.4, ...)$ 6.2×10^{20} atoms cm^{-2}for cold HI recovered by Gaussian decomposition method (red dashed contours). The spatial resolution of Hα data and the T_B data is $\sim$ 100 pc.

cold HI estimated assuming the emission to be optically thin. Col. (6) the mass of cold HI estimated assuming the emission to be optically thick.

In figure 5.5 we show the cold HI as detected by the T_B method as well as the Gaussian decomposition method overlayed on the Hα emission for UGC 685. The black solid contour represents the cold HI identified using the T_B method, whereas the red dashed contours show the cold HI identified by the Gaussian decomposition method. From the plot one can see that T_B method identifies gas that correlates with the Hα emission better than the Gaussian decomposition method. In Fig. 5.6 we compare the cold HI fraction recovered by both the methods. As can be seen T_B method recovers significantly more 'cold' gas than the Gaussian decomposition method. In Fig. 5.7 we plot the histograms of detected cold gas fraction in both the methods. Once again it is clear that the T_B method identifies much more cold gas than the Gaussian Decomposition method.

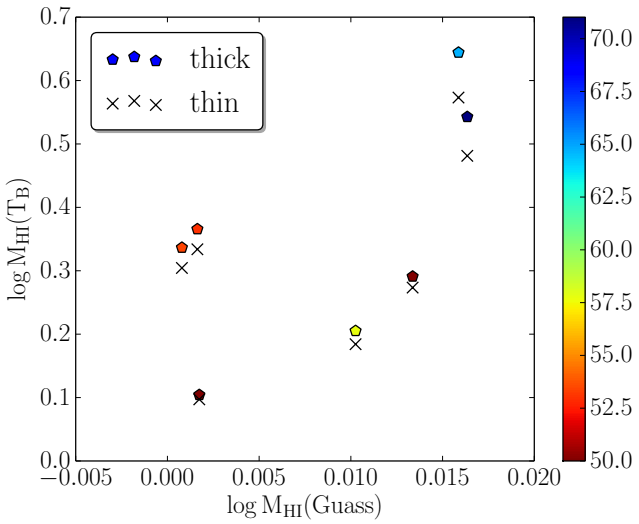

Figure 5.6: Comparison of fractional cold HI detected in the two different methods as discussed in the text. The crosses represents the fractional cold HI mass computed assuming the emission is optically thin, while the pentagons represents the fractional cold HI mass computed assuming a spin temperature of 500K. Color scale represents the brightness temperature cut-off used in T_B method. Data is shown only for those galaxies for which "cold" HI was also detected using the Gaussian Decomposition method. As can be seen the T_B method identifies much more cold gas than the Gaussian Decomposition method.

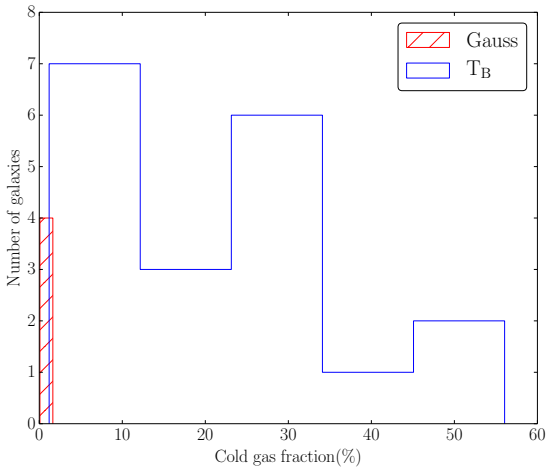

Figure 5.7: Histograms of cold gas fraction.

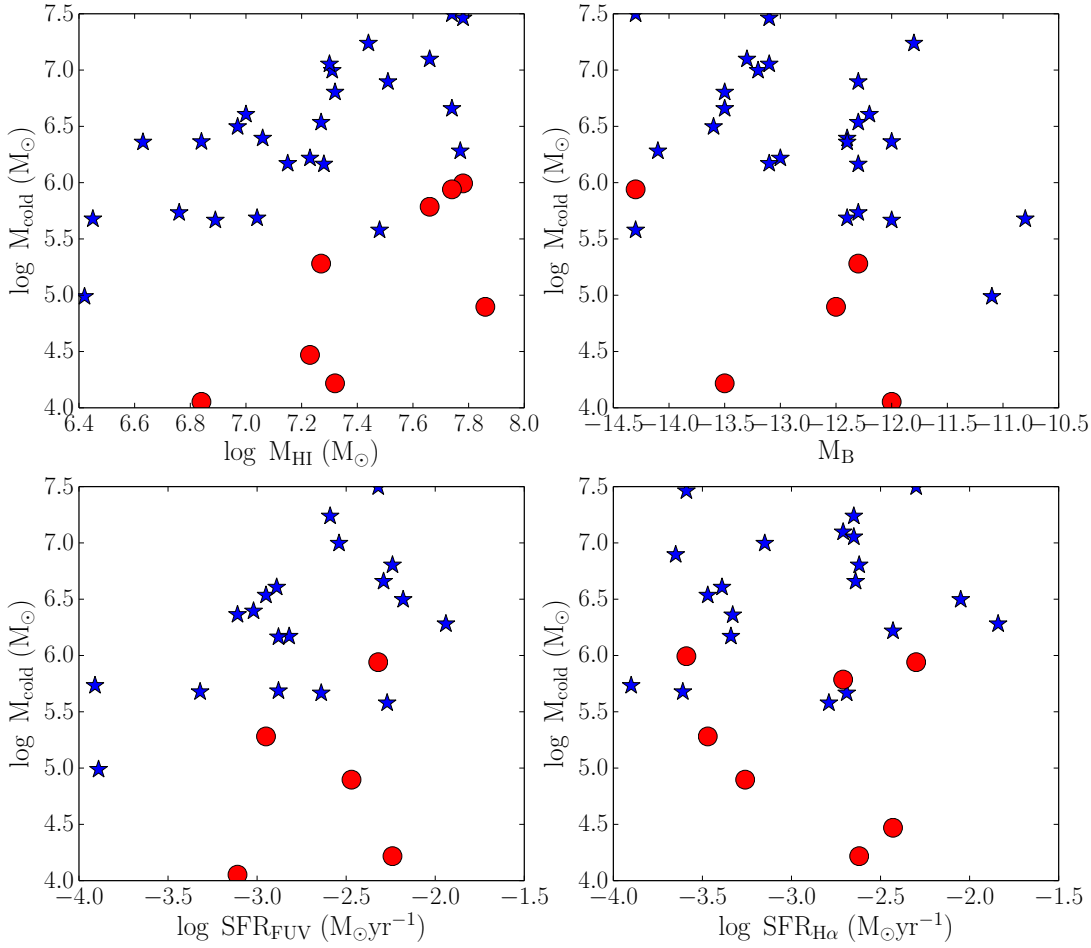

Figure 5.8: In all the panels, filled circles represents cold HI recovered by the Gaussian decomposition method while filled stars represents cold HI recovered by T_B method (optically thin approximation). Top left : The correlation of cold HI with total HI mass (M_{HI}) Top right : The correlation of cold HI with the absolute blue magnitude (M_B). Bottom left : The correlation of cold HI with star formation rate, as deduced from the H_α emission ($SFR_{H\alpha}$). Bottom right: The correlation of cold HI with star formation rate, as deduced from the FUV star-formation rates SFR_{FUV}). One can note that the recovered cold HI masses in two different methods correlate with different global properties of the galaxies. See text for more details.

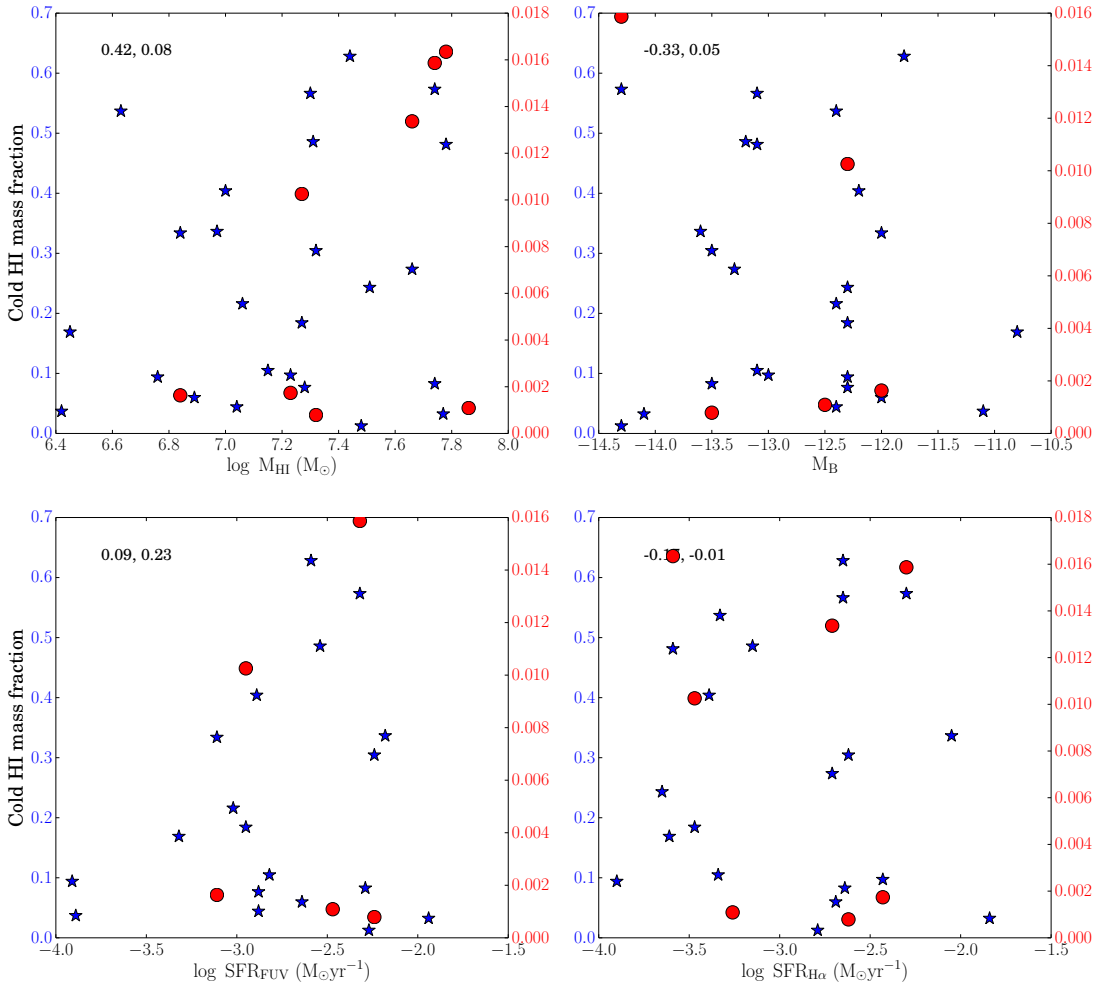

Figure 5.9: In all the panels, filled circles represents cold HI fraction recovered by the Gaussian decomposition method while filled stars represents cold HI fraction recovered by T_B method (optically thin approximation). In all panels the vertical left axes (blue) represent the cold HI fraction recovered by T_B method, whereas the vertical right axes (red) represent cold HI fraction as recovered by Gaussian decomposition method. Top left : The correlation of cold HI fraction with total HI mass (M_{HI}) Top right : The correlation of cold HI fraction with the absolute blue magnitude (M_B). Bottom left : The correlation of cold HI fraction with star formation rate, as deduced from the H_α emission ($SFR_{H\alpha}$). Bottom right: The correlation of cold HI fraction with star formation rate, as deduced from the FUV star-formation rates SFR_{FUV}). See the text for more details on the derivation of the star formation rates.

To investigate the connection between different global properties of galaxies and the detected cold HI , we plot detected cold HI as a function of different global parameters in figure 5.8. The top left panel shows the correlation between cold HI and total HI mass, the top right panel shows the dependence of cold HI as a function of absolute blue magnitude (M_B). The left and right bottom panels represent the dependence of cold HI on global Hα and FUV star formation rates respectively. From the plots it is clear that brighter galaxies with more HI mass and higher star formation rates contain more cold HI . The global Hα and FUV SFR used in the plots were taken from the Updated Nearby Galaxy Catalogue (UNGC) (Karachentsev et al., 2013). The correlation coefficients of various correlations of cold HI with global galaxy properties are quoted in the upper left side of the respective panels of Fig. 5.8. The first number indicates the correlation coefficient with the cold HI detected in Gaissian decomposition method and the second number represents the coefficient with cold HI detected by T_B method.

We also plot the dependence of cold HI fraction detected in Gaussian decomposition and T_B method as a function of different global galaxy properties in Figure 5.9. This plot is similar to the Figure 5.8, except it shows the dependence of cold HI fraction instead of cold HI mass on different global properties. Unlike Figure 5.8, we do not see any significant correlation of cold HI fraction on different global galaxy properties. This is counter-intuitive. It could be due to the fact that our recovery efficiency of cold HI is not uniform across our sample galaxies.

In Fig. 5.10, the total HI is plotted against total global star formation rates. The numbers quoted on the top left of the figure represents the correlation coefficients for Hα , and FUV data respectively. Comparing with Fig. 5.8 one can see that the total HI correlates better with global star-formation than cold HI .

Conversion of atomic gas to the molecular phase is expected to lead to a maximum column density of the atomic phase. At column densities larger than this value the shielding against Lyman-Werner band photons which could dissociate the H_2 molecule (both self-shielding, as well as shielding due to dust) is expected to be sufficient for atomic to the molecular conversion. In our own galaxy for example, the molecular fraction becomes significant above column densities of $\log(N_{HI}) \sim 20.7$ Gillmon and Shull (2006); Gillmon et al. (2006); Savage et al. (1977). If the gas to dust ratio scales with the metalicity one expects that the threshold column density would increase with

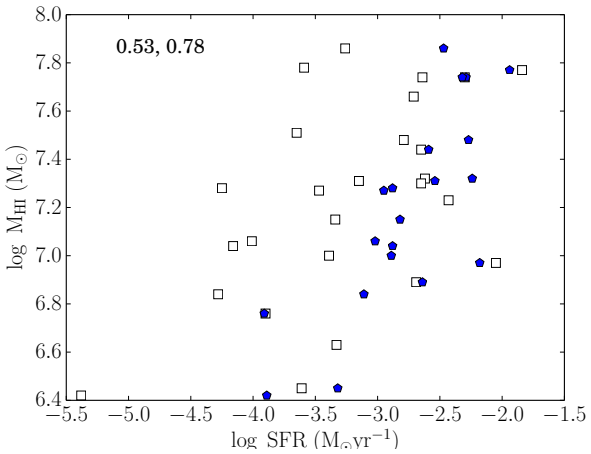

Figure 5.10: Total HI mass is plotted against global star-formation rates. The empty squares represents Hα data and blue pentagons represents FUV data. The numbers quoted on the top left shows the correlation coefficients between total HI and global star-formation rate for Hα and FUV respectively.

decreasing metalicity (since lower metalicity would correspond to lower dust content and hence lower shielding.) In Figure 5.11 the fractional cold HI mass (i.e. the ratio of the cold HI mass detected over the entire sample to the total HI mass of the galaxies in the sample) is plotted as a function the column density of the cold HI . As can be seen the fraction gradually increases with increasing N_{HI} but there is an abrupt cut off near $N_{HI}\sim\ 10^{21.8}$ atoms cm^{-2}. At low column densities, one would expect that the gas would predominantly be in the WNM phase, and indeed in our own galaxy Kanekar et al. (2011) show that there appears to be a threshold density of $\sim 10^{20.3}$ atoms cm^{-2} for the formation of the CNM. Kanekar et al. (2011) suggest that this threshold arises because one needs a critical amount of shielding before the gas can cool down to the CNM phase, while the numerical models of Kim et al. (2014) indicates that this threshold can be understood in terms of vertical equilibrium in the local Milky Way disk. In our observations, since low N_{HI} would correspond to lower brightness temperature and hence a lower signal to noise ratio, the fall off that we see at low column densities could partly be a sensitivity related issue. What is more interesting is the peak HI column density of $\sim 10^{21.8}$ that is seen in our data. (Krumholz et al., 2009) present detailed calculations of the atomic to molecular transition in gas of different metalicities. At the

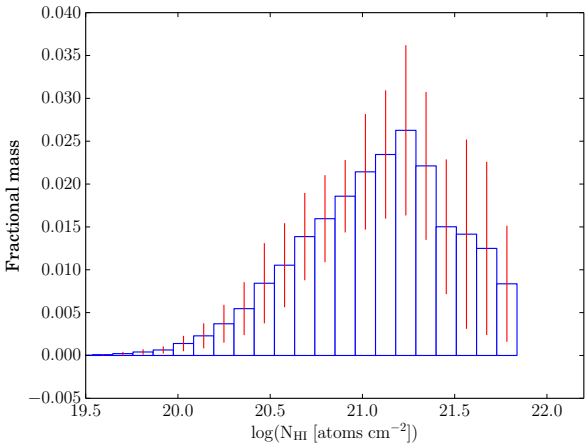

Figure 5.11: The fractional HI mass in the cold phase (as determined by the T_B method) as a function of N_{HI}. At log $N_{HI}\sim$ 21.8 cold HI fraction drops to zero, consistent with the expected threshold column density for conversion of low metallicity (Z$\sim$ 0.1 $Z_\odot$) gas into the molecular phase. (Krumholz et al., 2009).

metalicity of our sample galaxies (i.e. $\sim 0.1\ Z_\odot$), the saturation column density that is predicted by their model (Fig 1. in Krumholz et al. (2009)) is in excellent agreement with the maximum column density seen in Fig. 5.11.

5.5 Summary

We used two different methods to identify cold HI in a sample of dwarf irregular galaxies selected from the FIGGS and FIGGS2 survey. In the first method, line-of-sight HI spectra with SNR greater than 10 were decomposed into multiple Gaussian components. Following earlier studies, Gaussian components having velocity dispersion $\sigma < 6$ km s^{-1}were identified as narrow component and attributed them to cold HI . For a galaxy that is in common between the two samples, we compare narrow velocity dispersion HI detected using this method with that detected using the same technique (but with a different data set, and a different software routine) by (Warren et al., 2012). Despite being observed using two different telescopes and analysed independently, the results are very similar. In our sample we detect narrow velocity dispersion components in 6 galaxies out of the total sample of 15. In common with previous studies, we find that the narrow velocity dispersion components do not overlap with the locations

of cold HI and the locations of Hα emission or high column density regions. This is somewhat surprising if the narrow velocity dispersions are accurately tracing the cold gas content of the galaxies.

We hence used a different method to try and identify cold atomic gas. Since the WNM has low opacity, there is a limit to the brightness temperature expected from physically plausible path lengths through the WNM. Gas with higher T_B than this threshold must be associated with cold gas. Since the CNM is clumpy, high velocity and spatial resolution is required to identify the high T_B gas. We re-imaged our sample galaxies at 100 pc and identified all regions with $T_B > 50$ K as being associated with the CNM. We find that cold gas identified in this way is associated with regions of high HI column density as well as regions with on going star formation. The amount of gas identified as being cold by the T_B method is also significantly larger than the amount of gas identified as being cold using Gaussian Decomposition. We also find that various global properties of the parent galaxies correlate well with the amount of cold HI in the galaxy. Finally we compare the peak HI column density that we observe (at 100 pc resolution) with the largest column density expected in low metallicity gas, and find good agreement with theoretical models.

6

Cold HI and star formation in faint dwarf galaxies

6.1 Introduction

Star formation plays a crucial role in galaxy formation and evolution. Observationally, the gas surface density and star formation rate density in galaxies are found to be related by a power law, (popularly known as "Kennicutt-Schmidt" law) given by

$$\Sigma_{gas} = A(\Sigma_{SFR})^N \tag{6.1}$$

where 'N' is the power-law index and 'A' is the normalising constant. 'A' and 'N' are determined by fitting Eqn. 6.1 to the observed data.

A number of studies have been carried out to quantify Eqn 6.1. Early studies based on galaxy wide averages of $\Sigma_{\rm SFR}$ and $\Sigma_{\rm gas}$ found N to be in the range $1-2$ (e.g. Kennicutt, 1997). These studies, which largely used Hα emission as a tracer of the SFR also found a sharp decline in the SFR below a critical threshold density (Kennicutt, 1998). The resultant star formation recipes hence could be thought as an outcome of various global processes like, large-scale instabilities (e.g. Fall and Efstathiou, 1980; Kennicutt, 1998; Quirk, 1972), differential rotation, etc. Spatially resolved, small linear scale studies allow one to quantify the form of star formation law across a widely different ISM conditions, and relate the star formation rate to more local processes. Recently a number of authors used radial profiles of gas density and star-formation densities to constraint the Schmidt law on intermediate scales (e.g. Boissier et al., 2003; Martin

and Kennicutt, 2001; Schuster et al., 2007). Most of these studies are based on samples of spiral galaxies due to the wealth of data available through large surveys (Dalcanton et al., 2009; Gil de Paz et al., 2007; Kennicutt et al., 2003; Leroy et al., 2009; Walter et al., 2008). While these are important, it is also useful to study the corresponding relation in dwarf galaxies. Since dwarf galaxies have low metallicity and low dust content, their ISM more closely resembles that of high redshift galaxies. Further there are also differences on global scales between spiral and dwarf galaxies. Spiral galaxies have thin, dynamically cold disks, where as dwarfs have thick, dynamically warm gas disks (Roychowdhury et al., 2010). This difference in structure and dynamics is likely to also lead to corresponding differences in the rate at which gas collapses to form stars. Star formation is expected to occur in molecular gas, which is generally traced by its CO emission. A number of studies shows that the cold molecular phase of the ISM traces star formation most closely giving a tight K-S relation as compared to atomic gas which shows a very weak or no correlation (Kennicutt et al., 2007). In dwarf galaxies however, CO emission is generally too faint to be detected (see e.g. Schruba et al., 2012). Since molecular gas is expected to be associated with the CNM, in this chapter we study the relation between cold HI and star formation.

6.2 Sample & Data preparation

6.2.1 The sample

Our sample consists of 25 dwarf galaxies selected from FIGGS (Begum et al., 2008) and FIGGS2 surveys (Chapter 2) for which cold HI has been detected by the T_B method (see §3 and previous chapter). To minimise uncertainties due to de-projection, seven highly inclined galaxies ($i > 70^o$) were excluded from the sample. We estimate the star formation rate either from the `GALEX` FUV emission or Hα emission. Two galaxies (ESO379-007 and UGC8508) did not have `GALEX` data and another four galaxies (KK200, KKH34, KKH6 and UGC5209) were observed as part of the all sky survey, and hence their FUV images have poor SNR. We exclude these six galaxies from our sample which leaves us to a sample of total 12 galaxies with good quality FUV `GALEX` data, as well as cold HI . Similarly we have 6 galaxies of the sub-sample for which Hα images are available. (Note that there are more galaxies for which the total Hα flux is

available, but for the local study that we are doing in this chapter, we also need access to a FITS file of the image.)

In Table 6.1 we describe the general properties of our sample galaxies. The columns are as follows: Col. (1) Galaxy name, Col. (2) and 3) the equatorial coordinates (J2000), Col. (4) and (5) log of HI mass and absolute blue magnitude, Col. (6) the Holmberg diameter (i.e. at a surface brightness of 26.5 mag arcsec^{-2}), Col. (7) the axial ratio, Col. (8) full width at half maxima of the HI line profile, Col. (9) inclination of the optical disc, Col. (10) and (11) represents the global Hα and FUV star-formation rates. Galaxies for which we have access to the Hα images are marked with asterisks. Only these galaxies have been used for the Hα based star formation rate analysis presented in this chapter.

The data in table 6.1 were taken from (Karachentsev et al., 2013). The median HI mass and absolute blue magnitude of our sample galaxies are $10^{7.3}$ M$_\odot$ and -12.4 respectively. A detailed description of observation and data analysis can be found in (Begum et al., 2008) and in Chapter 2. Details of the measurement of the cold gas content can be found in Chapter 5, and below we describe how the star formation rate has been measured.

6.2.2 Estimation of the star formation rate

FUV data were downloaded from the *GALEX* site and were used to prepare SFR$_{\rm FUV}$ maps for our sample galaxies. Only FUV ($1350 - 1750$Å) data were used to derive the star formation as a part of the NUV band ($1750 - 2800$Å) lies outside the range for which calibrations for conversion to the star formation rate are available. Galactic foreground emission was identified by manual inspection of the images, and removed from the FUV map using the task BLANK in AIPS. The FUV maps were then smoothed to the resolution of the HI maps using the task SMOTH in AIPS. The geometries of the smoothed FUV maps were then aligned with that of the HI maps using the task OHGEO. The FUV maps are in units of counts per second which can be converted into FUV flux using the calibration provided in *GALEX* site

$$m_{GALEX} = -2.5 \log(counts\ s^{-1}) \tag{6.2}$$

$$m_{AB} = m_{GALEX} + 18.82 \tag{6.3}$$

Using the above equations FUV flux maps were generated and corrected for the galactic dust extinction using the dust map of (Schlafly and Finkbeiner, 2011). The formulae given by (Cardelli et al., 1989) were used to extrapolate the extinction to the FUV band. For the internal dust correction, we adopt the approach described in detail in (Roychowdhury et al., 2014). Briefly, 24 μm *Spitzer* observations of FIGGS galaxies were used to derive a numerical relation between FUV star formation rate and 24 μm flux. The 24 μm flux can be given as:

$$\log F_{24\mu m}(Jy) = 1.78\ \log SFR_{FUV}(M_{\odot}yr^{-1}) + 2.62 \tag{6.4}$$

This corrected emergent FUV luminosity is then corrected for internal dust extinction using relation given by (Hao et al., 2011)

$$L_{FUV,corr} = L_{FUV,obs} + 3.89\ L_{24\mu m} \tag{6.5}$$

The FUV luminosity of equation 6.5 can then be converted into the star formation rate using the calibration given by (Hao et al., 2011; Kennicutt and Evans, 2012)

$$\log \dot{M}_{*}(M_{\odot}yr^{-1}) = \log L_x - \log C_x \tag{6.6}$$

where $L_x = \nu L_{\nu}$ is in the units of $ergs\ s^{-1}$ and $\log C_x = 43.35$. This calibration assumes an ongoing star formation for $\sim\ 10^8$ yr and a Salpeter IMF with solar metallicity. Studies of the star formation rate of nearby dIrr galaxies (Weisz et al., 2012) indicate that the assumption that the star formation rate has been approximately constant for the last $\sim 10^8$ yr is a reasonable one, however we do need to correct the star formation rate estimated above for the metallicity.

The typical metallicity of the dwarf galaxies in our sample is Z$\sim$ 0.1 (Roychowdhury et al., 2014). Metallicity measurements are available only for a few of our sample galaxies (e.g. Marble et al., 2010; Moustakas and Kennicutt, 2006). For the rest of our galaxies, we use the M_B-Z metallicity relation for dIrs from (Ekta and Chengalur, 2010) to estimate their metallicity. In Table 6.1 we list the metallicity estimated for our sample galaxies. The star formation rate estimated above hence needs to be corrected to account for this. Raiter et al. (Raiter et al., 2010) calculate the emergent FUV fluxes

in sub-solar metallicity environment using evolutionary synthesis model assuming a continuous star formation for 10^8 yrs and a Salpeter IMF. They show that the emergent FUV flux increases by $\sim$ 11%, 19%, 27% & 32% for 0.4, 0.2, 0.05 and 0.02 times solar metallicity respectively. For each sample galaxy we do a linear interpolation between these tabulated values to get the metallicity correction to the FUV flux.

The star formation rate density was also computed using Hα data largely taken from the 6m BTA telescope in Russia. For a detailed analysis of Hα data see (Kaisin and Karachentsev, 2008; Karachentsev and Kaisin, 2007). As can be seen from Tab. 6.1 Hα images were available only for six galaxies in the sample of galaxies with detected cold HI . The Hα data were processed exactly the same way (foreground subtraction, smoothing to $\sim$ 100 pc resolution, geometrical alignment) as the FUV data. To derive the star-formation rate from Hα map we used Kennicutt's calibration, equation (4) with L_x in the units of $ergs\ s^{-1}$ and $\log C_x = 41.27$. This calibration also assumes a Salpeter IMF with a continuous star-formation for $3-10$ Myr. We note that at low star formation rates, the Hα emission becomes unreliable as a tracer of the star formation rate largely because of stochastic effects in the number of high mass stars observed at any instant (da Silva et al., 2014). The actual star formation rate as deduced from the Hα emission for our sample should hence be treated with caution.

6.2.3 Measurement of the cold HI column density

A detailed description of the brightness temperature based method used to identify cold HI detection in our sample of galaxies can be found in Chapter 5. Briefly, previous galactic as well as extra galactic studies show that all lines of sight with brightness temperature larger than some threshold (typically few degrees Kelvin) have some associated CNM (Braun and Walterbos, 1992; Roy et al., 2013b). This can be understood as being a consequence of the very low optical depth of the WNM – to get more than a few degree Kelvin of brightness temperature would require unphysically long path lengths through the WNM. We hence identify gas with very high T_B as being in the CNM phase. Since the CNM is clumpy, the brightness temperature is smoothed to lower values when one observes with insufficient resolution. We hence reimage our galaxies at $\sim$ 100pc resolution in order to identify the CNM clumps. All gas with brightness temperature cube greater than a threshold (typically 50K) T_B are identified as being

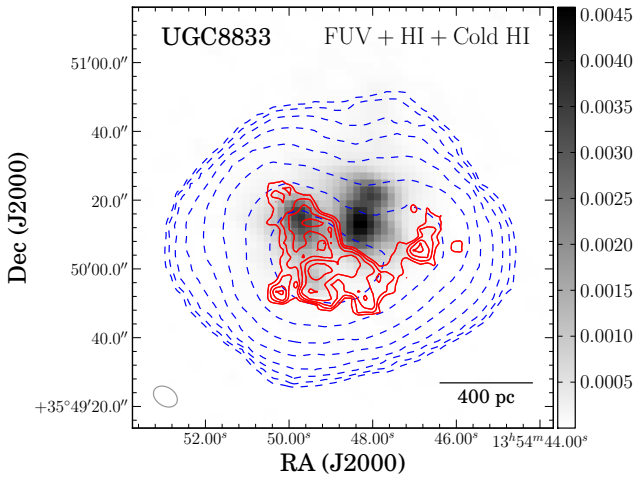

Figure 6.1: Total HI column density distribution (blue, dotted contours) and the "cold" HI column density distribution (red, solid contours) overlayed on the FUV SFR for UGC8833. The blue broken contours represents total HI , red solid contours present cold HI using T_B method. The red contour levels are $(1, 1.4, 2, 2.8, ...) \times (5 \times 10^{20}$atoms cm^{-2}. The color bar shows the star-formation rate density in units of $M_\odot yr^{-1} kpc^{-2}$.

in the CNM phase. The gas column density was estimated assuming the emission to be optically thin, which is a strict lower limit to the actual column density.

In Figure 6.1 we show the total HI column density distribution (blue, dotted contours) , as well as the cold HI column density distribution (red, solid contours) overlayed on the star formation rate density (gray scale) as measured from the FUV emission for UGC8833. One can see that the cold HI is concentrated within central region of this galaxy and that it has significant overlap with the FUV emission.

To compute the face on column density of cold gas and surface density of star formation rate at the same spatial location we deproject the observed column densities using the inclination angles given in Table 6.1. We also multiply the HI surface density by a factor 1.34 to account for the presence of helium. In several plots we average over several regions lying within a given Σ_{HI}, or Σ_{SFR} bin in order to improve the signal to noise ratio and reduce the effects of stochasticity in the star formation rate.

Table 6.1: Sample galaxy properties

Name	RA (J2000)	DEC (J2000)	$\log M_{HI}$ ($M_\odot$)	M_B	Metallicity ($Z_\odot$)	D_{opt} ($''$)	b/a	W_{50} (km s^{-1})	incl (^{o})	$\log SFR_{H\alpha}$ ($M_\odot yr^{-1}$)	$\log SFR_{FUV}$ ($M_\odot yr^{-1}$)
DDO125	122741.8	+432938	7.48	−14.3	0.12	3.89	0.56	27	66	−2.79	−2.27
DDO187	141556.5	+230319	7.06	−12.4	0.11†	1.70	0.76	31	46	−4.01	−3.02
GR8	125840.4	+141303	6.89	−12.0	0.09	1.66	0.91	26	27	−2.69	−2.64
KKH98	234534.0	+384304	6.45	−10.8	0.04	1.05	0.55	21	67	−3.61*	−3.32
UGC06456	112800.6	+785929	7.77	−14.1	0.10‡	1.48	0.53	37	69	−1.84*	−1.94
UGC06541	113329.1	+491417	6.97	−13.6	0.13	1.74	0.57	26	65	−2.05	−2.18
UGC00685	010722.3	+164102	7.74	−14.3	0.20†	2.40	0.71	64	51	−2.30*	−2.32
UGC07298	121628.6	+521338	7.28	−12.3	0.06	0.85	0.55	21	67	−4.25	−2.88
UGC07605	122839.0	+354305	7.32	−13.5	0.09	1.48	0.73	26	49	−2.62*	−2.24
UGC08215	130803.6	+464941	7.27	−12.3	0.06	0.85	0.70	25	52	−3.47	−2.95
UGC08833	135448.7	+355015	7.00	−12.2	0.06	1.17	0.89	28	30	−3.39*	−2.89
UGCA292	123840.0	+324600	7.44	−11.8	0.05	1.02	0.70	27	52	−2.54	−2.59
UGC08508	133044.4	+545436	7.30	−13.1	0.08	2.14	0.59	46	63	−2.65*	–

References: † : (Marble et al., 2010); ‡ : (Moustakas and Kennicutt, 2006)

Table 6.2: Derived quantities during data analysis

Galaxy	Beam ($''\times''$)	Beam (pc × pc)	Δv (km s^{-1})	Noise (mJy/Beam)
DDO125	6×5	79×66	1.7	1.7
DDO187	5×3	57×36	3.3	2.1
GR8	12×12	123×121	1.7	2.3
KKH98	9×4	117×60	3.3	1.3
UGC06456	5×3	125×77	1.6	1.9
UGC06541	4×4	85×77	3.3	0.9
UGC00685	5×4	117×91	6.6	1.2
UGC07298	5×3	119×78	1.7	1.2
UGC07605	4×3	89×76	3.3	0.7
UGC08215	4×4	97×89	3.3	0.8
UGC08833	7×5	111×80	1.7	1.2
UGCA292	4×3	70×62	1.7	1.2

6.3 Results & Discussion

6.3.1 Cold gas with associated star formation

To examine the association of cold HI with recent star formation, we compute the area covered by pixels with detected cold gas which also have a star formation rate density greater than the 3σ level of the FUV SFR map, and normalizing this area by the total area covered by cold gas alone. In Figure 6.2 we plot the histogram of fractional cold gas with associated star formation for our sample galaxies. We note that most of the cold HI has some associated star formation; the median fractional area is $\sim$ 84%. It is possible that deeper FUV observations could show star formation associated with all of the gas. In any case, this exercise indicates that cold dense atomic gas in dwarf galaxies is closely associated with recent star formation. In Figure 6.3 we show a similar histogram, but this time using the the star formation rate as deduced from the Hα emission.

It is also interesting to see if all star forming regions have associated cold HI . In Figure 6.4), we show the fractional area with both cold HI and recent star formation (as traced by FUV emission) normalised by total area covered by regions with recent star formation. We find that for most of the galaxies, $\lesssim 10\%$ of the regions with recent star

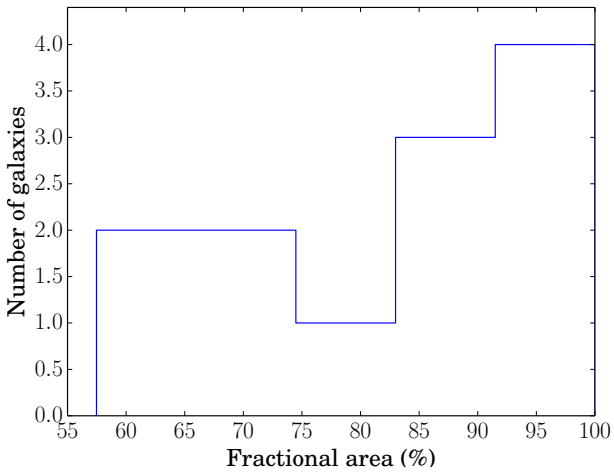

Figure 6.2: Histogram of areal fraction of cold HI with associated recent star formation (as measured from the FUV emission). The median fraction is 84%

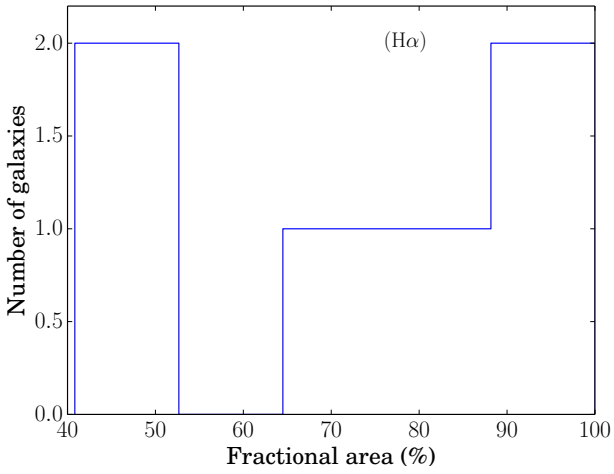

Figure 6.3: Histogram of areal fraction of cold HI that is associated with recent star formation (as measured from the Hα emission). The median fraction is $\sim$ 75%.

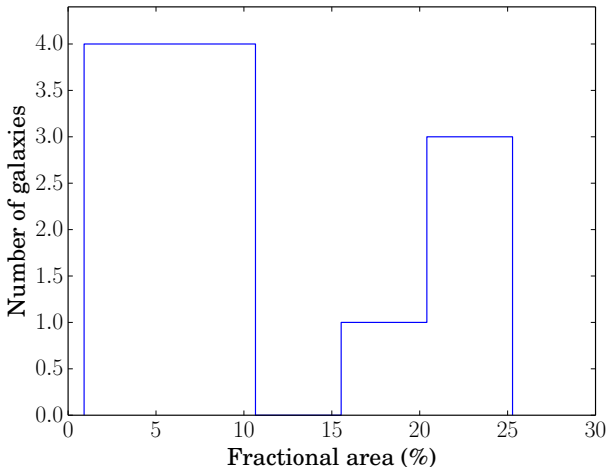

Figure 6.4: Histogram of areal fraction of recent star formation (as measured from the FUV emission) that is is associated with recent star formation. The median fraction is $\sim$ 8%.

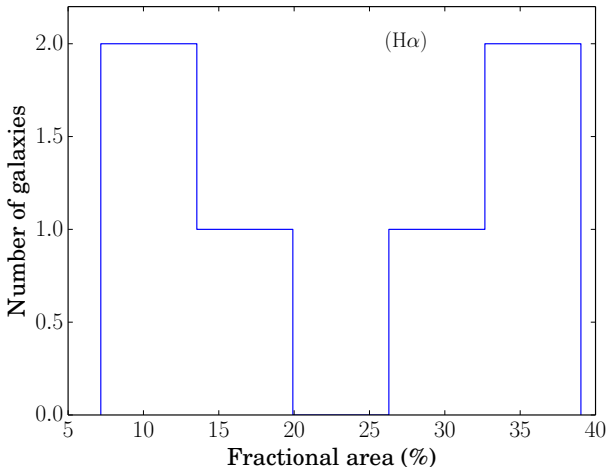

Figure 6.5: Histogram of areal fraction of recent star formation (as measured from the Hα emission) with associated cold HI . The median fraction is $\sim$ 24%.

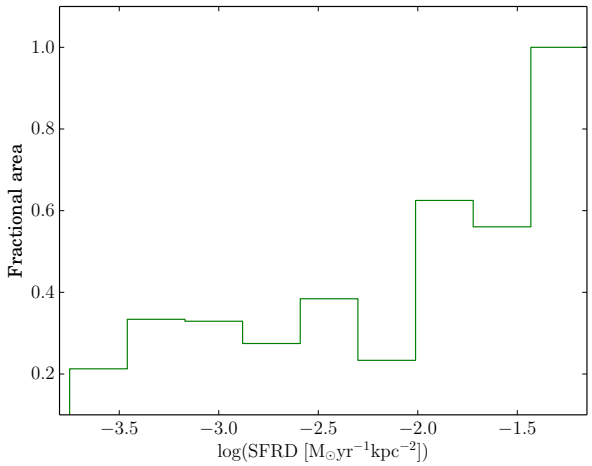

Figure 6.6: Histogram of areal fraction of recent star formation (as measured from the Hα emission) with associated cold HI , as a function of the star formation rate. At the highest star formation rates essentially all of the star forming regions have associated cold gas.

formation have associated cold HI ; the median fraction is $\sim 8\%$. So, although most of the regions with cold HI have some associated recent star formation, the converse is not true. It is interesting to note that in the case of the recent star formation as estimated from the Hα emission (which traces much more recent star formation than FUV) a larger fraction ($\sim 24\%$) of the star forming regions have associated cold HI . We show in Fig. 6.6 how this fraction varies as a function of the star formation rate. As can be seen, at the highest star formation rates, essentially all of the star forming regions have associated cold gas.

6.3.2 The Kennicutt-Schmidt law for cold HI

In Figure 6.7 we plot the star formation rate surface density as a function of cold gas surface density. We use only the FUV estimates of the star formation rates, since, as discussed earlier these are more reliable at the low star formation rates typical of our sample. The cold gas surface density is defined as the HI column density multiplied by a factor of 1.34 to account for the presence of Helium. The red filled circles with error bars represent our data, the black dashed line represents the canonical K-S law

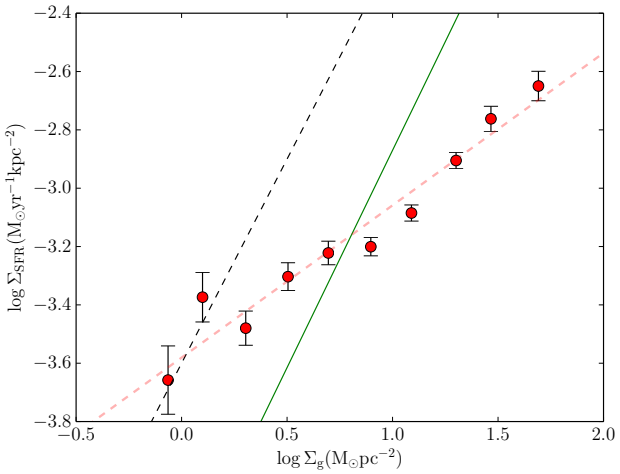

Figure 6.7: The Kennicutt-Schmidt law for cold HI . The filled points with error bars represent data points from our sample galaxies using the star formation rate as measured from the FUV emission. The thick red dashed line represents a straight line fit to the data. The green solid line represents K-S law for FIGGS galaxies (Roychowdhury et al., 2014), measured using the total gas content (i.e. not just the cold gas) at 400 pc resolution. The thin black dashed line represents the canonical K-S law (Kennicutt, 1998).

(Kennicutt, 1998) and the green solid line represents K-S law for FIGGS galaxies at 400 pc resolution (and using the total gas content, not just the cold gas) taken from (Roychowdhury et al., 2009). The thick pink dashed line shows a linear fit to our data (i.e. for the cold gas alone). For this data, we find a slope of 0.52 ± 0.04 with an intercept of -3.58 ± 0.04. As mentioned above, most previous studies of the KS law find slopes between 1-2 (e.g. Bigiel et al., 2008; Kennicutt, 1997; Roychowdhury et al., 2009, 2014). A steeper slope indicates a higher dependency of Σ_{SFR} on the total HI . The molecular gas is believed to be the raw fuel of star formation and hence the star formation is expected to be most closely related to molecular gas. In earlier studies (e.g. Kennicutt, 1989) it has been found that the total gas (HI + H_2) is more strongly correlated to star formation than only molecular gas. But with better CO data, recent studies found that the molecular gas correlates closely with many star formation indicators in disk galaxies (Leroy et al., 2013). Even then, the slope of the schmidt type power law is shallower in the case of molecular gas as compared to the case of total gas or only atomic gas (Kennicutt, 1998; Roychowdhury et al., 2009). In our study, we found a very shallow slope (0.52 ± 0.04) of Kennicutt-schmidt law with cold HI . A flat slope indicates a higher gas depletion time scale and hence a less efficient star formation. The reason for this shallow Kennicutt-schmidt law is not clear to us though, it indicates that the total HI is better correlated to the star formation (and hence presumably the molecular gas) than the cold HI .

6.4 Summary

We study the relationship between the cold HI detected using the T_B method and recent star formation. For our sample of galaxies we find that regions with cold HI are almost always have associated recent star formation (as traced by FUV emission), ∼ 85% of the cold gas has some associated recent star formation. The converse however is not true, only ∼ 8% of the area covered by regions with recent star formation is associated with cold HI . In the case of Hα emission (which traces more recent star formation) the fraction of star forming regions that are associated with cold HI is significantly higher. In fact, at the highest star formation rates, essentially all of the star forming regions are associated with cold HI . If we focus on the regions were there is overlap between cold gas and recent star formation, (and use the FUV estimates of the star formation

rates, which are more reliable at low SFR) we find that $\Sigma_{\rm SFR}$ correlated to $\Sigma_{\rm HI}$, albeit with a slope ($\sim 0.52 \pm 0.04$) that is significantly flatter than that seen in earlier studies which used the total (as opposed to the cold) gas content. This suggests that the total HI may be a better tracer of $\Sigma_{\rm SFR}$ (and hence $\Sigma_{\rm H_2}$) than the cold dense HI .

7

Summary of the thesis

In this thesis we have addressed several questions related to the interstellar medium in dwarf galaxies. Our analysis was based on data available for the FIGGS sample, as well as its extension FIGGS2. The FIGGS2 data is presented in this thesis for the first time. We use the HI data to measure the HI column density distribution function $f(N_{HI})$ of local volume dwarf galaxies and compare it to that measured in high redshift DLAs. We also study the phase structure of the atomic ISM of dwarf galaxies, with the aim of identifying cold gas, and its connection (if any) with recent star formation. Finally, we also studied and modeled the HI vertical structure of a dwarf galaxy KK250.

7.1 Key results

7.1.1 FIGGS2 an extension of FIGGS survey

The FIGGS2 survey is an extension to fainter galaxies of the earlier FIGGS (Begum et al., 2008) survey. The median absolute blue magnitude of FIGGS2 samples is -11.7 which about one magnitude fainter than the FIGGS sample. A total of 21 galaxies were observed in HI with the Giant Meter wave Radio Telescope (GMRT), and HI emission was detected in 15 of them. Complementary multi wavelength data is also available for most of these galaxies. In chapter 2 we presented the observations and data analysis for our sample galaxies along with few preliminary results.

7.1.2 HI column density distribution in faint dwarfs

The high column density Damped Lyman-alpha Absorbing systems (DLAS) are known to contain the bulk of the neutral gas at high redshifts. As such, DLAS are the best available high redshift precursors of the gas rich galaxies at present epoch. However, despite decades of study the nature of the DLAS hosts are not yet firmly established. Two extremes of the models that have been proposed are i) DLAS arise from large rotating discs, much like disc of modern day spirals (e.g. Prochaska and Wolfe, 1997; Wolfe et al., 1986) and ii) DLAS arises from small systems analogous to the current day dwarf galaxies. Recent numerical studies (e.g. Cen, 2012; Pontzen et al., 2008) indicate a more nuanced picture where a range of hosts gives rise to DLAS. Because the information available from absorption studies is limited by its pencil beam absorption line, a quantitative comparison of DLAS and local volume galaxies is difficult. The column density distribution function ($f(\mathrm{N_{HI}})$), (which gives the expected numbers of absorbers per unit distance with column densities between $\mathrm{N_{HI}}$ and $\mathrm{N_{HI}}$+$\mathrm{dN_{HI}}$) is one of the few statistics which can be computed for both local volume galaxies and high redshift DLAS.

We determined $f(\mathrm{N_{HI}})$ in faint dwarfs and compared it with the $f(\mathrm{N_{HI}})$ of DLAS. We found that the $f(\mathrm{N_{HI}})$ in dwarfs falls off significantly faster at high column densities than the $f(\mathrm{N_{HI}})$ in DLAS or in the $f(\mathrm{N_{HI}})$ determined from a representative sample of local galaxy population. In the local universe, $\sim 10\%$ of the cross section above $\mathrm{N_{HI}}= 10^{20.3}$ atoms $\mathrm{cm^{-2}}$ at $z = 0$ is provided by dwarf galaxies but the fraction falls to $\lesssim 1\%$ by $\mathrm{N_{HI}}\sim 10^{21.5}$ atoms $\mathrm{cm^{-2}}$. The contribution to high $\mathrm{N_{HI}}$ end of the $f(\mathrm{N_{HI}})$ distribution comes predominantly from the inclined discs of large galaxies. Dwarf galaxies, both because of their smaller scale lengths and their larger intrinsic axial ratios do not produce large column densities even when viewed at edge-on. If high column density DLAS/GRB hosts corresponds to galaxies like the local dwarfs, this would require either that (i) the absorption arises from merging and not isolated systems or (ii) the observed lines of sight are strongly biased towards high column density regions.

7.1.3 Vertical scaleheight & HI kinematics in an edge-on dwarf KK250

In galaxies, the underlying gravitational field determines the vertical gas distribution via the hydrostatic equilibrium equation. Hence the vertical gas distribution can be used to trace the gravitational field and hence the underlying dark matter halo. Since the HI disc extends much farther than optical disc, measurement of HI vertical scale-height in nearby galaxies allows one to trace the shape of dark matter halo to large galactocentric radius (Banerjee and Jog, 2008; Banerjee et al., 2010, 2011a; Becquaert and Combes, 1997; Narayan et al., 2005; Olling, 1995). In particular the HI scale height of dwarf galaxies are very interesting for several reasons. For example; (Brinks et al., 2002) postulated that the dwarf galaxies have a larger gas scaleheights than normal spiral galaxies which is supported by the observations of (Roychowdhury et al., 2010). This will have several implications if we indeed consider that local volume dwarfs are somewhat similar to the galaxies at early universe. For e.g. a thick HI disc will prevent an early breakout of HI shells and hence reduce escape of enriched gas into the IGM.

However a direct measurement of vertical scaleheight is not possible even for a edge-on galaxy, unless the scale height is constant with radius and the gas is optically thin (Sancisi and Allen, 1979). The vertical scaleheight is hence generally obtained via modelling of the gas distribution. While modelling of vertical gas distribution can be useful in many contexts, comparison of models with observations are complicated by the following problems. The vertical HI distribution can be constrained by the observation of edge-on galaxies but in this case estimating the gas velocity dispersion (which is crucial input to the hydrostatic equilibrium model) is not possible. On the other hand for face-on systems velocity dispersions can be estimated but the vertical scaleheight cannot be constrained. The fact that it is difficult to measure the vertical gas distribution and gas velocity dispersion simultaneously makes it difficult to build a completely data driven model. In our study instead of using a fixed gas velocity dispersion, we use it as a free parameter to our model. We build a grid of models (with different variations of velocity dispersions with galactocentric radius) and compute synthetic HI cubes and moment maps for every model. We finally select the model which best matches the observed HI distribution.

We apply this technique to GMRT HI data for the dwarf irregular galaxy KK 250. We model the galaxy as a two component gravitationally bound system of stars and gas

in vertical hydrostatic equilibrium under the external force field of a fixed dark matter halo. The gas velocity dispersion is considered as a free parameter to the model. For the best fit model we also compare the model line-of-sight velocity width with observed width and find that they are in excellent agreement with each other. This gives further support to the correctness of the model. From the best fit model we find that velocity dispersion is maximum at the centre and rapidly falls to a value ~ 8 km s^{-1}at a radius $R \sim 1$ kpc. This is similar to the both scale length of the optical disc and resolution of HI data in radial direction. The intrinsic HI scaleheight also reaches to a minimum value at $R \sim 1$ kpc. The disk of KK250 is significantly thicker than that of spiral galaxies, consistent with the idea that dwarf galaxies have in general puffier disks.

7.1.4 Cold HI and star formation in faint dwarf galaxies

From theoretical models, one expects the atomic interstellar medium of galaxies to exist in two stable phases, a cold dense phase (CNM) and a warm diffuse phase (WNM). The typical temperature of the CNM is $\sim$ 100K, while that of the WNM is significantly higher ($\sim 5000 - 8000$K). Observational studies in both our own galaxy, as well as external spiral and dwarf galaxies have established that the HI in these systems does indeed have a multi-phase structure. We use our HI data to study the phase structure of the gas in our sample of galaxies.

We used two different techniques to identify CNM. In the first method we developed a routine to decompose line-of-sight HI spectra into multiple Gaussian components; 'narrow' velocity width components, were then identified with the CNM. We characterised our routine and find that the recovery efficiency of 'narrow' components (15-20%) is consistent with previous works (Warren et al., 2012). Using this method we detected cold HI in 6 galaxies out of total 15 galaxies which meet our selection criteria. Amongst the non-detections, we do not find any significant trend with other global properties of the galaxies. We also find the location of detected cold HI does not coincide with either the high HI column density gas, or recent star forming regions (as traced by Hα emission). This is somewhat surprising, as one would expect that cold HI would be associated with both high HI column density regions as well as recent star formation.

In the second method we use the brightness temperature (T_B) as a tracer of cold dense HI . Because of its low optical depth, typical path lenghts through the WNM

would give rise to no more than a few K of brigthness temperature. Regions with higher T_B are hence likely to be associated with the CNM. Since the CNM is clumpy, one needs high spatial and velocity resolution images to identify high T_B gas. We hence re-imaged all our sample galaxies at a spatial resolution of $\sim$ 100 pc. To detect cold HI in T_B method we used a cutoff brightness temperature of $\sim$ 50 K. With this cut-off, we detect cold HI in 25 galaxies out of the 38 galaxies which could be imaged at high resolution. The detection efficiency is $\sim$ 65%. We find that the detected cold HI is associated with star forming regions – $\sim$ 85% of the cold gas has associated star formation. However, the reverse is not true, only $\sim$ 8% regions with recent star formation (as traced by FUV emission) are found to have associated cold HI . However, if we use the Hα emission (which traces much more recent star formation than the FUV emission) we find that a larger fraction of the star forming regions are associated with cold gas. This fraction increases with the star formation rate, and at the highest star formation rates, essentially all of the star forming regions are associated with cold HI .

We also used cold HI that is associated with star formation in T_B method to study the K-S law at very high spatial resolution ($\sim$ 100 pc) in our sample dwarf galaxies. We found that the star formation rate does correlate with the column density of the cold HI , however with a very flat slope of 0.52 ± 0.04. The flattening of the K-S law suggests that the total HI correlates better with the SFR (and hence with the total molecular gas) than the cold dense gas alone.

7.2 Scope for future work

In chapter 2 we described the FIGGS2 survey: An HI survey of extremely faint gas-rich dwarf irregular galaxies. In this survey we have detected 15 new ultra-faint dwarf galaxies in HI . In Fig 2.4 we have over plotted the HI contours on top of the optical images of the galaxies. It can be noted that for many of these galaxies (e.g. AGC112521, KK15, KKH37, KKH46, UGC4879, KK152, LVJ1243+4127) the HI centers are significantly displaced from their optical centers. A feedback from star formation on these low mass galaxies (with shallow potential well) could be one of the possible reasons for this though, the HI contours do not show enough evidence of that. We do not understand clearly the reasons for this offset. Hence a detailed study to investigate the cause of this offset as well as its dynamical implications would be really interesting.

7. SUMMARY OF THE THESIS

In this thesis we have used *GALEX* FUV images as well as Hα images for estimating the current star formation rate. The number of galaxies for which we have detected cold HI and for which either sufficiently deep FUV or Hα images are available is quite small. It would be good to have a significantly larger sample to place our findings on a statistically firmer footing. In this context we note that there have been a number of recent surveys of Hα emission from dwarf galaxies (e.g. kai; Kaisin et al., 2012, etc.). In the same context of comparing CMM with recent star formation, it would be very interesting to investigate if the strong active star forming regions satisfy Toomre stability criterion or not.

The second area where there is significant scope for improvement is in the detection of cold HI in dwarf galaxies. As we discuss in the thesis, the T_B method appears more suited than the Gaussian Decomposition method for detecting cold HI in dwarfs. In this thesis we have restricted ourselves to a spatial resolution of ~ 100 pc in order to ensure a reasonable signal to noise ratio. This is a marginal resolution as far as the clumpiness of the CNM is concerned. It would be good to image a sub-sample of our galaxies with significantly higher signal to noise ratio to see if one could (a) use this method at higher spatial resolution and (b) get a more complete census of the population of dense gas clouds in these galaxies. Deep HI observations may also reveal small scale kinematical features associated with recent star formation (e.g. as traced by the Hα emission). The issue of mechanical feed back from star formation is an important one in dwarf galaxies, and it would be interesting to get observational constraints on this.

In this thesis we have built a detailed dynamical model of one dwarf galaxy (KK250), which allowed us to constrain the velocity dispersion in the gas. It would be useful to extend this kind of modelling to a sample of dwarf galaxies, so that one can try and gain an understanding of the velocity dispersion in galaxies, as well as the connections (if any) with star formation. The model that we have built is based on vertical equilibrium between the vertical momentum flux and the gravity. The gravitational potential was computed using the standard Newtonian theory of gravity. Models which use a different theory of gravity (e.g. **MO**dified **N**ewtonian **D**ynamics Milgrom (1983)) would predict a different vertical structure for the HI disk. Constructing such models, and comparing them with observations could provide an interesting observational test of such theories.

Bibliography

K. N. Abazajian, J. K. Adelman-McCarthy, M. A. Agüeros, S. S. Allam, C. Allende Prieto, D. An, K. S. J. Anderson, S. F. Anderson, J. Annis, N. A. Bahcall, and et al. The Seventh Data Release of the Sloan Digital Sky Survey. *ApJS*, 182:543, June 2009. doi: 10.1088/0067-0049/182/2/543.

G. Altay, T. Theuns, J. Schaye, N. H. M. Crighton, and C. Dalla Vecchia.

E. Audit and P. Hennebelle. Thermal condensation in a turbulent atomic hydrogen flow. *A&A*, 433:1–13, April 2005. doi: 10.1051/0004-6361:20041474.

J. N. Bahcall, P. S. Osmer, and M. Schmidt. ON the Absorption Spectrum of Ton 1530. *ApJL*, 156:L1, April 1969. doi: 10.1086/180336.

P. L. Baker and W. B. Burton. Investigation of low-latitude hydrogen emission in terms of a two-component interstellar gas model. *ApJ*, 198:281–297, June 1975. doi: 10.1086/153605.

A. Banerjee and C. J. Jog. The Flattened Dark Matter Halo of M31 as Deduced from the Observed H I Scale Heights. *ApJ*, 685:254–260, September 2008. doi: 10.1086/591223.

A. Banerjee, L. D. Matthews, and C. J. Jog. Dark matter dominance at all radii in the superthin galaxy UGC 7321. *NewA*, 15:89–95, January 2010. doi: 10.1016/j.newast.2009.05.015.

A. Banerjee, C. J. Jog, E. Brinks, and I. Bagetakos. Theoretical determination of H I vertical scale heights in the dwarf galaxies DDO 154, Ho II, IC 2574 and NGC 2366. *MNRAS*, 415:687–694, July 2011a. doi: 10.1111/j.1365-2966.2011.18745.x.

BIBLIOGRAPHY

A. Banerjee, C. J. Jog, E. Brinks, and I. Bagetakos. Theoretical determination of H I vertical scale heights in the dwarf galaxies DDO 154, Ho II, IC 2574 and NGC 2366. *MNRAS*, 415:687–694, July 2011b. doi: 10.1111/j.1365-2966.2011.18745.x.

J.-F. Becquaert and F. Combes. The 3D geometry of Dark Matter Halos. *A&A*, 325: 41–56, September 1997.

A. Begum and J. N. Chengalur. Kinematics of two dwarf galaxies in the NGC 6946 group. *A&A*, 424:509–517, September 2004. doi: 10.1051/0004-6361:20041210.

A. Begum, J. N. Chengalur, and U. Hopp. The little galaxy that could: Kinematics of Camelopardalis B. *NewA*, 8:267–280, May 2003. doi: 10.1016/S1384-1076(02) 00238-5.

A. Begum, J. N. Chengalur, and S. Bhardwaj. Power spectrum of HI intensity fluctuations in DDO 210. *MNRAS*, 372:L33–L37, October 2006. doi: 10.1111/j.1745-3933. 2006.00220.x.

A. Begum, J. N. Chengalur, I. D. Karachentsev, M. E. Sharina, and S. S. Kaisin. FIGGS: Faint Irregular Galaxies GMRT Survey - overview, observations and first results. *MNRAS*, 386:1667–1682, May 2008. doi: 10.1111/j.1365-2966.2008.13150.x.

V. Belokurov, D. B. Zucker, N. W. Evans, J. T. Kleyna, S. Koposov, S. T. Hodgkin, M. J. Irwin, G. Gilmore, M. I. Wilkinson, M. Fellhauer, D. M. Bramich, P. C. Hewett, S. Vidrih, J. T. A. De Jong, J. A. Smith, H.-W. Rix, E. F. Bell, R. F. G. Wyse, H. J. Newberg, P. A. Mayeur, B. Yanny, C. M. Rockosi, O. Y. Gnedin, D. P. Schneider, T. C. Beers, J. C. Barentine, H. Brewington, J. Brinkmann, M. Harvanek, S. J. Kleinman, J. Krzesinski, D. Long, A. Nitta, and S. A. Snedden. Cats and Dogs, Hair and a Hero: A Quintet of New Milky Way Companions. *ApJ*, 654:897–906, January 2007. doi: 10.1086/509718.

F. Bigiel, A. Leroy, F. Walter, E. Brinks, W. J. G. de Blok, B. Madore, and M. D. Thornley. The Star Formation Law in Nearby Galaxies on Sub-Kpc Scales. *AJ*, 136: 2846–2871, December 2008. doi: 10.1088/0004-6256/136/6/2846.

F. Bigiel, A. Leroy, F. Walter, L. Blitz, E. Brinks, W. J. G. de Blok, and B. Madore. Extremely Inefficient Star Formation in the Outer Disks of Nearby Galaxies. *AJ*, 140:1194–1213, November 2010. doi: 10.1088/0004-6256/140/5/1194.

J. Binney, F. Alouani Bibi, and H. Omma. Bubbles as tracers of heat input to cooling flows. *MNRAS*, 377:142–146, May 2007. doi: 10.1111/j.1365-2966.2007.11575.x.

D. L. Block, I. Puerari, B. G. Elmegreen, and F. Bournaud. A Two-component Power Law Covering Nearly Four Orders of Magnitude in the Power Spectrum of Spitzer Far-infrared Emission from the Large Magellanic Cloud. *ApJL*, 718:L1–L6, July 2010. doi: 10.1088/2041-8205/718/1/L1.

S. Boissier, N. Prantzos, A. Boselli, and G. Gavazzi. The star formation rate in disc galaxies: thresholds and dependence on gas amount. *MNRAS*, 346:1215–1230, December 2003. doi: 10.1111/j.1365-2966.2003.07170.x.

N. Bouché, M. T. Murphy, C. Péroux, T. Contini, C. L. Martin, N. M. Forster Schreiber, R. Genzel, D. Lutz, S. Gillessen, L. Tacconi, R. Davies, and F. Eisenhauer. Enriched haloes at redshift z = 2 with no star formation: implications for accretion and wind scenarios. *MNRAS*, 419:2–13, January 2012. doi: 10.1111/j.1365-2966.2011.19500.x.

R. Braun. The Temperature and Opacity of Atomic Hydrogen in Spiral Galaxies. *ApJ*, 484:637–655, July 1997.

R. Braun. Cosmological Evolution of Atomic Gas and Implications for 21 cm H I Absorption. *ApJ*, 749:87, April 2012. doi: 10.1088/0004-637X/749/1/87.

R. Braun and R. A. M. Walterbos. Physical properties of neutral gas in M31 and the Galaxy. *ApJ*, 386:120–138, February 1992. doi: 10.1086/170998.

E. Brinks, F. Walter, and J. Ott. Bloated Dwarfs: The Thickness of the HI Disks in Irregular Galaxies. In E. Athanassoula, A. Bosma, and R. Mujica, editors, *Disks of Galaxies: Kinematics, Dynamics and Peturbations*, volume 275 of *Astronomical Society of the Pacific Conference Series*, pages 57–60, December 2002.

M. T. Busha, M. A. Alvarez, R. H. Wechsler, T. Abel, and L. E. Strigari. The Impact of Inhomogeneous Reionization on the Satellite Galaxy Population of the Milky Way. *ApJ*, 710:408–420, February 2010. doi: 10.1088/0004-637X/710/1/408.

J. M. Cannon, R. Giovanelli, M. P. Haynes, S. Janowiecki, A. Parker, J. J. Salzer, E. A. K. Adams, E. Engstrom, S. Huang, K. B. W. McQuinn, J. Ott, A. Saintonge, E. D. Skillman, J. Allan, G. Erny, P. Fliss, and A. Smith. The Survey of H I

in Extremely Low-mass Dwarfs (SHIELD). *ApJL*, 739:L22, September 2011. doi: 10.1088/2041-8205/739/1/L22.

J. A. Cardelli, G. C. Clayton, and J. S. Mathis. The relationship between infrared, optical, and ultraviolet extinction. *ApJ*, 345:245–256, October 1989. doi: 10.1086/167900.

C. L. Carilli, W. Lane, A. G. de Bruyn, R. Braun, and G. K. Miley. Redshifted H I 21 cm Line Observations of Damped Ly A Absorption Systems. *AJ*, 112:1317, September 1996. doi: 10.1086/118103.

R. Cen. The Nature of Damped Lyα Systems and Their Hosts in the Standard Cold Dark Matter Universe. *ApJ*, 748:121, April 2012. doi: 10.1088/0004-637X/748/2/121.

H.-W. Chen and K. M. Lanzetta. The Nature of Damped Lyα Absorbing Galaxies at $z < 1$: A Photometric Redshift Survey of Damped Lyα Absorbers. *ApJ*, 597:706–729, November 2003. doi: 10.1086/378635.

H.-W. Chen, D. A. Perley, L. K. Pollack, J. X. Prochaska, J. S. Bloom, M. Dessauges-Zavadsky, M. Pettini, S. Lopez, A. Dall'aglio, and G. D. Becker. High-Redshift Starbursting Dwarf Galaxies Revealed by γ-Ray Burst Afterglows. *ApJ*, 691:152–174, January 2009. doi: 10.1088/0004-637X/691/1/152.

J. N. Chengalur and N. Kanekar. Implications of 21-cm observations for damped Lyα systems. *MNRAS*, 318:303–308, October 2000. doi: 10.1046/j.1365-8711.2000.03793.x.

J. N. Chengalur, N. Kanekar, and N. Roy. Accurate measurement of the H I column density from H I 21 cm absorption-emission spectroscopy. *MNRAS*, 432:3074–3079, July 2013. doi: 10.1093/mnras/stt658.

B. G. Clark. An Interferometer Investigation of the 21-CENTIMETER Hydrogen-Line Absorption. *ApJ*, 142:1398, November 1965. doi: 10.1086/148426.

C. J. Conselice, J. A. Blackburne, and C. Papovich. The Luminosity, Stellar Mass, and Number Density Evolution of Field Galaxies of Known Morphology from z = 0.5 to 3. *ApJ*, 620:564–583, February 2005. doi: 10.1086/426102.

R. L. da Silva, M. Fumagalli, and M. R. Krumholz. SLUG - Stochastically Lighting Up Galaxies - II. Quantifying the effects of stochasticity on star formation rate indicators. *MNRAS*, 444:3275–3287, November 2014. doi: 10.1093/mnras/stu1688.

J. J. Dalcanton, B. F. Williams, A. C. Seth, A. Dolphin, J. Holtzman, K. Rosema, E. D. Skillman, A. Cole, L. Girardi, S. M. Gogarten, I. D. Karachentsev, K. Olsen, D. Weisz, C. Christensen, K. Freeman, K. Gilbert, C. Gallart, J. Harris, P. Hodge, R. S. de Jong, V. Karachentseva, M. Mateo, P. B. Stetson, M. Tavarez, D. Zaritsky, F. Governato, and T. Quinn. The ACS Nearby Galaxy Survey Treasury. *ApJS*, 183: 67–108, July 2009. doi: 10.1088/0067-0049/183/1/67.

W. J. G. de Blok and F. Walter. The Star Formation Threshold in NGC 6822. *AJ*, 131:363–374, January 2006. doi: 10.1086/497828.

W. J. G. de Blok, F. Walter, E. Brinks, C. Trachternach, S.-H. Oh, and R. C. Kennicutt, Jr. High-Resolution Rotation Curves and Galaxy Mass Models from THINGS. *AJ*, 136:2648, December 2008. doi: 10.1088/0004-6256/136/6/2648.

W. Dehnen. Phase-space mixing and the merging of cusps. *MNRAS*, 360:892–900, July 2005. doi: 10.1111/j.1365-2966.2005.09099.x.

J. Diemand, M. Kuhlen, P. Madau, M. Zemp, B. Moore, D. Potter, and J. Stadel. Clumps and streams in the local dark matter distribution. *Natur*, 454:735–738, August 2008. doi: 10.1038/nature07153.

P. Dutta and S. Bharadwaj. The H I column density power spectrum of six nearby spiral galaxies. *MNRAS*, 436:L49–L53, November 2013. doi: 10.1093/mnrasl/slt110.

P. Dutta, A. Begum, S. Bharadwaj, and J. N. Chengalur. A study of interstellar medium of dwarf galaxies using HI power spectrum analysis. *MNRAS*, 398:887–897, September 2009. doi: 10.1111/j.1365-2966.2009.15105.x.

B. Ekta and J. N. Chengalur. When are extremely metal-deficient galaxies extremely metal deficient? *MNRAS*, 406:1238–1247, August 2010. doi: 10.1111/j.1365-2966.2010.16756.x.

BIBLIOGRAPHY

B. G. Elmegreen, S. Kim, and L. Staveley-Smith. A Fractal Analysis of the H I Emission from the Large Magellanic Cloud. *ApJ*, 548:749–769, February 2001. doi: 10.1086/319021.

D. Erkal, N. Y. Gnedin, and A. V. Kravtsov. On the Origin of the High Column Density Turnover in the H I Column Density Distribution. *ApJ*, 761:54, December 2012. doi: 10.1088/0004-637X/761/1/54.

S. M. Fall and G. Efstathiou. Formation and rotation of disc galaxies with haloes. *MNRAS*, 193:189–206, October 1980.

G. B. Field and W. C. Saslaw. A Statistical Model of the Formation of Stars and Interstellar Clouds. *ApJ*, 142:568, August 1965. doi: 10.1086/148318.

G. B. Field, D. W. Goldsmith, and H. J. Habing. Cosmic-Ray Heating of the Interstellar Gas. *ApJL*, 155:L149, March 1969. doi: 10.1086/180324.

J. P. U. Fynbo, P. Laursen, C. Ledoux, P. Møller, A. K. Durgapal, P. Goldoni, B. Gullberg, L. Kaper, J. Maund, P. Noterdaeme, G. Östlin, M. L. Strandet, S. Toft, P. M. Vreeswijk, and T. Zafar. Galaxy counterparts of metal-rich damped Lyα absorbers - I. The case of the z = 2.35 DLA towards Q2222-0946. *MNRAS*, 408:2128–2136, November 2010. doi: 10.1111/j.1365-2966.2010.17294.x.

J. P. U. Fynbo, C. Ledoux, P. Noterdaeme, L. Christensen, P. Møller, A. K. Durgapal, P. Goldoni, L. Kaper, J.-K. Krogager, P. Laursen, J. R. Maund, B. Milvang-Jensen, K. Okoshi, P. K. Rasmussen, T. J. Thorsen, S. Toft, and T. Zafar. Galaxy counterparts of metal-rich damped Lyα absorbers - II. A solar-metallicity and dusty DLA at z_{abs}= 2.58. *MNRAS*, 413:2481–2488, June 2011. doi: 10.1111/j.1365-2966.2011.18318.x.

S. Genel, M. Vogelsberger, V. Springel, D. Sijacki, D. Nelson, G. Snyder, V. Rodriguez-Gomez, P. Torrey, and L. Hernquist. Introducing the Illustris project: the evolution of galaxy populations across cosmic time. *MNRAS*, 445:175–200, November 2014. doi: 10.1093/mnras/stu1654.

G. Gentile, P. Salucci, U. Klein, D. Vergani, and P. Kalberla. The cored distribution of dark matter in spiral galaxies. *MNRAS*, 351:903–922, July 2004. doi: 10.1111/j.1365-2966.2004.07836.x.

A. Gil de Paz, S. Boissier, B. F. Madore, M. Seibert, Y. H. Joe, A. Boselli, T. K. Wyder, D. Thilker, L. Bianchi, S.-C. Rey, R. M. Rich, T. A. Barlow, T. Conrow, K. Forster, P. G. Friedman, D. C. Martin, P. Morrissey, S. G. Neff, D. Schiminovich, T. Small, J. Donas, T. M. Heckman, Y.-W. Lee, B. Milliard, A. S. Szalay, and S. Yi. The GALEX Ultraviolet Atlas of Nearby Galaxies. *ApJS*, 173:185–255, December 2007. doi: 10.1086/516636.

K. Gillmon and J. M. Shull. Molecular Hydrogen in Infrared Cirrus. *ApJ*, 636:908–915, January 2006. doi: 10.1086/498055.

K. Gillmon, J. M. Shull, J. Tumlinson, and C. Danforth. A FUSE Survey of Interstellar Molecular Hydrogen toward High-Latitude AGNs. *ApJ*, 636:891–907, January 2006. doi: 10.1086/498053.

R. Giovanelli, M. P. Haynes, B. R. Kent, P. Perillat, A. Saintonge, N. Brosch, B. Catinella, G. L. Hoffman, S. Stierwalt, K. Spekkens, M. S. Lerner, K. L. Masters, E. Momjian, J. L. Rosenberg, C. M. Springob, A. Boselli, V. Charmandaris, J. K. Darling, J. Davies, D. Garcia Lambas, G. Gavazzi, C. Giovanardi, E. Hardy, L. K. Hunt, A. Iovino, I. D. Karachentsev, V. E. Karachentseva, R. A. Koopmann, C. Marinoni, R. Minchin, E. Muller, M. Putman, C. Pantoja, J. J. Salzer, M. Scodeggio, E. Skillman, J. M. Solanes, C. Valotto, W. van Driel, and L. van Zee. The Arecibo Legacy Fast ALFA Survey. I. Science Goals, Survey Design, and Strategy. *AJ*, 130: 2598–2612, December 2005. doi: 10.1086/497431.

F. Governato, A. Zolotov, A. Pontzen, C. Christensen, S. H. Oh, A. M. Brooks, T. Quinn, S. Shen, and J. Wadsley. Cuspy no more: how outflows affect the central dark matter and baryon distribution in Λ cold dark matter galaxies. *MNRAS*, 422: 1231–1240, May 2012. doi: 10.1111/j.1365-2966.2012.20696.x.

M. G. Haehnelt, M. Steinmetz, and M. Rauch. Damped Lyα Absorber at High Redshift: Large Disks or Galactic Building Blocks? *ApJ*, 495:647–658, March 1998. doi: 10.1086/305323.

C.-N. Hao, R. C. Kennicutt, B. D. Johnson, D. Calzetti, D. A. Dale, and J. Moustakas. Dust-corrected Star Formation Rates of Galaxies. II. Combinations of Ultraviolet and Infrared Tracers. *ApJ*, 741:124, November 2011. doi: 10.1088/0004-637X/741/2/124.

BIBLIOGRAPHY

C. Heiles and T. H. Troland. The Millennium Arecibo 21 Centimeter Absorption-Line Survey. I. Techniques and Gaussian Fits. *ApJS*, 145:329–354, April 2003a. doi: 10.1086/367785.

C. Heiles and T. H. Troland. The Millennium Arecibo 21 Centimeter Absorption-Line Survey. I. Techniques and Gaussian Fits. *ApJS*, 145:329–354, April 2003b. doi: 10.1086/367785.

C. Heiles and T. H. Troland. The Millennium Arecibo 21 Centimeter Absorption-Line Survey. II. Properties of the Warm and Cold Neutral Media. *ApJ*, 586:1067–1093, April 2003c. doi: 10.1086/367828.

P. W. Hodge. Dwarf Galaxies. *ARA&A*, 9:35, 1971. doi: 10.1146/annurev.aa.09.090171.000343.

W. K. Huchtmeier, I. D. Karachentsev, V. E. Karachentseva, and M. Ehle. HI observations of nearby galaxies . I. The first list of the Karachentsev catalog. *A&AS*, 141: 469–490, February 2000. doi: 10.1051/aas:2000324.

W. K. Huchtmeier, I. D. Karachentsev, and V. E. Karachentseva. HI-observations of dwarf galaxies in the Local Supercluster. *A&A*, 506:677–680, November 2009. doi: 10.1051/0004-6361/200911774.

D. A. Hunter, D. Ficut-Vicas, T. Ashley, E. Brinks, P. Cigan, B. G. Elmegreen, V. Heesen, K. A. Herrmann, M. Johnson, S.-H. Oh, M. P. Rupen, A. Schruba, C. E. Simpson, F. Walter, D. J. Westpfahl, L. M. Young, and H.-X. Zhang. Little Things. *AJ*, 144:134, November 2012. doi: 10.1088/0004-6256/144/5/134.

M. Johnson, D. A. Hunter, S.-H. Oh, H.-X. Zhang, B. Elmegreen, E. Brinks, E. Tollerud, and K. Herrmann. The Stellar and Gas Kinematics of the LITTLE THINGS Dwarf Irregular Galaxy NGC 1569. *AJ*, 144:152, November 2012. doi: 10.1088/0004-6256/144/5/152.

J. L. Jonas. MeerKAT - The South African Array With Composite Dishes and Wide-Band Single Pixel Feeds. *IEEE Proceedings*, 97:1522–1530, August 2009. doi: 10.1109/JPROC.2009.2020713.

S. S. Kaisin and I. D. Karachentsev. Canes Venatici I cloud of galaxies seen in the Hα line. *A&A*, 479:603–624, February 2008. doi: 10.1051/0004-6361:20078652.

S. S. Kaisin, I. D. Karachentsev, and S. Ravindranath. Hα survey of nearby dwarf galaxies. *MNRAS*, 425:2083–2098, September 2012. doi: 10.1111/j.1365-2966.2012.21501.x.

N. Kanekar and J. N. Chengalur. A deep search for 21-cm absorption in high redshift damped Lyman-alpha systems. *A&A*, 399:857–868, March 2003. doi: 10.1051/0004-6361:20021922.

N. Kanekar, J. N. Chengalur, R. Subrahmanyan, and P. Petitjean. ATCA search for 21 cm emission from a candidate damped Ly-alpha absorber at z = 0.101. *A&A*, 367: 46–50, February 2001. doi: 10.1051/0004-6361:20000420.

N. Kanekar, J. N. Chengalur, A. G. de Bruyn, and D. Narasimha. Detection of OH and wide HI absorption toward B0218+357. *MNRAS*, 345:L7–L11, October 2003. doi: 10.1046/j.1365-8711.2003.07077.x.

N. Kanekar, A. Smette, F. H. Briggs, and J. N. Chengalur. A Metallicity-Spin Temperature Relation in Damped Lyα Systems. *ApJL*, 705:L40–L44, November 2009. doi: 10.1088/0004-637X/705/1/L40.

N. Kanekar, R. Braun, and N. Roy. An H I Column Density Threshold for Cold Gas Formation in the Galaxy. *ApJL*, 737:L33, August 2011. doi: 10.1088/2041-8205/737/2/L33.

I. D. Karachentsev and S. S. Kaisin. A View of the M81 Galaxy Group via the Hα Window. *AJ*, 133:1883–1902, May 2007. doi: 10.1086/512127.

I. D. Karachentsev, V. E. Karachentseva, W. K. Huchtmeier, and D. I. Makarov. A Catalog of Neighboring Galaxies. *AJ*, 127:2031–2068, April 2004. doi: 10.1086/382905.

I. D. Karachentsev, D. I. Makarov, and E. I. Kaisina. Updated Nearby Galaxy Catalog. *AJ*, 145:101, April 2013. doi: 10.1088/0004-6256/145/4/101.

BIBLIOGRAPHY

R. C. Kennicutt. From gas to stars: regulation of star formation. In *Astrophysics and Space Science Library*, volume 161 of *Astrophysics and Space Science Library*, pages 171–195, 1997.

R. C. Kennicutt and N. J. Evans. Star Formation in the Milky Way and Nearby Galaxies. *ARA&A*, 50:531–608, September 2012. doi: 10.1146/annurev-astro-081811-125610.

R. C. Kennicutt, Jr. The star formation law in galactic disks. *ApJ*, 344:685–703, September 1989. doi: 10.1086/167834.

R. C. Kennicutt, Jr. The Global Schmidt Law in Star-forming Galaxies. *ApJ*, 498: 541–552, May 1998. doi: 10.1086/305588.

R. C. Kennicutt, Jr., L. Armus, G. Bendo, D. Calzetti, D. A. Dale, B. T. Draine, C. W. Engelbracht, K. D. Gordon, A. D. Grauer, G. Helou, D. J. Hollenbach, T. H. Jarrett, L. J. Kewley, C. Leitherer, A. Li, S. Malhotra, M. W. Regan, G. H. Rieke, M. J. Rieke, H. Roussel, J.-D. T. Smith, M. D. Thornley, and F. Walter. SINGS: The SIRTF Nearby Galaxies Survey. *PASP*, 115:928–952, August 2003. doi: 10.1086/376941.

R. C. Kennicutt, Jr., D. Calzetti, F. Walter, G. Helou, D. J. Hollenbach, L. Armus, G. Bendo, D. A. Dale, B. T. Draine, C. W. Engelbracht, K. D. Gordon, M. K. M. Prescott, M. W. Regan, M. D. Thornley, C. Bot, E. Brinks, E. de Blok, D. de Mello, M. Meyer, J. Moustakas, E. J. Murphy, K. Sheth, and J. D. T. Smith. Star Formation in NGC 5194 (M51a). II. The Spatially Resolved Star Formation Law. *ApJ*, 671:333–348, December 2007. doi: 10.1086/522300.

C.-G. Kim, E. C. Ostriker, and W.-T. Kim. Three-dimensional Hydrodynamic Simulations of Multiphase Galactic Disks with Star Formation Feedback. II. Synthetic H I 21 cm Line Observations. *ApJ*, 786:64, May 2014. doi: 10.1088/0004-637X/786/1/64.

R. S. Klessen and P. Hennebelle. Accretion-driven turbulence as universal process: galaxies, molecular clouds, and protostellar disks. *A&A*, 520:A17, September 2010. doi: 10.1051/0004-6361/200913780.

A. Klypin, A. V. Kravtsov, O. Valenzuela, and F. Prada. Where Are the Missing Galactic Satellites? *ApJ*, 522:82–92, September 1999. doi: 10.1086/307643.

S. E. Koposov, J. Yoo, H.-W. Rix, D. H. Weinberg, A. V. Macciò, and J. M. Escudé. A Quantitative Explanation of the Observed Population of Milky Way Satellite Galaxies. *ApJ*, 696:2179–2194, May 2009. doi: 10.1088/0004-637X/696/2/2179.

S. E. Koposov, H.-W. Rix, and D. W. Hogg. Constraining the Milky Way Potential with a Six-Dimensional Phase-Space Map of the GD-1 Stellar Stream. *ApJ*, 712: 260–273, March 2010. doi: 10.1088/0004-637X/712/1/260.

B. S. Koribalski, L. Staveley-Smith, V. A. Kilborn, S. D. Ryder, R. C. Kraan-Korteweg, E. V. Ryan-Weber, R. D. Ekers, H. Jerjen, P. A. Henning, M. E. Putman, M. A. Zwaan, W. J. G. de Blok, M. R. Calabretta, M. J. Disney, R. F. Minchin, R. Bhathal, P. J. Boyce, M. J. Drinkwater, K. C. Freeman, B. K. Gibson, A. J. Green, R. F. Haynes, S. Juraszek, M. J. Kesteven, P. M. Knezek, S. Mader, M. Marquarding, M. Meyer, J. R. Mould, T. Oosterloo, J. O'Brien, R. M. Price, E. M. Sadler, A. Schröder, I. M. Stewart, F. Stootman, M. Waugh, B. E. Warren, R. L. Webster, and A. E. Wright. The 1000 Brightest HIPASS Galaxies: H I Properties. *AJ*, 128:16–46, July 2004. doi: 10.1086/421744.

J. Kormendy and K. C. Freeman. Scaling Laws for Dark Matter Halos in Late-Type and Dwarf Spheroidal Galaxies. In S. Ryder, D. Pisano, M. Walker, and K. Freeman, editors, *Dark Matter in Galaxies*, volume 220 of *IAU Symposium*, page 377, July 2004.

A. V. Kravtsov. Modeling Galaxy Clustering with Cosmological Simulations. *ArXiv Astrophysics e-prints*, July 2006.

M. R. Krumholz, C. F. McKee, and J. Tumlinson. The Star Formation Law in Atomic and Molecular Gas. *ApJ*, 699:850–856, July 2009. doi: 10.1088/0004-637X/699/1/850.

V. P. Kulkarni, J. Meiring, D. Som, C. Péroux, D. G. York, P. Khare, and J. T. Lauroesch. A Super-damped Lyα Quasi-stellar Object Absorber at z = 2.2. *ApJ*, 749:176, April 2012. doi: 10.1088/0004-637X/749/2/176.

M. Lacy, R. H. Becker, L. J. Storrie-Lombardi, M. D. Gregg, T. Urrutia, and R. L. White. Imaging and Spectroscopy of Galaxies Associated with Two z˜0.7 Damped Lyα Absorption Systems. *AJ*, 126:2230–2236, November 2003. doi: 10.1086/378957.

BIBLIOGRAPHY

V. Le Brun, J. Bergeron, P. Boisse, and J. M. Deharveng. The nature of intermediate-redshift damped Lyα absorbers. *A&A*, 321:733–748, May 1997.

C. Ledoux, P. Petitjean, J. Bergeron, E. J. Wampler, and R. Srianand. On the kinematics of damped Lyman-alpha systems. *A&A*, 337:51–63, September 1998.

A. K. Leroy, F. Walter, E. Brinks, F. Bigiel, W. J. G. de Blok, B. Madore, and M. D. Thornley. The Star Formation Efficiency in Nearby Galaxies: Measuring Where Gas Forms Stars Effectively. *AJ*, 136:2782–2845, December 2008. doi: 10.1088/0004-6256/136/6/2782.

A. K. Leroy, A. Bolatto, C. Bot, C. W. Engelbracht, K. Gordon, F. P. Israel, M. Rubio, K. Sandstrom, and S. Stanimirović. The Structure of a Low-metallicity Giant Molecular Cloud Complex. *ApJ*, 702:352–367, September 2009. doi: 10.1088/0004-637X/702/1/352.

A. K. Leroy, F. Walter, K. Sandstrom, A. Schruba, J.-C. Munoz-Mateos, F. Bigiel, A. Bolatto, E. Brinks, W. J. G. de Blok, S. Meidt, H.-W. Rix, E. Rosolowsky, E. Schinnerer, K.-F. Schuster, and A. Usero. Molecular Gas and Star Formation in nearby Disk Galaxies. *AJ*, 146:19, August 2013. doi: 10.1088/0004-6256/146/2/19.

Y.-S. Li, A. Helmi, G. De Lucia, and F. Stoehr. On the common mass scale of the Milky Way satellites. *MNRAS*, 397:L87–L91, July 2009. doi: 10.1111/j.1745-3933.2009.00690.x.

M.-M. Mac Low and R. S. Klessen. Control of star formation by supersonic turbulence. *Reviews of Modern Physics*, 76:125–194, January 2004. doi: 10.1103/RevModPhys.76.125.

S. Malhotra. The Vertical Distribution and Kinematics of H i and Mass Models of the Galactic Disk. *ApJ*, 448:138, July 1995. doi: 10.1086/175946.

A. R. Marble, C. W. Engelbracht, L. van Zee, D. A. Dale, J. D. T. Smith, K. D. Gordon, Y. Wu, J. C. Lee, R. C. Kennicutt, E. D. Skillman, L. C. Johnson, M. Block, D. Calzetti, S. A. Cohen, H. Lee, and M. D. Schuster. An Aromatic Inventory of the Local Volume. *ApJ*, 715:506–540, May 2010. doi: 10.1088/0004-637X/715/1/506.

A. M. Martin, E. Papastergis, R. Giovanelli, M. P. Haynes, C. M. Springob, and S. Stierwalt. The Arecibo Legacy Fast ALFA Survey. X. The H I Mass Function and Ω_H I from the 40% ALFALFA Survey. *ApJ*, 723:1359–1374, November 2010. doi: 10.1088/0004-637X/723/2/1359.

C. L. Martin and R. C. Kennicutt, Jr. Star Formation Thresholds in Galactic Disks. *ApJ*, 555:301–321, July 2001. doi: 10.1086/321452.

C. F. McKee and M. R. Krumholz. The Atomic-to-Molecular Transition in Galaxies. III. A New Method for Determining the Molecular Content of Primordial and Dusty Clouds. *ApJ*, 709:308–320, January 2010. doi: 10.1088/0004-637X/709/1/308.

M. Milgrom. A modification of the Newtonian dynamics as a possible alternative to the hidden mass hypothesis. *ApJ*, 270:365–370, July 1983. doi: 10.1086/161130.

M. Milgrom. The structure of Lyman-Alpha systems. *A&A*, 202:L9–L12, August 1988.

B. Moore, S. Ghigna, F. Governato, G. Lake, T. Quinn, J. Stadel, and P. Tozzi. Dark Matter Substructure within Galactic Halos. *ApJL*, 524:L19–L22, October 1999. doi: 10.1086/312287.

J. Moustakas and R. C. Kennicutt, Jr. An Integrated Spectrophotometric Survey of Nearby Star-forming Galaxies. *ApJS*, 164:81–98, May 2006. doi: 10.1086/500971.

C. A. Narayan and C. J. Jog. Origin of radially increasing stellar scaleheight in a galactic disk. *A&A*, 390:L35–L38, July 2002a. doi: 10.1051/0004-6361:20020961.

C. A. Narayan and C. J. Jog. Vertical scaleheights in a gravitationally coupled, three-component Galactic disk. *A&A*, 394:89–96, October 2002b. doi: 10.1051/0004-6361:20021128.

C. A. Narayan, K. Saha, and C. J. Jog. Constraints on the halo density profile using HI flaring in the outer Galaxy. *A&A*, 440:523–530, September 2005. doi: 10.1051/0004-6361:20041055.

J. F. Navarro, C. S. Frenk, and S. D. M. White. A Universal Density Profile from Hierarchical Clustering. *ApJ*, 490:493–508, December 1997.

BIBLIOGRAPHY

P. Noterdaeme, P. Petitjean, C. Ledoux, and R. Srianand. Evolution of the cosmological mass density of neutral gas from Sloan Digital Sky Survey II - Data Release 7. *A&A*, 505:1087–1098, October 2009. doi: 10.1051/0004-6361/200912768.

P. Noterdaeme, P. Laursen, P. Petitjean, S. D. Vergani, M. J. Maureira, C. Ledoux, J. P. U. Fynbo, S. López, and R. Srianand. Discovery of a compact gas-rich damped Lyman-α galaxy at z = 2.2: evidence of a starburst-driven outflow. *A&A*, 540:A63, April 2012a. doi: 10.1051/0004-6361/201118691.

P. Noterdaeme, P. Petitjean, W. C. Carithers, I. Pâris, A. Font-Ribera, S. Bailey, E. Aubourg, D. Bizyaev, G. Ebelke, H. Finley, J. Ge, E. Malanushenko, V. Malanushenko, J. Miralda-Escudé, A. D. Myers, D. Oravetz, K. Pan, M. M. Pieri, N. P. Ross, D. P. Schneider, A. Simmons, and D. G. York. Column density distribution and cosmological mass density of neutral gas: Sloan Digital Sky Survey-III Data Release 9. *A&A*, 547:L1, November 2012b. doi: 10.1051/0004-6361/201220259.

R. P. Olling. On the Usage of Flaring Gas Layers to Determine the Shape of Dark Matter Halos. *AJ*, 110:591, August 1995. doi: 10.1086/117545.

J. Ott, A. M. Stilp, S. R. Warren, E. D. Skillman, J. J. Dalcanton, F. Walter, W. J. G. de Blok, B. Koribalski, and A. A. West. VLA-ANGST: A High-resolution H I Survey of Nearby Dwarf Galaxies. *AJ*, 144:123, October 2012. doi: 10.1088/0004-6256/144/4/123.

N. N. Patra, J. N. Chengalur, and A. Begum. The H I column density distribution function in faint dwarf galaxies. *MNRAS*, 429:1596–1601, February 2013. doi: 10.1093/mnras/sts440.

C. Péroux, M. Dessauges-Zavadsky, S. D'Odorico, T. Sun Kim, and R. G. McMahon. A homogeneous sample of sub-damped Lyman α systems - III. Total gas mass $\Omega_{HI+HeII}$ at z $> 2^*$. *MNRAS*, 363:479–495, October 2005. doi: 10.1111/j.1365-2966.2005.09432.x.

C. Péroux, N. Bouché, V. P. Kulkarni, D. G. York, and G. Vladilo. A SINFONI integral field spectroscopy survey for galaxy counterparts to damped Lyman α systems - II. Dynamical properties of the galaxies towards Q0302 - 223 and Q1009 - 0026. *MNRAS*, 410:2251–2256, February 2011. doi: 10.1111/j.1365-2966.2010.17597.x.

A. Pontzen, F. Governato, M. Pettini, C. M. Booth, G. Stinson, J. Wadsley, A. Brooks, T. Quinn, and M. Haehnelt. Damped Lyman α systems in galaxy formation simulations. *MNRAS*, 390:1349–1371, November 2008. doi: 10.1111/j.1365-2966.2008.13782.x.

J. X. Prochaska and A. M. Wolfe. On the Kinematics of the Damped Lyman-α Protogalaxies. *ApJ*, 487:73–95, September 1997.

J. X. Prochaska and A. M. Wolfe. Protogalactic Disk Models of Damped Lyα Kinematics. *ApJ*, 507:113–130, November 1998. doi: 10.1086/306325.

J. X. Prochaska and A. M. Wolfe. On the (Non)Evolution of H I Gas in Galaxies Over Cosmic Time. *ApJ*, 696:1543–1547, May 2009. doi: 10.1088/0004-637X/696/2/1543.

J. X. Prochaska, S. Herbert-Fort, and A. M. Wolfe. The SDSS Damped Lyα Survey: Data Release 3. *ApJ*, 635:123–142, December 2005. doi: 10.1086/497287.

J. X. Prochaska, H.-W. Chen, M. Dessauges-Zavadsky, and J. S. Bloom. Probing the Interstellar Medium near Star-forming Regions with Gamma-Ray Burst Afterglow Spectroscopy: Gas, Metals, and Dust. *ApJ*, 666:267–280, September 2007. doi: 10.1086/520042.

W. J. Quirk. On the Gas Content of Galaxies. *ApJL*, 176:L9, August 1972. doi: 10.1086/181009.

V. Radhakrishnan and W. M. Goss. The Parkes Survey of 21-CENTIMETER Absorption in Discrete-Source Spectra. V. Note on the Statistics of Absorbing H i Concentrations in the Galactic Disk. *ApJS*, 24:161, January 1972. doi: 10.1086/190251.

A. Raiter, D. Schaerer, and R. A. E. Fosbury. Predicted UV properties of very metal-poor starburst galaxies. *A&A*, 523:A64, November 2010. doi: 10.1051/0004-6361/201015236.

S. Rao and F. Briggs. Neutral Hydrogen in Galaxies at the Present Epoch. *ApJ*, 419:515, December 1993. doi: 10.1086/173504.

S. M. Rao, D. B. Nestor, D. A. Turnshek, W. M. Lane, E. M. Monier, and J. Bergeron. Low-Redshift Damped Lyα Galaxies toward the Quasars B2 0827+243, PKS

0952+179, PKS 1127-145, and PKS 1629+120. *ApJ*, 595:94–108, September 2003. doi: 10.1086/377331.

K. Rohlfs. On the Structure of Interstellar Matter. I. Kinematics of the Interstellar Gas and the Brightness Temperature of the 21-cm Line Emission. *A&A*, 12:43, April 1971.

N. Roy, N. Kanekar, R. Braun, and J. N. Chengalur. The temperature of the diffuse H I in the Milky Way - I. High resolution H I-21 cm absorption studies. *MNRAS*, 436: 2352–2365, December 2013a. doi: 10.1093/mnras/stt1743.

N. Roy, N. Kanekar, and J. N. Chengalur. The temperature of the diffuse H I in the Milky Way - II. Gaussian decomposition of the H I-21 cm absorption spectra. *MNRAS*, 436:2366–2385, December 2013b. doi: 10.1093/mnras/stt1746.

N. Roy, N. Kanekar, and J. N. Chengalur. The temperature of the diffuse H I in the Milky Way - II. Gaussian decomposition of the H I-21 cm absorption spectra. *MNRAS*, 436:2366–2385, December 2013c. doi: 10.1093/mnras/stt1746.

S. Roychowdhury, J. N. Chengalur, A. Begum, and I. D. Karachentsev. Star formation in extremely faint dwarf galaxies. *MNRAS*, 397:1435–1453, August 2009. doi: 10.1111/j.1365-2966.2009.14931.x.

S. Roychowdhury, J. N. Chengalur, A. Begum, and I. D. Karachentsev. Thick gas discs in faint dwarf galaxies. *MNRAS*, 404:L60–L63, May 2010. doi: 10.1111/j.1745-3933.2010.00835.x.

S. Roychowdhury, J. N. Chengalur, S. S. Kaisin, A. Begum, and I. D. Karachentsev. Small Bites: star formation recipes in extreme dwarfs. *MNRAS*, 414:L55–L59, June 2011. doi: 10.1111/j.1745-3933.2011.01055.x.

S. Roychowdhury, J. N. Chengalur, I. D. Karachentsev, and E. I. Kaisina. The intrinsic shapes of dwarf irregular galaxies. *MNRAS*, 436:L104–L108, November 2013. doi: 10.1093/mnrasl/slt123.

S. Roychowdhury, J. N. Chengalur, S. S. Kaisin, and I. D. Karachentsev. The relation between atomic gas and star formation rate densities in faint dwarf irregular galaxies. *MNRAS*, 445:1392–1402, December 2014. doi: 10.1093/mnras/stu1814.

K. Saha and W. Maciejewski. Spontaneous formation of double bars in dark-matter-dominated galaxies. *MNRAS*, 433:L44–L48, June 2013. doi: 10.1093/mnrasl/slt055.

R. Sancisi and R. J. Allen. Neutral hydrogen observations of the edge-on disk galaxy NGC 891. *A&A*, 74:73–84, April 1979.

B. D. Savage, R. C. Bohlin, J. F. Drake, and W. Budich. A survey of interstellar molecular hydrogen. I. *ApJ*, 216:291–307, August 1977. doi: 10.1086/155471.

J. Schaye. A Physical Upper Limit on the H I Column Density of Gas Clouds. *ApJL*, 562:L95–L98, November 2001. doi: 10.1086/338106.

E. F. Schlafly and D. P. Finkbeiner. Measuring Reddening with Sloan Digital Sky Survey Stellar Spectra and Recalibrating SFD. *ApJ*, 737:103, August 2011. doi: 10.1088/0004-637X/737/2/103.

M. Schmidt. Spiral structure in the inner parts of the Galactic System derived from the hydrogen emission at 21-cm wavelength. *BAN*, 13:247, May 1957.

A. Schruba, A. K. Leroy, F. Walter, F. Bigiel, E. Brinks, W. J. G. de Blok, C. Kramer, E. Rosolowsky, K. Sandstrom, K. Schuster, A. Usero, A. Weiss, and H. Wiesemeyer. Low CO Luminosities in Dwarf Galaxies. *AJ*, 143:138, June 2012. doi: 10.1088/0004-6256/143/6/138.

K. F. Schuster, C. Kramer, M. Hitschfeld, S. Garcia-Burillo, and B. Mookerjea. A complete ^{12}CO 2-1 map of M 51 with HERA. I. Radial averages of CO, H I, and radio continuum. *A&A*, 461:143–151, January 2007. doi: 10.1051/0004-6361:20065579.

J. A. Sellwood and S. A. Balbus. Differential Rotation and Turbulence in Extended H I Disks. *ApJ*, 511:660–665, February 1999. doi: 10.1086/306728.

W. L. H. Shuter and G. L. Verschuur. A high resolution investigation of 21 cm absorption. *MNRAS*, 127:387, 1964.

V. Springel, J. Wang, M. Vogelsberger, A. Ludlow, A. Jenkins, A. Helmi, J. F. Navarro, C. S. Frenk, and S. D. M. White. The Aquarius Project: the subhaloes of galactic haloes. *MNRAS*, 391:1685–1711, December 2008. doi: 10.1111/j.1365-2966.2008.14066.x.

R. Srianand, P. Petitjean, C. Ledoux, G. Ferland, and G. Shaw. The VLT-UVES survey for molecular hydrogen in high-redshift damped Lyman α systems: physical conditions in the neutral gas. *MNRAS*, 362:549–568, September 2005. doi: 10.1111/j.1365-2966.2005.09324.x.

J. Stadel, D. Potter, B. Moore, J. Diemand, P. Madau, M. Zemp, M. Kuhlen, and V. Quilis. Quantifying the heart of darkness with GHALO - a multibillion particle simulation of a galactic halo. *MNRAS*, 398:L21–L25, September 2009. doi: 10.1111/j.1745-3933.2009.00699.x.

C. C. Steidel, M. Pettini, and D. Hamilton. Lyman Imaging of High-Redshift Galaxies.III.New Observations of Four QSO Fields. *AJ*, 110:2519, December 1995. doi: 10.1086/117709.

A. M. Stilp, J. J. Dalcanton, E. Skillman, S. R. Warren, J. Ott, and B. Koribalski. Drivers of H I Turbulence in Dwarf Galaxies. *ApJ*, 773:88, August 2013. doi: 10.1088/0004-637X/773/2/88.

G. Swarup, S. Ananthakrishnan, V. K. Kapahi, A. P. Rao, C. R. Subrahmanya, and V. K. Kulkarni. The Giant Metre-Wave Radio Telescope. *Current Science, Vol. 60, NO.2/JAN25, P. 95, 1991*, 60:95, January 1991.

D. Tamburro, H.-W. Rix, A. K. Leroy, M.-M. Mac Low, F. Walter, R. C. Kennicutt, E. Brinks, and W. J. G. de Blok. What is Driving the H I Velocity Dispersion? *AJ*, 137:4424–4435, May 2009. doi: 10.1088/0004-6256/137/5/4424.

G. A. Tammann. Dwarf Galaxies in the Past. In G. Meylan and P. Prugniel, editors, *European Southern Observatory Conference and Workshop Proceedings*, volume 49 of *European Southern Observatory Conference and Workshop Proceedings*, page 3, January 1994.

E. J. Tollerud, J. S. Bullock, L. E. Strigari, and B. Willman. Hundreds of Milky Way Satellites? Luminosity Bias in the Satellite Luminosity Function. *ApJ*, 688:277–289, November 2008. doi: 10.1086/592102.

D. A. Turnshek, S. Rao, D. Nestor, W. Lane, E. Monier, J. Bergeron, and A. Smette. The z=0.0912 and z=0.2212 Damped Lyα Galaxies along the Sight Line toward the Quasar OI 363. *ApJ*, 553:288–298, May 2001. doi: 10.1086/320660.

M. A. W. Verheijen and R. Sancisi. The Ursa Major cluster of galaxies. IV. HI synthesis observations. *A&A*, 370:765–867, May 2001. doi: 10.1051/0004-6361:20010090.

M. A. W. Verheijen, T. A. Oosterloo, W. A. van Cappellen, L. Bakker, M. V. Ivashina, and J. M. van der Hulst. Apertif, a focal plane array for the WSRT. In R. Minchin and E. Momjian, editors, *The Evolution of Galaxies Through the Neutral Hydrogen Window*, volume 1035 of *American Institute of Physics Conference Series*, pages 265–271, August 2008. doi: 10.1063/1.2973599.

K. Wada, G. Meurer, and C. A. Norman. Gravity-driven Turbulence in Galactic Disks. *ApJ*, 577:197–205, September 2002. doi: 10.1086/342151.

F. Walter, E. Brinks, W. J. G. de Blok, F. Bigiel, R. C. Kennicutt, Jr., M. D. Thornley, and A. Leroy. THINGS: The H I Nearby Galaxy Survey. *AJ*, 136:2563, December 2008. doi: 10.1088/0004-6256/136/6/2563.

B. E. Warren, H. Jerjen, and B. S. Koribalski. The Minimum Amount of Stars a Galaxy Will Form. *AJ*, 134:1849, November 2007. doi: 10.1086/521925.

S. R. Warren, E. D. Skillman, A. M. Stilp, J. J. Dalcanton, J. Ott, F. Walter, E. A. Petersen, B. Koribalski, and A. A. West. Tracing Cold H I Gas in nearby, Low-mass Galaxies. *ApJ*, 757:84, September 2012. doi: 10.1088/0004-637X/757/1/84.

D. R. Weisz, B. D. Johnson, L. C. Johnson, E. D. Skillman, J. C. Lee, R. C. Kennicutt, D. Calzetti, L. van Zee, M. S. Bothwell, J. J. Dalcanton, D. A. Dale, and B. F. Williams. Modeling the Effects of Star Formation Histories on Hα and Ultraviolet Fluxes in nearby Dwarf Galaxies. *ApJ*, 744:44, January 2012. doi: 10.1088/0004-637X/744/1/44.

D. E. Welty, R. Xue, and T. Wong. Interstellar H I and H_2 in the Magellanic Clouds: An Expanded Sample Based on Ultraviolet Absorption-line Data. *ApJ*, 745:173, February 2012. doi: 10.1088/0004-637X/745/2/173.

A. M. Wolfe and M. M. Davis. Detection of 21-cm absorption at Z of approximately 1.8 in the quasi-stellar object 1331+170. *AJ*, 84:699–706, June 1979. doi: 10.1086/112470.

BIBLIOGRAPHY

A. M. Wolfe, D. A. Turnshek, H. E. Smith, and R. D. Cohen. Damped Lyman-alpha absorption by disk galaxies with large redshifts. I - The Lick survey. *ApJS*, 61: 249–304, June 1986. doi: 10.1086/191114.

A. M. Wolfe, J. X. Prochaska, and E. Gawiser. C II* Absorption in Damped Lyα Systems. I. Star Formation Rates in a Two-Phase Medium. *ApJ*, 593:215–234, August 2003. doi: 10.1086/376520.

A. M. Wolfe, E. Gawiser, and J. X. Prochaska. Damped Ly α Systems. *ARA&A*, 43: 861–918, September 2005. doi: 10.1146/annurev.astro.42.053102.133950.

M. G. Wolfire, D. Hollenbach, C. F. McKee, A. G. G. M. Tielens, and E. L. O. Bakes. The neutral atomic phases of the interstellar medium. *ApJ*, 443:152–168, April 1995a. doi: 10.1086/175510.

M. G. Wolfire, C. F. McKee, D. Hollenbach, and A. G. G. M. Tielens. The Multiphase Structure of the Galactic Halo: High-Velocity Clouds in a Hot Corona. *ApJ*, 453: 673, November 1995b. doi: 10.1086/176429.

M. G. Wolfire, C. F. McKee, D. Hollenbach, and A. G. G. M. Tielens. Neutral Atomic Phases of the Interstellar Medium in the Galaxy. *ApJ*, 587:278–311, April 2003. doi: 10.1086/368016.

L. M. Young and K. Y. Lo. The Neutral Interstellar Medium in Nearby Dwarf Galaxies. I. Leo A. *ApJ*, 462:203, May 1996. doi: 10.1086/177141.

L. M. Young and K. Y. Lo. The Neutral Interstellar Medium in Nearby Dwarf Galaxies. III. Sagittarius DIG, LGS 3, and Phoenix. *ApJ*, 490:710–728, December 1997.

L. M. Young, L. van Zee, K. Y. Lo, R. C. Dohm-Palmer, and M. E. Beierle. Star Formation and the Interstellar Medium in Four Dwarf Irregular Galaxies. *ApJ*, 592: 111–128, July 2003. doi: 10.1086/375581.

T. Zafar, C. Péroux, A. Popping, B. Milliard, J.-M. Deharveng, and S. Frank. The ESO UVES advanced data products quasar sample. II. Cosmological evolution of the neutral gas mass density. *A&A*, 556:A141, August 2013. doi: 10.1051/0004-6361/201321154.

M. A. Zwaan, L. Staveley-Smith, B. S. Koribalski, P. A. Henning, V. A. Kilborn, S. D. Ryder, D. G. Barnes, R. Bhathal, P. J. Boyce, W. J. G. de Blok, M. J. Disney, M. J. Drinkwater, R. D. Ekers, K. C. Freeman, B. K. Gibson, A. J. Green, R. F. Haynes, H. Jerjen, S. Juraszek, M. J. Kesteven, P. M. Knezek, R. C. Kraan-Korteweg, S. Mader, M. Marquarding, M. Meyer, R. F. Minchin, J. R. Mould, J. O'Brien, T. Oosterloo, R. M. Price, M. E. Putman, E. Ryan-Weber, E. M. Sadler, A. Schröder, I. M. Stewart, F. Stootman, B. Warren, M. Waugh, R. L. Webster, and A. E. Wright. The 1000 Brightest HIPASS Galaxies: The H I Mass Function and Ω_{HI}. *AJ*, 125: 2842–2858, June 2003. doi: 10.1086/374944.

M. A. Zwaan, J. M. van der Hulst, F. H. Briggs, M. A. W. Verheijen, and E. V. Ryan-Weber. Reconciling the local galaxy population with damped Lyman α cross-sections and metal abundances. *MNRAS*, 364:1467–1487, December 2005. doi: 10.1111/j.1365-2966.2005.09698.x.